STM/STS and BEES Study of Nanocrystals

A Thesis
Presented to
The Academic Faculty

by

Jianfei Shao

In Partial Fulfillment
of the Requirements for the Degree
Doctor of Philosophy

School of Physics
Georgia Institute of Technology
May 2006

STM/STS and BEES Study of Nanocrystals

Approved by:

Dr. Phillip N. First, Advisor
School of Physics
Georgia Institute of Technology

Dr. Alexei Marchenkov
School of Physics
Georgia Institute of Technology

Dr. Edward H. Conrad
School of Physics
Georgia Institute of Technology

Dr. Robert L. Whetten
School of Chemistry & Biochemistry
Georgia Institute of Technology

Dr. Walter A. De Heer
School of Physics
Georgia Institute of Technology

Date Approved: March 23, 2006

To my mother,

Yuexian Mei

(1929 - 2004)

ACKNOWLEDGEMENTS

I thank my advisor, Dr. First, for his years support and guidance. His amazing knowledge of materials and equipments is always an encouragement to me. I appreciate his valuable help when I was stuck in China due to Visa problem. In the final month of my stay at Georgia Tech, Dr. First read my thesis page by page and pointed out numerous mistakes I made. This thesis would not be readable without his careful reading. I also appreciate his patience and kindness to my poor English. During my Ph. D program. I got a lot of help and guidance from other professors of my thesis committee, Dr. Conrad, Dr. De Heer, Dr. Marchenkov, and Dr. Whetten. I thank them for allowing me to use their equipments, from Epoxy to variacs.

When I started to work on this project, Dr. Bigioni and Dr. Ogbazghi gave me great help and training in experimental physics. They taught me how to move forward in the lab fast and steady. I thank my main collaborators, Sameh Dardona, Ryan Price, Alex Schill, and Qusai Darugar. This project is impossible without them. Other students in Dr. First's group, Greg Rutter, Joanna Hass, Tianbo Li, Nikhil Sharma gave me constant help. I appreciate the nice atmosphere they created in the lab. Other members in Dr. Conrad's group, Dr. Davidovic's, Dr. De Heer's group, and Dr. Marchenkov's group, are always kind and helpful to me. I thank them all.

During my stay at Georgia Tech, I got valuable guidance from many professors. Among them I especially thank Dr. Zangwill for his help to my academic things. Dr. Gaylord and Dr. Glytsis led me to the envelope function method. Their well-organized lecture notes and research documents influence my habit of doing things. I appreciate Dr. Gaylord's RA support when I lost financial support from School of Physics. I thank Dr. Davidovic and Dr. Trebino for the guidance and help I received while staying in their group.

My family always give me support and encouragement whenever I need them. Their love accompanied me through all the difficult times.

TABLE OF CONTENTS

LIST OF TABLES

LIST OF FIGURES

SUMMARY

This work investigates the electronic properties of very small gold and semiconductor particles using Scanning Tunneling Microscopy/Spectroscopy (STM/STS) and Ballistic Electron Emission Spectroscopy (BEES). Complementary theoretical works were also performed. The first theoretical work was to calculate the quantized states in the CdS/HgS/CdS quantum-well-quantum-dot nanocrystals. Since HgS is a narrow band gap semiconductor and CdS is a wide band gap semiconductor, we expect the quantized states to be a strong mixture of states from both the conduction bands and the valence bands. In order to include the coupling between the conduction bands and the valence bands, an eight-band envelope function method was applied to this system. This method treats exactly the coupling between the conduction bands, the light-hole bands, the heavy-hole bands, and the spin-orbit split bands. The contributions of all other bands were taken into account using second order perturbation theory.

Gold nanocrystals with diameters of 1.5 nm have discrete energy levels with energy spacings of about 0.2 eV. These values are comparable to the single electron charging energy, which was about 0.5 eV in our experimental configuration. Since bulk gold doesn't have an energy gap, we expect the electron levels both below and above the Fermi level should be involved in the tunneling. Measured spectroscopy data have rich features. In order to understand and relate these features to the electronic properties of the nanocrystals, we developed a tunneling model. This model includes the effect of excited states which have electron-hole pairs. The relaxation between discrete electron energy levels can also be included in this model. We also considered how the nanocrystals affect the BEES current.

In this work an ultra-high vacuum and low-temperature STM was re-designed and rebuilt. The BEEM/BEES capabilities were incorporated into the STM. We used this STM to image gold nanocrystals and semiconductor nanocrystals. STS and BEES spectra of gold nanocrystals were collected and compared with calculations.

CHAPTER I

INTRODUCTION

1.1 Physics of Nanocrystals

In the past two decades, artificial structures with reduced size and dimensions have been fabricated successfully due to advance of material science technologies. Thin film growth can be controlled with single layer precision. Electron beam lithography can make patterns with widths of nanometers (1 nm=10^{-9} m). Quantum wells are typical "2D" structures. Different materials are grown layer by layer. Material with small band gap is sandwiched between materials with high band gap. Band edge offsets at the interfaces will form a "quantum well" for electrons and holes in the middle layer. Carriers can move freely in the plane along the layer, but their movement in the perpendicular direction is confined by the energy barriers. Since carriers can move freely in two dimensions but are limited in the third dimension, this kind of structure is called 2D structure. Quantum wires are "1D" structures. Carriers can only move freely in one dimension along the axis of the wire. Carbon nanotubes may be the most famous example of 1D structures. The "0D" structures are those in which carrier movement is confined in all directions. There are many terms related to 0D structures: cluster, quantum dot, nano particle, and nanocrystal.

"Cluster" usually refers to metal or semiconductor particles comprised of several to tens of atoms. "Quantum dot" is a name used mainly in Electrical Engineering and Material Science. When depositing material onto a flat substrate of a different material, if the amount of deposited material is equivalent to only several layers, then the deposited material might form islands instead of a uniform layer. The driving force behind this phenomena is energy minimize principle. Forming islands can reduce the total energy by reducing the energy due to surface tension and strain from lattice mismatch. Advanced microelectronic lithography and etching can also make quantum dots with the sizes of several tens of nanometers. Quantum dots are usually made from semiconductor materials. "Nano particle" refers to

very small particles made by novel deposition methods. "Nanocrystal" is a term used for small particles made by chemical synthesis. Most of them are synthesized using a colloidal technique. They have ordered lattice structures and even facets on the surface. The wok in this thesis focuses on chemically synthesized nanocrystals.

When dimension and size change, physical properties also change. The quantum confinement (QC) effect is one of the most important changes seen in low-dimensional structures. Carriers, electron or hole, are constantly scattered in solid materials. Impurity atoms, lattice defects, surfaces or interfaces will introduce defects in the ideal lattice structure. These defect potentials will scatter carriers from one Bloch state to another. Even in perfect lattices, the thermal deviation of ion from equilibrium positions introduces scattering of the carriers. Scattering originating from this perturbation is called electron-phonon (e-p) scattering. Scattering among carriers can also occur since the Coulomb force is not perfectly screened. This is electron-electron (e-e) scattering. The scattering is inelastic or elastic depending on whether carriers lose energy or not. Scattering can also change the momentum and phase. The average distance carrier moves before it loses phase is called the coherence length. If the sizes of the system is comparable to the coherence length of carriers, the wave function of the carrier is affected by the surfaces or interfaces. The boundaries will pose restrictions on the allowed energy levels for carriers. Effects introduced by this restriction are called quantum confinement effects.

Nanocrystals are good candidates to show the effects of quantum confinement in low dimensional structures. Typical nanocrystals are composed of several tens to one thousand atoms. Compared with bulk materials, nanocrystals don't have long range translation symmetry. Movement of electrons and holes are well confined in three dimensions. Wave functions of electrons or holes have to be terminated at the surface. In order to meet this requirement, the energy levels can't be arbitrary. Only some specific energies will meet the boundary conditions. So the energy levels inside nanocrystals are discrete. The spacing between neighboring levels is inversely related to the size.

Another striking property due to QC is the band gap change in semiconductor nanocrystals. The change in band gap is manifested by the continuous shifting of absorption edge

of semiconductor nanocrystals when the size changes. For direct band gap semiconductors, the absorption edges will shift to the blue when the size is reduced. In optical absorption measurement, valence electrons will be excited to conduction band states by absorbing photons. The energy of photons have to be larger than the band gap in order to be absorbed. Therefore the edge of the absorption curve is very close to the band gap energy. In Figure 1 [46], the absorption edge of CdSe nanocrystals changes from 420 nm for 1.2 nm diameter nanocrystals to 670 nm for 11.5 nm ones [46]. This spectrum extends across the whole visible spectrum (from 475 nm to 650 nm). The band gap changes are the direct consequence of QC. In order to meet the boundary condition, wave functions have to change more drastically in nanocrystals than in bulk material. From quantum mechanics, the total energy of one electron is the sum of its kinetic and potential energy. The kinetic energy is proportional to the second derivative of the wave function. Therefore in nanocrystals, electrons are expected to have more kinetic energy. For holes, the energy levels are downshifted. So band gaps of semiconductor nanocrystals become larger than the bulk band gap of the same material.

The energy of electron states for not very small semiconductor nanocrystals can be calculated by envelope function method (EFM) or effective mass approximation (EMA). This method assumes the wave function of an electron is the product of a slowly varying function $F(r)$, the envelope function, and a rapid varying function, $u(r)$. Usually $u(r)$ is chosen as the bulk Bloch wave function at band minimum or maximum. For III-V semiconductors, $u(r)$ is the Bloch wave function at zone center with $k = 0$. In this case, $u(r)$ is a periodic function of the bulk lattice. The $F(r)$ is described by effective mass of electrons in conduction band m_e or hole in valence band m_h. m_e and m_h include effects due to band structure. For a wide band gap semiconductor nanocrystal, the energy levels in the conduction band can be calculated as follows:

$$-\frac{\hbar^2}{2m_e}\nabla^2 F_l(r) + U(r)F_l(r) = E_l F_l(r) \tag{1}$$

$U(r)$ is the potential barrier at surfaces or interfaces. For "particle-in-box" problem, U(r)

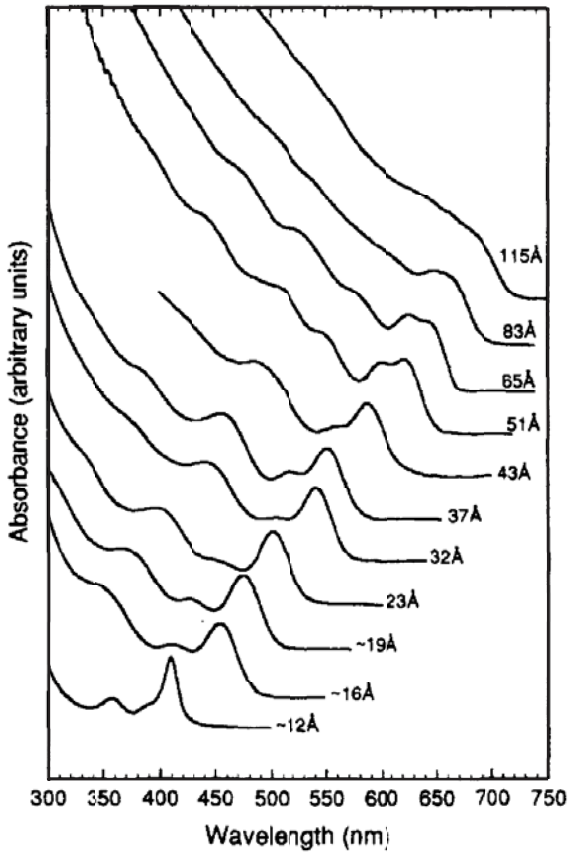

Figure 1: Optical absorption spectrum of CdSe nanocrystals with size from 12 Å to 115 Å [46].

is just the energy barrier measured from the bottom of the conduction band to the vacuum level. Since effective masses for semiconductors are usually small, the kinetic energy change due to the size confinement is quite significant. This is why discrete energy levels due to quantum confinement are observable for semiconductor nanocrystals even at room temperature.

The case for metal nanocrystals is different. The free electron model is a reasonable starting point for typical metal nanocrystals. Applying this model to metal nanocrystals, we will have similar equation as Eq. (1). But the mass is the mass of the bare electron. It is much large than typical electron or hole effective mass of semiconductors. Because of this, the QC introduced energy shift is relatively small in metal nanocrystals. So in order to observe discrete energy levels in metal nanocrystals, the temperature has to be very low or the size of metal nanocrystal has to be very small, or both.

Reducing the size also changes the electron-electron (e-e) and electron-phonon (e-p) interactions. The Coulomb interaction of two electrons is modified by the existence of other electrons. Other electrons will move relative to fixed positive ions in order to minimize the interaction between two bare electrons. In nanocrystals, the surface to volume ratio is large. This large ratio reduces the average electron density for the screening of the bare electron interaction. Therefore the e-e interaction is expected to increase while size decreases. The electron-phonon interaction is basically Coulomb interaction between a negative charge (electron) and a positive charge (ion). So the decrease of screening should increase the e-p interaction. We know the relaxation processes inside nanocrystals depend on the strength of interactions. The relaxation from non-equilibrium to equilibrium is expected to be faster in nanocrystal than in bulk material.

Another complication related to e-p interaction arises in small nanocrystals. For very small nanocrystals, the energy level spacing is not small. The energy spacing can be several times bigger than the energy of longitudinal-optical phonon (LO). If one electron is excited to a high level initially, the non-radiative relaxation of this electron back to lower energy level needs to transfer some energy to phonons. In case when electron energy level spacing

is several times bigger than energy of a single phonon, the relaxation process is a multiple-phonon process. This multiple-phonon process would be very slow. This phenomena is called the "phonon bottleneck".

There are many methods to calculate the electronic structures of nanocrystals. For semiconductor nanocrystals, the envelope function method (or the effective mass method) is simple and can provide a good qualitative picture. This method is limited to large nanocrystals. Envelope function method originally was used to describe electron response to slow varying external fields [43]. It describes wave function variations on a scale much larger than the lattice constants. If the size of nanocrystals is close to lattice constants of bulk materials, envelope function method is problematic. For wide band gap materials, the coupling between conduction band and valence bands is weak. So the states in conduction band can be described with a single effective mass. But for small band gap materials, the coupling between conduction band and valence bands is large. The states have to be described by coupled equations of envelope functions. This makes the envelope function method complicated. Tight-binding is another widely used method to calculate electronic structures of semiconductor nanocrystals. The simplicity of tight-binding is somehow lost in nanocrystals because of the absence of translation symmetry. But for nanocrystals composed of several hundred atoms, the application of tight-binding method is straightforward and practical for numerical computation. Tight-binding method is based on atomic orbitals. It doesn't use the translational invariance of bulk band structure. So it is proper for very small nanocrystals where effective envelope function method is not proper. Another advantage of tight-binding method is that it can treat the surface more accurately.

For metal nanocrystals with the size range of 1$\sim$10 nm, the combination of spherical jellium model and density functional theory (DFT) [38] with local-density approximation (LDA) is widely used to calculate the electronic structure. The nanocrystals are imagined as spheres without any lattice structure. The total charges of ions are assumed to be evenly distributed inside the spheres. Wave functions of valence electrons and electron density are calculated using the Kohn-Sham scheme [41] in a recursive way. This approach can produce good quantitative results.

A variety of experimental techniques have been applied to investigate properties of nanocrystals. Transmission electron microscopy (TEM) is used to measure sizes of nanocrystals and lattice structures. Atomic force microscopy (AFM) is used to measure size distribution of nanocrystals. Electrochemical methods can be used to measure charging processes. Among all the techniques, Scanning tunneling microscopy (STM) with its spectroscopy (STS) and optical spectroscopy are the most powerful tools to probe the electronic properties and dynamic processes inside nanocrystals.

Optical processes are directly related to transitions between electron states. The energy of emitted or absorbed photon is equal to the energy difference between the initial and final electron states. The size dependence of band gap and discrete energy levels in semiconductor nanocrystals are first manifested by absorption spectrum and photoluminescence spectrum. Optical spectroscopy is also a powerful tool for studying dynamic processes. With ultrafast laser pulses, optical spectroscopy can have time resolution of femtoseconds. This kind time resolved experiments are usually of pump-probe type. An ultrafast laser pulse with proper wavelength is used to excite electrons to a non-equilibrium distribution. A second ultrafast laser pulse comes to the sample with different wavelength and controlled time delay. The absorption spectrum is related to the non-equilibrium distribution of electrons. The change of light transmission gives a snapshot of electron states at that particular time. Based on this information, rates of e-e interaction and e-p interaction which are responsible for the change of states can be estimated. This pump-probe method has been used to investigate relaxation rates inside nanocrystals. One of the result is that, the relaxation rates related to e-e and e-p interaction increase when size decreases. This result is consistent with theories mentioned before. The e-e and e-p interaction depend on the effective screening of the Coulomb interactions between the charged particles, electron-electron for e-e or electron-ion for e-p. Reduced "effective" electron density increases the interactions. Therefore relaxation rates increase when size decreases.

Scanning tunneling microscopy with its spectroscopy is another powerful technique to probe sates of electrons inside nanocrystals. The unique advantage of STM is the spacial resolution. STM can have atomic resolution. The high resolution of STM comes from its

capability of moving probe tip with sub-angstrom precision. When nanocrystals are on a flat surface, STM can "see" the surface height change due to nanocrystals. Individual nanocrystals can be investigated one by one without interfering with each other. Once a single nanocrystal is resolved, the tip can be set above the it. By changing the tip voltage and recording corresponding change of tunneling current, information about the electron states can be collected. Without averaging, STM/STS can get more accurate relation between size and electronic properties compared with optical spectroscopy. STM data is a good compliment to the optical spectroscopy data. Optical spectroscopy data is about the properties of neutral nanocrystals since optical excitation doesn't change the charge state of nanocrystals. At the other hand, tunneling spectroscopy involves adding electrons onto or extracting electrons off nanocrystals. Therefore the STM data is related to the charge state of nanocrystals.

In order to image nanocrystals, two conditions have to be met. The first is a relative flat surface to support nanocrystals. The STM tip usually has finite radius of several tens of nanometers. If the surface height has random fluctuation of the order of nanocrystal diameters with high space pitch, then the tip will have tunneling current at different points, some close to nanocrystals and some close to bumps on the surface. This is especially true to cases of small metal nanocrystals. The second condition is that nanocrystals have to be fixed on the surface rigidly. The tunneling current exponentially depends on the distance between the tip and the nanocrystals under it. For most of the experiments, the tunneling current is set at $10^{-11} \sim 10^{-10}$ Ampere. The corresponding distance is several angstroms. In order to inject electrons onto nanocrystals, finite voltage is applied between the tip and the surface. This voltage will produce a huge electric field between the tip and the substrate. When one electron is injected from the tip to the nanocrystal, the nanocrystal will not be charge neutral anymore. The charged nanocrystal will experience very large electrostatic force. The repulsion force between the tip and the nanocrystal will expel the nanocrystal away from the tip. For colloidal synthesized nanocrystals, one way to fix nanocrystals to the surface is using organic molecules with sulfur atom at both ends. For example, gold nanocrystals can be attached to gold substrate by xylenedithiol. Xylenedithiol has a sulfur

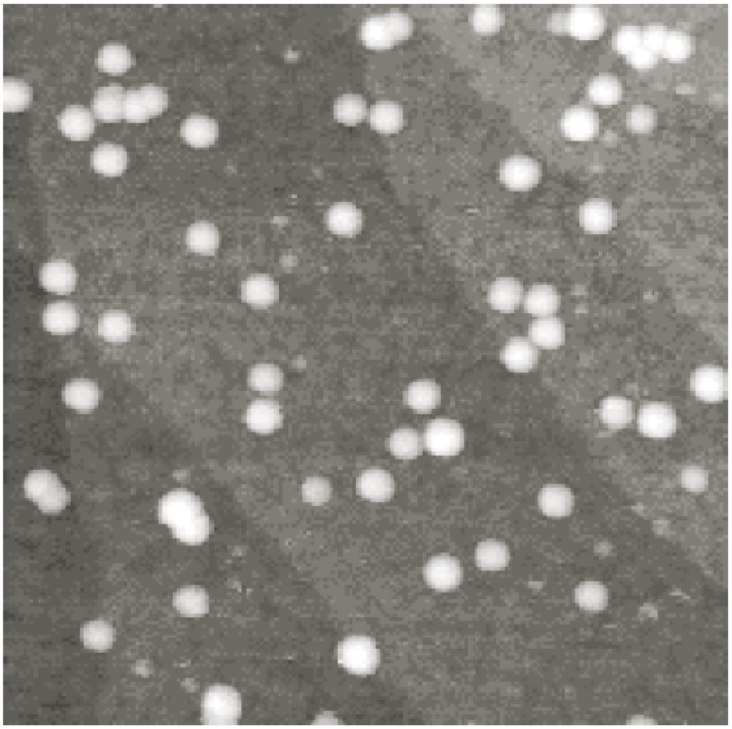

Figure 2: STM image of Au nanocrystals bonded to gold substrate by xylenedithoil molecules [20].

atom at each end. Sulfur atoms can form relatively strong bonds with gold. If one sulfur atom is bonded to a gold atom on the substrate and the other is bonded with a gold atom on the nanocrystal, the nanocrystal can be attached to the surface by xylenedithiol. Figure 2 shows the STM image of a sample prepared in such a way [20].

Semiconductor nanocrystals CdS, CdSe, ZnS, InAs, and PbSe have been imaged successfully using similar technique as mentioned above. Figure 3 is the measured dI/dV curves of InAs nanocrystals [44]. The STS curves clearly show voltage gaps at the middles of dI/dV curves. This gap is related to the energy band gap of nanocrystals. The widening of the gap with decreasing size supports the theory of quantum confinement. In Fig. 3(b), dI/dV peaks are assigned to different energy states. For InAs spherical nanocrystals, the lowest conduction band electron level is of s type (the envelope function has zero angular momentum). Due to spin degeneracy, this level is double degenerate. So the authors assigned the first two peaks to two s electron levels. The spacing between these two peaks was thought

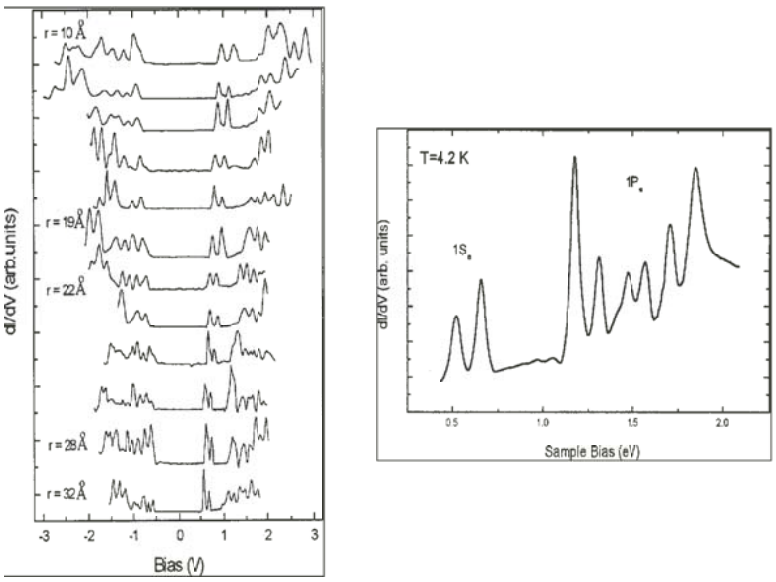

(a) (b)

Figure 3: (a) Size dependence of dI/dV versus V curves of InAs nanocrystals. (b) Interpretation of dI/dV peaks [44].

to be the Coulomb interaction energy between two electrons on the s level. The next six peaks were assigned to p type levels with degeneracy of six if including spin degeneracy.

The interpretation of dI/dV in metal nanocrystals is different from the semiconductor case. For same size nanocrystals, the energy spacing of discrete energy levels is much smaller for metal than for semiconductor. Discrete energy levels can only be resolved for very small metal nanocrystals at low temperature. For small metal particles, the capacitances of tip-nanocrystal junction and nanocrystal-substrate junction are very small. When there is one net charge on the nanocrystal, the electrostatic energy building up in two junctions is about $e^2/2C_{total}$ where C_{total} is the total capacitance of two junctions. This electrostatic energy called charging energy can be several hundred meV. Usually It is much larger than the energy spacing of quantized energy levels. In order to tunnel one electron on to the initially neutral nanocrystal, the tip has to be biased at voltage high enough to provide the necessary energy for the tunneling electron to overcome the final state electrostatic energy. This is the Coulomb Blockade (CB) phenomenon. dI/dV curves for metal nanocrystals will have similar gap at the middle as in Fig. (3). But this gap is related to Coulomb blockade. It

is not dominated by density of energy states of the nanocrystal. This gap also will increase while the size decreases. For peaks higher than the first one, they can't simply be assigned to discrete energy levels. In some nanocrystals, these peaks are related to multiple charging. Starting from voltages at these peaks, tip can add several net electrons or holes onto the nanocrystal.

1.2 Synthesis of Nanocrystals

There are two general categories of approaches to make semiconductor nano-size particles. One is called the "top-down" approach. This approach usually uses microelectronics techniques. An epitaxial thin layer is patterned by E-beam lithography and etched into quantum dots. Quantum dots made by this way are usually large (tens of nm). The "bottom-up" approach has two types. One type is the self-assembly method. An amount of material equivalent to a few layers is deposited on the substrate. The deposited material forms particles in order to minimize total energy. The other "bottom-up" method is wet chemical synthesis.

The nanocrystals investigated in this thesis were synthesized by wet chemical methods. Since the 1980s, II-VI semiconductor nanocrystals with different size are synthesized by reverse micelle method [56]. Water is added to hydrocarbon solvents with surfactant. The surfactant has a polar head at one end and a non-polar head at the other. The polar heads will be attracted to surface of small drops of water. Each small drop of water is called a micelle. The surfactant molecules attached to the water drop basically form a membrane. After precursors for nanocrystals are added into the solvent, anions (for example Se^{2-}) permeate the surfactant membrane more easily than cations (for example Cd^{2+}). So the water pool inside the membrane becomes a trap for anions. The association of anions and cations forms nanocrystals. The size of the nanocrystals is controlled by the number of cations and anions inside each micelle. Good control of the concentration of ions, size and number of micelles can achieve small semiconductor nanocrystals. The micelles will prevent the aggregation of nanocrystals since each nanocrystal is confined in its own micelle and the surfactant molecules prevent them from contacting with one another. If nanocrystals

come out of micelles, they will aggregate in order to minimize the surface energy. So capping reagents must be added to prevent aggregation after nanocrystals are extracted from micelles.

Another method to synthesize semiconductor nanocrystals is based on pyrolysis of organometallic reagents at high temperature [46]. The coordinate solvent with proper surfactant is heated up to several hundred Celsius. Solvents containing organometallic precursors are injected into the hot solvent. Precursors are decomposed into ions and organic products. The ions become supersaturated. They will form nuclei suddenly. The concentration will drop below the threshold concentration for nucleation after many nuclei form. After that, no new nuclei will form in the solvent. Nuclei formed just after injection of precursors will grow bigger slowly with time. The surfactant inside the solvent will cover surfaces of nanocrystals. The surfactant will prevent nanocrystals to aggregate. The attachment of surfactant to the surface of nanocrystals is not very strong. Ions inside solvent can penetrate the surfactant and are attached to nanocrystals. Surface atoms of the nanocrystals can also easily dissociate from nanocrystals. This freedom reduces the lattice defects of nanocrystals. The growth of nanocrystals can be stopped by reducing the temperature or stopping the feed of precursors. The advantages of this method are low size diversity and high quality crystalline structure. The separation of nucleation and growth is the key for high degree of monodispersity. All the nuclei are formed at the same time and then they grow at the same speed. The high temperature also anneals nanocrystals. This also reduces lattice defects . Figure 4 shows the basic process and setup of this method.

Gold nanocrystals are synthesized using a two-phase technique [22]. Aqueous solution of hydrogen tetrachloroaurate is mixed with solution of tetraoctylammonium bromide (TOAB) in toluene. TOAB acts as a transfer agent. $AuCl_4^-$ will be transferred from aqueous phase to organic phase after vigorously stirring. Then sodium borohydride will be added in to the solvent. Sodium borohydride will reduce $AuCl_4^-$ to Au atoms. Au atoms will nucleate and form clusters. Bifunctional organic molecules like dodecanethiol are added into the organic phase. Bifunctional organic molecules prevent the initial gold nuclei from sintering into bulk material.

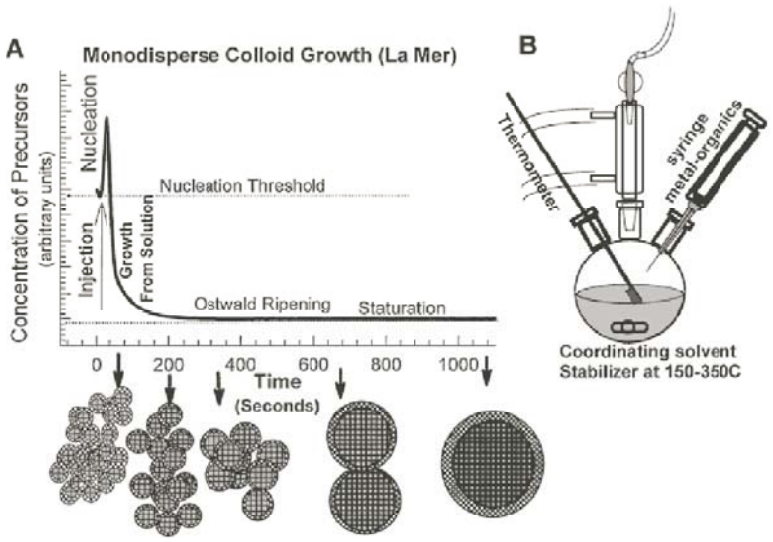

Figure 4: (A) The concentration of precursors is shown with time for different stages in the synthesis of nanocrystals. Bottoms show how the size of nanocrystals changes with time. (B) The apparatus for nanocrystals synthesis [45].

1.3 Purpose of This Work

This work is to understand the dynamic processes in tunneling experiments, especially of small gold nanocrystals. A tunneling model based on double junction model will be developed. This model emphasizes the importance of excited states and discrete energy levels. These excited states include not only states with net charges but also states which are neutral in charge. We are interested at how the dynamic balance of states affects tunneling dI/dV spectra. We will also change parameters, like tunneling rates, ratio of charging energy to level spacing of nanocrystals, relaxation rates, to see how these parameters change the shape of dI/dV curves. The ultimate goal is to know how to accurately extract useful information about the nanocrystal from measured dI/dV curves.

In order to understand the effect of energy relaxation on dI/dV curves, Ballistic electron emission spectroscopy (BEES) is also modeled. Measured BEES current versus voltage curves were used to extract transmission rates across the interface between a thin gold film and the silicon (111) surface. We don't model this process because it needs to do some full band calculation of electron transport in silicon. It is a too big and not proper to be a part of this work. Once the transmission rate across the interface of gold and silicon is

known, it will be combined with the tunneling model to get the BEES I-V. We focus on two things. One is how to understand the tunneling dI/dV well with the help from BEES I-V. Second is how the relaxation inside the nanocrystal affects the BEES I-V. We hope we can extract some information about the relaxation from the BEES I-V combined with tunneling spectroscopy.

The main part of this work was redesigning a low temperature and ultra high vacuum STM to incorporate the capability of BEEM and BEES. Both the sample stage and sample holder were re-designed to introduce the BEEM electrode. Good Schottky junction of Au-Si(111) was developed to make BEEM samples. Gold nanocrystals were attached to the surface by alkanedithiol. STS and BEES were measured.

Work was also performed on electronic states calculation of semiconductor nanocrystals using envelope function method. This work was to estimate qualitatively the energy levels inside semiconductor nanocrystals of $4 \sim 6$ nm in diameter. Multi-band envelope function method was applied to quantum-well-quantum-dot structures. The main interest was to see how the band gap difference affects the electronic density of states.

CHAPTER II

ELECTRONIC STRUCTURE CALCULATION OF SEMICONDUCTOR NANOCRYSTALS

2.1 Introduction to Envelope Function Method

The quantum confinement effect is relative easier to observe in semiconductor nanocrystals as compared with metal nanocrystals. This is due to the small effective masses of electrons and holes in semicondcutors. As seen in the previous chapter, CdSe nanocrystals with diameter of 8 nm have different absorption edges compared with bulk material while gold nanocrystals with 8nm diameter are thought to be bulk like. Nanocrystals of this size have over one hundred atoms. They have the same lattice structure as the bulk material but lose the translation symmetry. In this range, tight-binding method and envelope function method are two simple and feasible ways to calculate the electron levels of semiconductor nanocrystals.

Envelope function method is originally developed to calculate the response of carriers to weak and slow varying external perturbation, like electromagnetic fields or impurity atoms induced potential perturbation [43]. The main idea is that the perturbed wave function is a product of a slow varying part (the envelope) and a fast oscillating part with the lattice constant as the period. Usually, Bloch wave functions at band extrema are chosen as the fast oscillating part (for semiconductors, only at the band extrema there are free carriers). For example, the Bloch function of conduction band at Γ point of the Brillouin zone is often chosen as the fast oscillating part. The argument for this idea is very simple. Assuming the new Hamiltonian H is the original Hamiltonian H_0 plus the external perturbation $U(r)$, It is nature to build the new eigenfunctions of H with the eigenfunctions of H_0.

$$H = H_0 + U(r) \tag{2}$$

$$\Psi(r) = \int c(k) e^{ikr} u_{nk}(r) dk \tag{3}$$

Here $e^{ikr}u_{nk}(r)$ is the Bloch wave function for band n with momentum k. u_{nk} is a periodic function of the lattice. u_{nk} can be expanded with a complete set $u_{n'k_0}$ which have the same periodicity [27, 43]

$$u_{nk} = \sum_{n'} b_{nn'}(k) u_{n'k_0} \tag{4}$$

Here n' refers to other bands. Insert the above equation into Eq. 3, we have:

$$\Psi(r) = \sum_{n'} \int c(k) e^{ikr} b_{nn'}(k) u_{n'k_0} dk \tag{5}$$

If we introduce new functions $f_{n'}(r)$

$$f_{n'}(r) = \int c(k) e^{ikr} b_{nn'}(k) dk \tag{6}$$

Now we can rewrite $\Psi(r)$ as

$$\Psi(r) = \sum_{n'} f_{n'}(r) u_{n'k_0}(r) \tag{7}$$

$f_{n'}(r)$ is the envelope function mentioned above. If $U(r)$ is not very strong and the inter-band scattering can be neglected, we have:

$$\Psi(r) \simeq f_n(r) u_{nk_0}(r) \tag{8}$$

The problem of finding the solution of $\Psi(r)$ is transformed to the problem of finding the solution of $f_n(r)$.

$$(H_0 + U(r)) f_n(r) u_{nk_0}(r) = E f_n(r) u_{nk_0}(r) \tag{9}$$

If $E_n(k)$ is the energy of the Bloch state of the band n with momentum k, then $f_n(r)$ has the following equation [43]

$$(E_n(-i\nabla) + U(r)) f_n(r) = E f_n(r) \tag{10}$$

In the above equation, $(-i\nabla)$ replaces k in $E_n(k)$.

The replacement of k with $-i\nabla$ is related to the $k \cdot p$ method for calculating bulk band structures. Actually the procedure of $k \cdot p$ is almost the same as that of the envelope

function method [15, 21]. Everywhere there is a $-i\nabla$ in envelope function method, there is a corresponding k term in the $k \cdot p$ calculation. All the other parameters are the same.

Although envelope function method has great success in calculating electronic states of quantum well structures, there are many controversies about this method. Early days, people just replaced the k in $E_n(k)$ with operator $-i\nabla$ to get the equations for envelope functions. This is quite questionable especially for inhomogeneous structures. The problem comes from the proper choice of boundary conditions at the interface of two different materials. For single band envelope function, one of the boundary condition is that the envelope function should be continuous across the interface. The equation for the second boundary condition is achieved from integrating the equation for the envelope function across the interface. The resulting equation is an equation of the first derivative of the envelope function. It is obvious that the following two equations will have different boundary conditions if $m^*(r)$ is different at two sides of the interface.

$$-\frac{\hbar^2}{2m^*(r)}\nabla^2 f(r) + ... = Ef(r)$$

$$-\nabla^2(\frac{\hbar^2}{2m^*(r)}f(r)) + ... = Ef(r)$$

People have tried different approaches to this operator ordering problem. One of them is to write the operators symmetrical. For example:

$$\frac{\hbar^2 k^2}{2m^*(r)} \rightarrow -i\frac{\hbar^2}{2}\left(\frac{1}{2m^*(r)}\nabla^2 + \nabla^2\frac{1}{2m^*(r)}\right)$$

Another approach is to derive the equation for the envelope function directly from Schrodinger's equation [26, 31]. The latter approach has more solid physics ground. But the latter approach loses the simplicity.

But the correct ordering doesn't mean a correct boundary condition. It is still questionable to get the second boundary condition which contains the first derivative by integrating equations of envelope functions. Originally the envelope function is for slowly varying external perturbation. But for nanocrystals or quantum wells, there are abrupt changes of material properties at the interface. The change of potential is not slow and gentle. So it is not known if the envelope function method is valid or not close to the interface. If the

differential form of the envelope function doesn't exist there, the second boundary condition is still missing. In Burt's seminal papers [24–26], he proved that the exact envelope function and its first order derivative are both continuous at the abrupt heterostructure interface. He also showed that approximations would introduce "kinks" for envelope functions at the interface. These kinks are consistent with the discontinuity of the first order derivative due to the second boundary condition and discontinuity of the effective mass.

For wide band gap materials and weak size confinement, single band envelope function of the conduction band is good enough to calculate the discrete electron energy levels above the conduction band minimum. The band is parabolic near an extremum, so the kinetic operator for the envelope function is very simple, $-\hbar^2\nabla^2/2m^*$, where m^* is the effective mass of electron at the band minimum. But if the confinement is very strong, the energy of these levels (subbands) are significantly higher than the conduction band edge. At that high energy, the E(k) relation of the conduction band is not parabolic. An energy-dependent effective mass should replace the energy independent effective mass in order to obtain accurate results.

States in the valence bands are different. Usually the valence bands of bulk materials are degenerate at the valence band maximum. Figure 5 shows the band structure of zinc blende semiconductors near the Γ point. The heavy hole bands and light hole bands are degenerate at the Γ point. If the spin-orbit splitting energy Δ_{so} is bigger than the energy due to quantum confinement, then the quantized states in valence band can be constructed from both the light-hole bands and the heavy-hole bands of the bulk. So there are four envelope functions, two for the light hole bands and two for the heavy hole bands if spin is taken into account. If Δ_{so} is very small and the energy due to quantum confinement is comparable with Δ_{so}, then all three type valence bands have to be used to construct the quantized valence states. There would be six envelope functions.

For small band gap materials like HgS in strong confinement regime, we would expect there is strong coupling between the conduction band and the valence bands. The quantized states have to be constructed from both the conduction bands and the valence bands. This is the so called eight-band scheme [48].

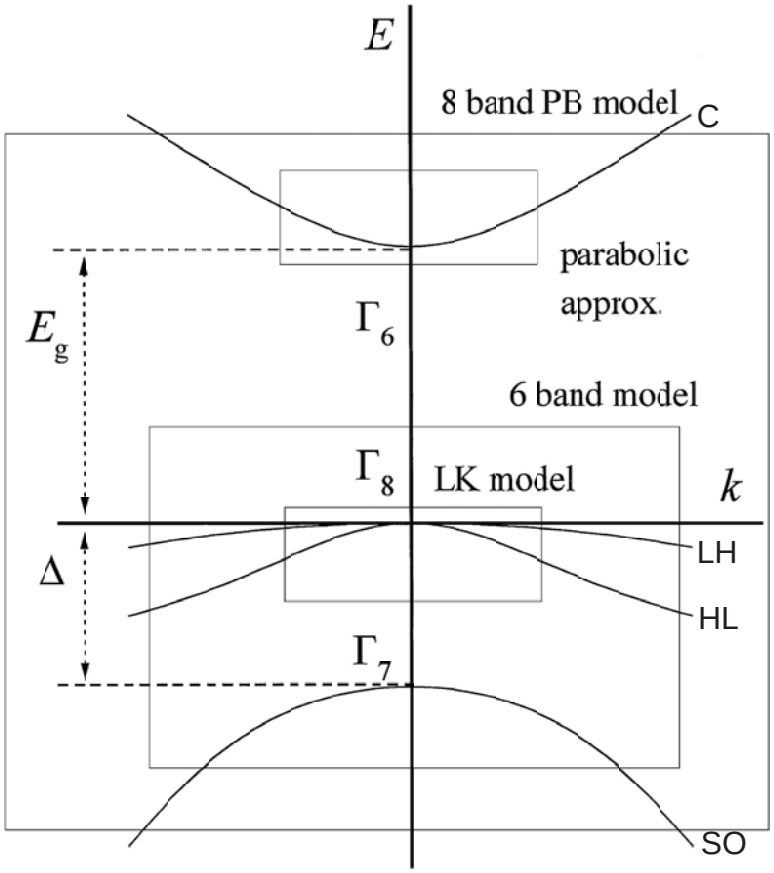

Figure 5: The bulk band structure of zinc blende semiconductors. The valence bands have six-fold degeneracy at the Γ point of the Brillouin zone if not considering the spin-orbit interaction. The spin-orbit interaction separates the valence bands to three bands: light hole(LH), heavy hole(HH), and spin-orbit(SO) split band. E_g is the band gap. Δ is the spin-orbit split energy. Light hole and heavy hole bands are still degenerate at the Γ point [29].

In the following section, we will follow Efros and Rosen's work [29] to calculate the quantized energy levels in CdS/HgS/CdS quantum-well-quantum-dot nanocrystals.

2.2 CdS/HgS/CdS QWQD Semiconductor Nanocrystals

In this section, we will develop eight-band calculation for CdS/HgS/CdS nanocrystals with quantum-well-quantum-dot (QWQD) structure. Recently nanocrystals with QWQD structures have been synthesized by the colloidal method. The bulk band gap of CdS is 2.56 eV. HgS is a small band gap material. Its band structure is not very clear. Some work claims that the conduction band minimum and the valence band maximum are inverted [49]. So it is a "negative" band gap material. Since HgS is a narrow band gap material, we would expect there to be strong coupling between conduction band and valence bands for quantized energy levels. If the energy levels are close to the band edges of HgS, they are be deeply in the band gap of bulk CdS. We also expect that the conduction band and valence bands of CdS are involved in the formation of discrete energy states.

We assume CdS/HgS/CdS nanocrystals have zinc-blende structure. For bulk zinc-blende structure, both the conduction band minimum and the valence band maximum are at the Γ point. $|S\rangle$ is the Bloch wave function at Γ for the conduction band. $|X\rangle$, $|Y\rangle$, and $|Z\rangle$, are the three degenerate valence band Bloch wave functions at Γ. In order to take the spin degeneracy and the spin-orbit interaction into account, the following eight wave functions are used as the basis for the eight-band envelope-function calculation.

$$
\begin{aligned}
u^c_{1/2} &= |S\uparrow\rangle \\
u^c_{-1/2} &= |S\downarrow\rangle \\
u^v_{3/2,3/2} &= \frac{1}{\sqrt{2}}|(X+iY)\uparrow\rangle \\
u^v_{3/2,1/2} &= \frac{i}{\sqrt{6}}|(X+iY)\downarrow -2Z\uparrow\rangle \\
u^v_{3/2,-1/2} &= \frac{1}{\sqrt{6}}|(X-iY)\uparrow +2Z\downarrow\rangle \\
u^v_{3/2,-3/2} &= \frac{i}{\sqrt{2}}|(X-iY)\downarrow\rangle
\end{aligned}
$$

$$
\begin{aligned}
u^v_{1/2,1/2} &= \frac{1}{\sqrt{3}}|(X+iY)\downarrow + Z\uparrow\rangle \\
u^v_{1/2,-1/2} &= \frac{i}{\sqrt{3}}|-(X-iY)\uparrow + Z\downarrow\rangle
\end{aligned} \tag{11}
$$

They are the fast oscillating parts of wave functions in envelope function method.

Above eight base functions are written in the form of $u^{c,v}_{J,J_z}$. c is for the conduction band and v is for the valence bands. J is the total angular momentum and J_z is the z component. The basis functions for heavy-hole and light-hole bands have angular momentum 3/2. The spin-orbit split band has angular momentum 1/2. The energy difference between $u^v_{3/2,j}$ and $u^v_{1/2,j}$ is the spin-orbit splitting energy, Δ_{so}. Based on these functions, we can write the wave function of a quantized level as

$$
\Psi(r) = \sum_{j_z=-1/2}^{1/2} f^c_{j_z} u^c_{j_z} + \sum_{j_z=-3/2}^{3/2} f^v_{3/2,j_z} u^v_{3/2,j_z} + \sum_{j_z=-1/2}^{1/2} f^v_{1/2,j_z} u^v_{1/2,j_z} \tag{12}
$$

For QWQD nanocrystals, we expand the wave functions with basis functions in each layer. The basis functions have the same form in all layers. The f-coefficients are different. Once the general solution with unknown coefficients found, envelope functions in different layers are connected together using proper boundary conditions. Until this point, there are still unknown coefficients and the unknown energy eigenvalue. In order to solve for the energy eigenvalues, the physical restriction of the wave function have to be considered. A solution of the wave function with physics meaning has to be finite at the core $r = 0$. In the vacuum, the wave function has to decrease exponentially. Only discrete energy values meet these two requirements for wave functions. These discrete energy values are the eigenvalues of the system. Once the eigenvalues are known, all coefficients for the envelope functions can be found.

In each layer, the equations for envelope functions are [29]:

$$\begin{pmatrix}
E_g+\frac{\alpha}{2m_0}p^2 & 0 & \frac{i}{\sqrt{2}}Vp_+ & \sqrt{\frac{2}{3}}Vp_z & \frac{i}{\sqrt{6}}Vp_- & 0 & \frac{i}{\sqrt{3}}Vp_z & \frac{1}{\sqrt{3}}Vp_- \\
0 & E_g+\frac{\alpha}{2m_0}p^2 & 0 & -\frac{1}{\sqrt{6}}Vp_+ & i\sqrt{\frac{2}{3}}Vp_z & -\frac{1}{\sqrt{2}}Vp_- & \frac{i}{\sqrt{3}}Vp_+ & -\frac{1}{\sqrt{3}}Vp_z \\
-\frac{i}{\sqrt{2}}Vp_- & 0 & -(P+Q) & -L & -M & 0 & -i\sqrt{\frac{1}{2}}L & i\sqrt{2}M \\
\sqrt{\frac{2}{3}}Vp_z & -\frac{1}{\sqrt{6}}Vp_- & -L^* & -(P-Q) & 0 & -M & i\sqrt{2}Q & -i\sqrt{\frac{3}{2}} \\
-\frac{i}{\sqrt{6}}Vp_+ & -i\sqrt{\frac{2}{3}}Vp_z & -M^* & 0 & -(P-Q) & L & i\sqrt{\frac{3}{2}}L^* & i\sqrt{2}Q \\
0 & -\frac{1}{\sqrt{2}}Vp_+ & 0 & -M^* & L^* & -(P+Q) & i\sqrt{2}M^* & i\sqrt{\frac{1}{2}}L^* \\
-\frac{i}{\sqrt{3}}Vp_z & -\frac{i}{\sqrt{3}}Vp_- & i\sqrt{\frac{1}{2}}L^* & -i\sqrt{2}Q & -i\sqrt{\frac{3}{2}}L & -i\sqrt{2}M & -\Delta_{so}-P & 0 \\
\frac{1}{\sqrt{3}}Vp_+ & -\frac{1}{\sqrt{3}}Vp_z & -i\sqrt{2}M & i\sqrt{\frac{3}{2}}L^* & -i\sqrt{2}Q & -i\sqrt{\frac{1}{2}}L & 0 & -\Delta_{so}-P
\end{pmatrix}$$

$$\times \begin{pmatrix} f^c_{1/2} \\ f^c_{-1/2} \\ f^v_{3/2,3/2} \\ f^v_{3/2,1/2} \\ f^v_{3/2,-1/2} \\ f^v_{3/2,-3/2} \\ f^v_{1/2} \\ f^v_{-1/2} \end{pmatrix} = E \cdot \begin{pmatrix} f^c_{1/2} \\ f^c_{-1/2} \\ f^v_{3/2,3/2} \\ f^v_{3/2,1/2} \\ f^v_{3/2,-1/2} \\ f^v_{3/2,-3/2} \\ f^v_{1/2} \\ f^v_{-1/2} \end{pmatrix} \tag{13}$$

The definitions of the operators are:

$$\begin{aligned}
p_\pm = p_x \pm ip_y, \quad & p_\perp^2 = p_x^2 + p_y^2 \\
P = \frac{\gamma_1}{2m_0}p^2, \quad & Q = \frac{\gamma}{2m_0}(p_\perp^2 - p_z^2) \\
L = \frac{-i\sqrt{3}\gamma}{m_0}p_z p_-, \quad & M = \frac{\sqrt{3}\gamma}{2m_0}p_-^2
\end{aligned} \tag{14}$$

E_g is the band gap between the conduction band minimum and light-hole, heavy-hole band maximum. Δ_{so} is the spin-orbit split energy. V is the matrix element $-i\langle S|p_z|Z\rangle/m_0$. The contributions of remote bands to the conduction band, the HH band, the LH band, and the SO band are included by parameters α, γ, γ_1. The inclusion is approximated by second order perturbation. These parameters are layer-dependent.

The above Hamiltonian for envelope functions has used the spherical approximation. Terms which are anisotropic have been modified to be spherical. Therefore the total angular momentum, the angular momentum of the envelope function plus the the angular

momentum of basis functions in Eq. 11, are good quantum numbers. Efros and Rosen [29] re-wrote the wave functions as

$$\Psi^{\pm}_{j,m}(r) = R^{\pm}_c(r) \sum_{\mu=-1/2}^{1/2} \Omega^c_\mu u^c_\mu + \sum_{i=1,2} R^{\pm}_{hi}(r) \sum_{\mu=-3/2}^{3/2} \Omega^{hi}_\mu u^v_{3/2,\mu} + R^{\pm}_s \sum_{\mu=-1/2}^{1/2} \Omega^s_\mu u^v_{1/2,\mu} \quad (15)$$

Here $\pm$ refers to odd or even states. j is the total angular momentum. $R^{\pm}_c$ is the radial part of the envelope function of conduction band. $R^{\pm}_{hi}$ are for heavy hole and light hole bands. $R^{\pm}_s$ is for the spin-orbit splitting band. The Ωs for even states are :

$$\Omega^+_c = \begin{pmatrix} \sqrt{\frac{j+m}{2j}} Y_{j-1/2,m-1/2} \\ \sqrt{\frac{j-m}{2j}} Y_{j-1/2,m+1/2} \end{pmatrix} \quad (16)$$

$$\Omega^+_{h1} = \frac{1}{\sqrt{2j(2j+2)(2j+3)}} \begin{pmatrix} \sqrt{3(j+m)(j-m+1)(j-m+2)} Y_{j+1/2,m-3/2} \\ i(j+3m)\sqrt{j-m+1} Y_{j+1/2,m-1/2} \\ (j-3m)\sqrt{j+m+1} Y_{j+1/2,m+1/2} \\ i\sqrt{3(j-m)(j+m+1)(j+m+2)} Y_{j+1/2,m+3/2} \end{pmatrix} \quad (17)$$

$$\Omega^+_{h2} = \frac{1}{\sqrt{2j(2j-1)(2j-2)}} \begin{pmatrix} -\sqrt{(j+m)(j+m-1)(j+m-2)} Y_{j-3/2,m-3/2} \\ i\sqrt{3(j-m)(j+m-1)(j+m)} Y_{j-3/2,m-1/2} \\ \sqrt{3(j+m)(j-m)(j-m-1)} Y_{j-3/2,m+1/2} \\ -i\sqrt{(j-m)(j-m-1)(j-m-2)} Y_{j-3/2,m+3/2} \end{pmatrix} \quad (18)$$

$$\Omega^+_s = \begin{pmatrix} \sqrt{\frac{j-m+1}{2(j+1)}} Y_{j+1/2,m-1/2} \\ -i\sqrt{\frac{j+m+1}{2(j+1)}} Y_{j+1/2,m+1/2} \end{pmatrix} \quad (19)$$

For odd states we have

$$\Omega^-_c = \begin{pmatrix} \sqrt{\frac{j-m+1}{2j+2}} Y_{j+1/2,m-1/2} \\ \sqrt{\frac{j+m+1}{2j+2}} Y_{j+1/2,m+1/2} \end{pmatrix} \quad (20)$$

$$\Omega^-_{h1} = \frac{1}{\sqrt{2j(2j+2)(2j-1)}} \begin{pmatrix} \sqrt{3(j+m)(j-m+1)(j+m-1)} Y_{j-1/2,m-3/2} \\ -i(j-3m+1)\sqrt{j+m} Y_{j-1/2,m-1/2} \\ (j+3m+1)\sqrt{j-m} Y_{j-1/2,m+1/2} \\ -i\sqrt{3(j+m+1)(j-m)(j-m-1)} Y_{j-1/2,m+3/2} \end{pmatrix} \quad (21)$$

$$\Omega^-_{h2} = \frac{1}{\sqrt{2(j+1)(2j+3)(2j+4)}} \begin{pmatrix} -\sqrt{(j-m+1)(j-m+2)(j-m+3)}Y_{j+3/2,m-3/2} \\ -i\sqrt{3(j+m+1)(j-m+2)(j-m+1)}Y_{j+3/2,m-1/2} \\ \sqrt{3(j-m+1)(j+m+1)(j+m+2)}Y_{j+3/2,m+1/2} \\ i\sqrt{(j+m+1)(j+m+2)(j+m+3)}Y_{j+3/2,m+3/2} \end{pmatrix} \tag{22}$$

$$\Omega^-_s = \begin{pmatrix} \sqrt{\frac{j+m}{2j}}Y_{j-1/2,m-1/2} \\ i\sqrt{\frac{j-m}{2j}}Y_{j-1/2,m+1/2} \end{pmatrix} \tag{23}$$

The combinations in Eq. 15 make the wave function an eigenfunction of total angular momentum j and its z component j_z

Inserting the above equations into Eq. 13, we get the equations for the radial parts of the envelope functions:

$$\begin{aligned}
[\epsilon_g - \epsilon - \alpha\Delta_{j-1/2}]R^+_c + \frac{\upsilon}{\sqrt{6}}\sqrt{1+3\eta^+_j}A^-_{j+1/2}R^+_{h1} & \\
-\frac{\upsilon}{\sqrt{2}}\sqrt{1-\eta^+_j}A^+_{j-3/2}R^+_{h2} + \frac{\upsilon}{\sqrt{3}}A^-_{j+1/2}R^+_s &= 0 \\
\frac{\upsilon}{\sqrt{6}}\sqrt{1+3\eta^+_j}A^+_{j-1/2}R^+_c + [[\gamma_1 - \gamma(1-3\eta_j+)]\Delta_{j+1/2} - \epsilon]R^+_{h1} & \\
+\gamma\sqrt{3[1+2\eta^+_j - 3(\eta^+_j)^2]}A^{+2}_{j-3/2}R^+_{h2} + \gamma\sqrt{2(1+3\eta^+_j)}\delta_{j+1/2}R^+_s &= 0 \\
-\frac{\upsilon}{2}\sqrt{1-\eta^+_j}A^-_{j-1/2}R^+_c + \gamma\sqrt{3[1+2\eta^+_j - 3(\eta^+_j)^2]}A^{-2}_{j+1/2}R^+_{h1} & \\
+[[\gamma_1 + \gamma(1-3\eta^+_j)]\Delta_{j-3/2} - \epsilon]R^+_{h2} + \gamma\sqrt{6(1-\eta^+_j)}A^{-2}_{j+1/2}R^+_s &= 0 \\
\frac{\upsilon}{\sqrt{3}}A^+_{j-1/2}R^+_c + \gamma\sqrt{2(1+3\eta^+_j)}\Delta_{j+1/2}R^+_{h1} & \\
+\gamma\sqrt{6(1-\eta^+_j)}A^{+2}_{j-3/2}R^+_{h2} + [\gamma_1\Delta_{j+1/2} - \delta - \epsilon]R^+_s &= 0
\end{aligned} \tag{24}$$

for even states and

$$\begin{aligned}
[\epsilon_g - \epsilon - \alpha\Delta_{j-1/2}]R^-_c + \frac{\upsilon}{\sqrt{6}}\sqrt{1+3\eta^-_j}A^-_{j+1/2}R^-_{h1} & \\
-\frac{\upsilon}{\sqrt{2}}\sqrt{1-\eta^-_j}A^+_{j-3/2}R^-_{h2} + \frac{\upsilon}{\sqrt{3}}A^-_{j+1/2}R^-_s &= 0 \\
\frac{\upsilon}{\sqrt{6}}\sqrt{1+3\eta^-_j}A^+_{j-1/2}R^-_c + [[\gamma_1 - \gamma(1-3\eta^-_j)]\Delta_{j+1/2} - \epsilon]R^-_{h1} & \\
+\gamma\sqrt{3[1+2\eta^-_j - 3(\eta^-_j)^2]}A^{+2}_{j-3/2}R^-_{h2} + \gamma\sqrt{2(1+3\eta^-_j)}\delta_{j+1/2}R^-_s &= 0
\end{aligned}$$

$$
\begin{aligned}
-\frac{\upsilon}{2}\sqrt{1-\eta_j^-}\,A^-_{j-1/2}R^-_c + \gamma\sqrt{3[1+2\eta_j^- - 3(\eta_j^-)^2]}A^{-2}_{j+1/2}R^-_{h1} & \\
+[[\gamma_1+\gamma(1-3\eta_j^-)]\Delta_{j-3/2} - \epsilon]R^-_{h2} + \gamma\sqrt{6(1-\eta_j^-)}A^{-2}_{j+1/2}R^-_s &= 0 \\
\frac{\upsilon}{\sqrt{3}}A^+_{j-1/2}R^-_c + \gamma\sqrt{2(1+3\eta_j^-)}\Delta_{j+1/2}R^-_{h1} & \\
+\gamma\sqrt{6(1-\eta_j^-)}A^{+2}_{j-3/2}R^-_{h2} + [\gamma_1\Delta_{j+1/2} - \delta - \epsilon]R^-_s &= 0
\end{aligned}
\tag{25}
$$

for odd sates with $\eta_j^+ = 1/(2j)$, $\eta_j^- = 1/(2j+2)$, $\epsilon_g = 2m_0E_g/\hbar^2$, $\delta = 2m_0\Delta_{so}/\hbar^2$, $\upsilon = 2m_0V/\hbar$, $\epsilon = 2m_0E/\hbar^2$. The definitions for operators $A_l^\pm$ and Δ are

$$
A_l^+ = -\frac{\partial}{\partial r} + \frac{l}{r}, \quad A_l^- = \frac{\partial}{\partial r} + \frac{l+1}{r} \tag{26}
$$

$$
\Delta_l = \frac{\partial^2}{\partial^2 r} + \frac{2}{r}\frac{\partial}{\partial r} - \frac{l(l+1)}{r^2} \tag{27}
$$

When acting on spherical Bessel functions $j_l(x)$, $y_l(x)$, $i_l(x)$, and $k_l(x)$, $A_l^\pm$ and Δ_l have the following properties:

$$
\begin{aligned}
A_l^\pm j_l(kr) &= k j_{l\pm1}(kr) \\
\Delta_l j_l(kr) &= -k^2 j_l(kr)
\end{aligned}
\tag{28}
$$

$$
\begin{aligned}
A_l^\pm y_l(kr) &= k y_{l\pm1}(kr) \\
\Delta_l y_l(kr) &= -k^2 y_l(kr)
\end{aligned}
\tag{29}
$$

$$
\begin{aligned}
A_l^\pm i_l(kr) &= \mp k i_{l\pm1}(kr) \\
\Delta_l j_l(kr) &= k^2 j_l(kr)
\end{aligned}
\tag{30}
$$

and

$$
\begin{aligned}
A_l^\pm k_l(kr) &= \pm k k_{l\pm1}(kr) \\
\Delta_l k_l(kr) &= k^2 k_l(kr)
\end{aligned}
\tag{31}
$$

In order to find the solutions of Eq. 24 and 25, we assume that the solutions are composed of spherical Bessel functions. For example, the following is used a trial solution for even states.

$$R_c^+(r) = c1\ j_{j-1/2}(kr), \qquad R_{h1}^+(r) = c2\ j_{j+1/2}(kr)$$
$$R_{h2}^+(r) = c3\ j_{j-3/2}(kr), \qquad R_s^+(r) = c4\ j_{j+1/2}(kr) \tag{32}$$

Inserting the above trial functions into Eq. 24, we get four coupled equations which contain k, ϵ, c_i. Four spherical Bessel functions with different order in each equation will be transformed to one by operators $A_l^{\pm}$ and Δ_l. This common spherical Bessel function can be discarded from both sides of the equation. The coupled equations become equations for four coefficients.

$$\begin{pmatrix} \epsilon_g - \epsilon + \alpha k^2 & \frac{v}{\sqrt{6}}\sqrt{1+3\eta_j^+}k & -\frac{v}{\sqrt{2}}\sqrt{1-\eta_j^+}k & \frac{v}{\sqrt{3}}k \\ \frac{v}{\sqrt{6}}\sqrt{1+3\eta_j^+}k & -[\gamma_1 - \gamma(1-3\eta_j+)]k^2 - \epsilon & \gamma\sqrt{3[1+2\eta_j^+ - 3(\eta_j^+)^2]}k^2 & -\gamma\sqrt{2(1+3\eta_j^+)}k^2 \\ -\frac{v}{2}\sqrt{1-\eta_j^+}k & \gamma\sqrt{3[1+2\eta_j^+ - 3(\eta_j^+)^2]}k^2 & -[\gamma_1 + \gamma(1-3\eta_j^+)]k^2 - \epsilon & \gamma\sqrt{6(1-\eta_j^+)}k^2 \\ \frac{v}{\sqrt{3}}k & -\gamma\sqrt{2(1+3\eta_j^+)}k^2 & \gamma\sqrt{6(1-\eta_j^+)}k^2 & -\gamma_1 k^2 - \delta - \epsilon \end{pmatrix} \cdot \begin{pmatrix} c1 \\ c2 \\ c3 \\ c4 \end{pmatrix} = \begin{pmatrix} 0 \\ 0 \\ 0 \\ 0 \end{pmatrix} \tag{33}$$

In order to get a non-trivial solution for those coefficients, the determinant of the matrix at the left side of the above equation has to be zero. This results in a characteristic equation which relates k to ϵ. For one fixed ϵ, there are four solutions for k^2. sometimes four k^2 can't all be positive. For each positive k^2, we have one solution for four coefficients. But we can get two solutions for envelope functions in Eq. 24. This is because if we use $y_l(kr)$ in Eq. 32, we will get the same equation for k^2 and same equations for coefficients. Because $j_l(kr)$ and $y_l(kr)$ are independent of each other, from the same set of coefficients we can have two independent solutions of the radial parts. In most cases, four k^2 can't be all positive. In order to get enough independent solutions for the radial parts of envelope functions, we also use $i_l(kr)$ and $k_l(kr)$ as trial functions in Eq. 32. $i_l(kr)$ and $k_l(kr)$ will have the same

equation for k^2. The good thing is that the sum of number of positive k^2 when assuming $j_l(kr)$ or $y_l(kr)$ and number of positive k^2 when assuming $i_l(kr)$ or $k_l(kr)$ is always 4. Values of positive k^2 in two cases are different. Therefore we always have four different positive k and eight independent solutions for the radial parts of envelope functions when ϵ is fixed.

The general solution of radial parts in Eq. 24 or 25 is the linear superposition of eight independent solutions mentioned above. Therefore, in each layer, we have eight unknown variables. Each variable is the the weight of the corresponding independent solution of Eq. 33 in the general solution. In order to connect the solutions in neighboring layers together, we need boundary conditions. Since we assume basis functions are the same for semiconductors with the same lattice structure. So the the continuity of the wave function requires the continuity of the envelope functions across each interface. There are four envelope functions in Eq. 15. So we have four continuity equations as boundary conditions.

Other boundary conditions come from integrating Eq. 24 or Eq. 25 across the interface between neighboring layers. The integration is made in a infinitely thin region $(-d, +d), d \rightarrow 0$, which contains the interface. The resulting equations only contain the first derivatives of the radial parts of envelope functions at two sides. Therefore we have another four equations as boundary conditions. At each interface between two neighboring layers, there are total eight equations as boundary conditions. At each side, there are eight unknown variables. Let S be a vector which has eight unknown variables as its elements. Then eight equations as boundary conditions can be written as:

$$B^I(r) \cdot S^I = B^{II}(r) \cdot S^{II} \tag{34}$$

B^I and B^{II} are 8×8 matrixes. I and II refer to two sides of the interface. The r means that the B matrix depends on the position of the interface.

The boundary conditions at the surface of the nanocrystals are different from those mentioned above. We don't consider the effect of the capping layer. So nanocrystals are thought to be exposed to the vacuum directly. Since in vacuum there is no lattice structure,

we assume the equation for each envelope function is:

$$-\frac{\hbar^2}{2m_0}\nabla^2\Psi(r) + U_0\Psi(r) = E\Psi(r) \tag{35}$$

U_0 is the vacuum level. For the eigenenergy we are looking for $U_0 > E$ is always true. Let

$$\kappa^2 = \frac{2m_0}{\hbar^2}(U_0 - E) \tag{36}$$

and

$$\Psi(r) = R_l(r)Y_l^m(\theta, \phi) \tag{37}$$

Then the solution for $R_l(r)$ is

$$R_l = a_l\ i_l(\kappa r) + b_l\ k_l(\kappa r) \tag{38}$$

a_l and b_l are two unknown coefficients to be determined by the boundary conditions. There are four radial parts in the nanocrystal. For each of them, we assume it matches to a solution in vacuum similar to R_l in Eq. 38. So we also have eight unknown variables in the vacuum. Each of these variables is a coefficient like a_l or b_l in Eq. 38. In order to connect the envelope functions in vacuum to those in the surface layer of the nanocrystal, we assume that the individual radial parts of the envelope function and its derivative are continuous across the surface boundary.

As shown in Fig. 6, vectors S are connected by B matrices.

$$\begin{aligned} B^1_{out} \cdot S_1 &= B^2_{in} \cdot S_2 \\ B^2_{out} \cdot S_2 &= B^3_{in} \cdot S_3 \\ B^3_{out} \cdot S_3 &= B^4 \cdot S_4 \end{aligned} \tag{39}$$

From above equations, we relate S_1 to S_4.

$$S_4 = T \times S_1 \tag{40}$$

where

$$T = (B^4)^{-1} \times B^3_{out} \times (B^{in}_3)^{-1} \times B^2_{out} \times (B^2_{in})^{-1} \times B^1_{out} \tag{41}$$

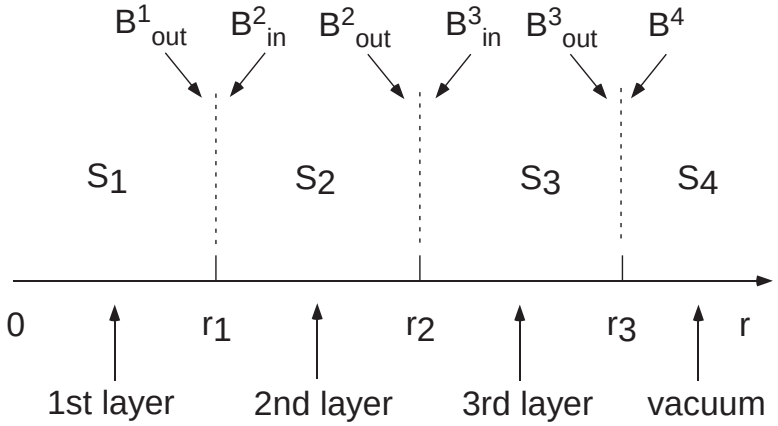

Figure 6: Boundaries for envelope functions. In each layer of nanocrystal, there are eight independent solutions. Each element of vector S is the weight of one independent solution in the general solution of the envelope function. At each interface, S_i and S_{i+1} are connected by matrix B^i_{out} and B^{i+1}_{in}.

Matrix T is a function of ϵ only (k's are expressed in ϵ.). In order to determine possible values for ϵ, we consider the restriction of the the envelope functions. As shown in Fig. 7, $y_l(kr)$ and $k_l(kr)$ will diverge at $r = 0$. So the solution for the radial parts of the envelope functions in the first layer should be composed of $j_l(kr)$ and $i_l(kr)$ only. For each positive k^2, one independent solution is $j_l(kr)$ or $i_l(kr)$ type and the other is $y_l(kr)$ or $k_l(kr)$ type. Therefore half of the elements of S_1 should be zero for a solution with physical meaning. In vacuum, the radial parts should decrease to zero at far distance from the the center. This means that the radial parts are composed only of $k_l(\kappa r)$ type solutions. So half of the elements of S_4 have to be zero. These two restrictions for S_1 and S_4 result in the following equation.

$$T' \cdot S'_1 = \begin{pmatrix} 0 \\ 0 \\ 0 \\ 0 \end{pmatrix} \tag{42}$$

Where vector S'_1 consists of the non-zero elements of S_1. The zeros at the right side of the above equation are the coefficients for solutions of $i_l(\kappa r)$ type in the vacuum. T' is a 4×4 matrix extracted from T. In order to get a non-trivial solution, the determinant of T' must

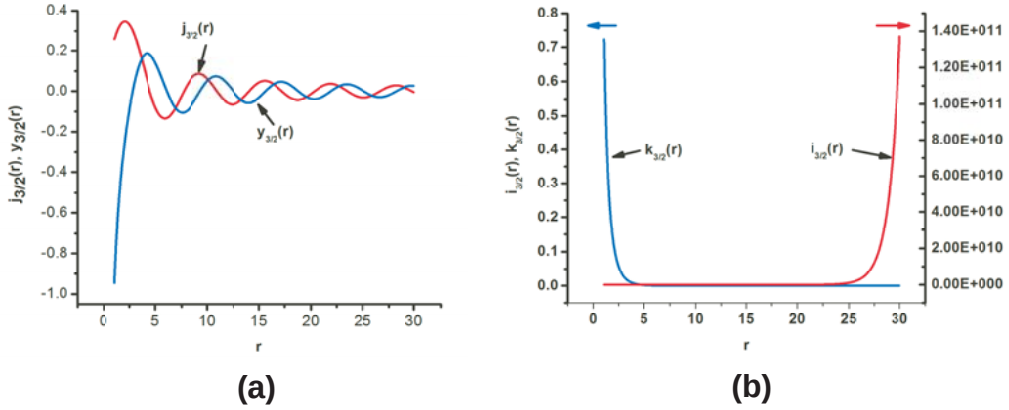

Figure 7: Spherical Bessel functions. (a) The first kind spherical Bessel function $j_{3/2}(r)$ and the second kind $y_{3/2}(r)$. (b) The modified first kind spherical Bessel function $i_{3/2}(r)$ and the modified second kind $k_{3/2}(r)$.

be zero. This determines the eigenvalues of ϵ. Once ϵ is known, S_1' is known. Then from Eq. 39, all of the S vectors can be calculated.

The band structure parameters used in our calculation are listed in Table 1. The band gap for HgS is 0.19 eV and positive (Bryant et. al. [23] got a positive band gap 0.201 ev by tight-binding calculation). All the other parameters are same as in [49]. In Fig. 8 and Fig. 9, the relation of e versus k is calculated using Eq. 24. The blue curves are like the "normal" dispersion of the $E(k)$ in bulk materials. For any value of e, there are four positive "k" values. Each value of k has two independent solutions. So total there are eight independent solutions of R's in Eq. 24 for each value of e. The number of total solutions meets the number of boundary condition equations.

Figure 10 shows the relative positions of band edges of CdS and HgS. A "flat band" condition is assumed for our calculation. The valence band offset between CdS and HgS is 0.93 eV [39]. We assume the vacuum level is 4.94 eV above the conduction band minimum of CdS. This value is relatively arbitrary. In the following, we calculate a three-layer quantum-well-quantum-dot nanocrystal. The core is CdS with a radius of 2.0 nm. The middle well is HgS with a thickness of 1.5 nm. The out layer is CdS with thickness of 0.5 nm.

In the calculation, we found it very difficult to find the exact solution of the eigenvalues

Table 1: Parameters for the eight-band calculation for HgS and CdS. Parameters are same as in [49] except the band gap of HgS [23].

	HgS	CdS
E_g	0.19 eV	2.56 eV
E_p	13.2 eV	21.0 eV
Δ	0.07 eV	0.07 eV
α	-1	-2.57
γ_1	0.35	-2.57
γ	-0.67	-0.75
α	1	2

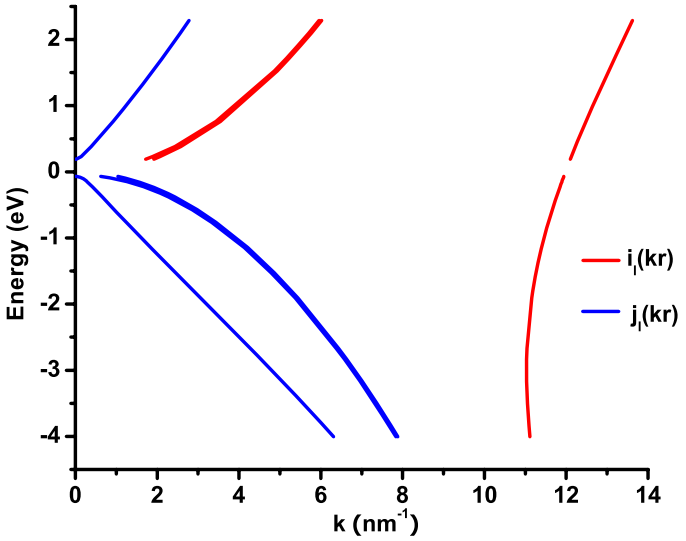

Figure 8: The E-k relation of HgS calculated using Eq. 24. The total angular momentum is $\frac{5}{2}$. At each point of energy, four real values for k are found by assuming the trial functions are $j_l(kr)$ or $i_l(kr)$. The red curves are for $i_l(kr)$ trial functions and the blue curves are for $j_l(kr)$ trial functions. Since the quantized energy levels will not be in the energy gap of HgS, only energy higher than conduction band minimum and lower than spin-orbit split band maximum is considered. Parameters used in the calculations are listed in Table 1.

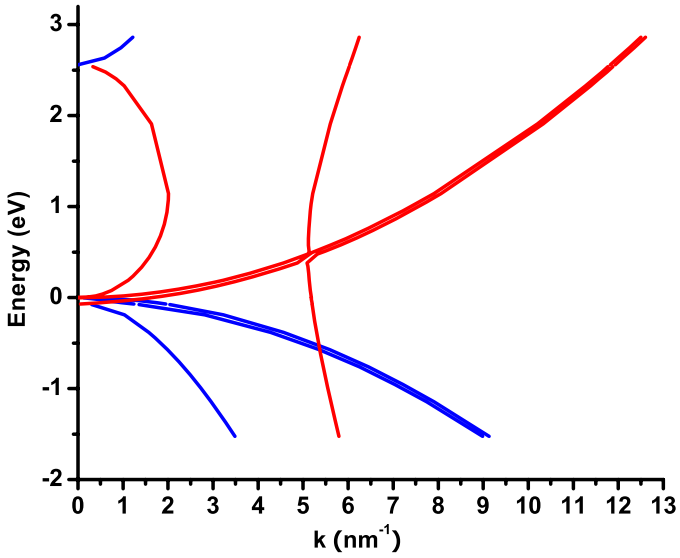

Figure 9: The E-k relation of CdS calculated using Eq. 24. The total angular momentum is $\frac{5}{2}$. The red curves are for $i_l(kr)$ trial functions and the blue curves are for $j_l(kr)$ trial functions. The parameters used in the calculation are listed in Table 1.

higher than the conduction band minimum. The eigenvalues are found by scanning E. At each E, the corresponding determinant of T' in Eq. 42 is calculated. Because the second type spherical Bessel functions and the modified second type spherical Bessel functions are involved, some of the matrices in Eq. 41 are "bad" matrices. Some of the elements are huge while others are very small. This makes the determinant of T' a large and rapidly varying function of E. It is difficult to find the roots of $det(T'(E)) = 0$. When we scan E with small steps, the eigenvalues interpolated between two successive values of e for which $det(T'(E))$ changes sign. The eigenvalues can be calculated with high accuracy, but it can be difficult to calculate the envelope functions since the exact zero of the determinant of T' in Eq. 42 is not found. Some of the eigenvalues are listed in Table 2.

The case for valence band states is better than the case for the conduction band. When the eigenenergy is below the spin-orbit split bands maximum of CdS, we can get both the eigenenergy and the envelope functions with high accuracy. This is because the envelope functions of valence band states have less components of exponentially increasing spherical

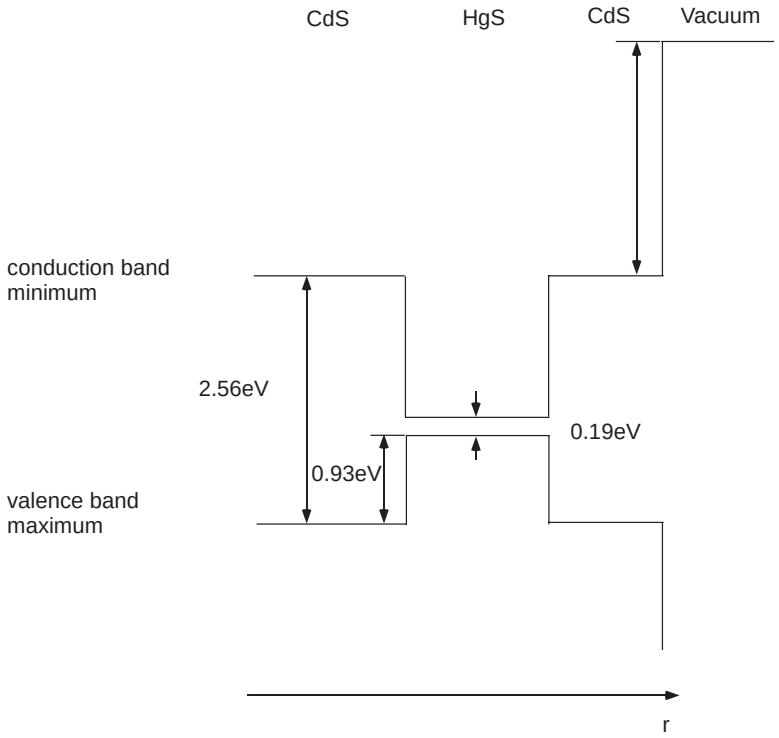

Figure 10: The band alignment for CdS/HgS/CdS system. The alignment is assumed to be in "flat band" condition. Any possible bend-bending effects are neglected here. A positive band gap is assumed for HgS. The energy barrier from the bottom of the CdS conduction band to the vacuum level is 4.94 eV.

Table 2: Eigenvalues of quantized states in CdS/HgS/CdS quantum-well-quantum-dot. The values are relative to the conduction band minimum of HgS. The unit is eV. E is for even states and O is for odd states.

j	$\frac{3}{2}$, E	$\frac{3}{2}$, O	$\frac{5}{2}$, E	$\frac{5}{2}$, O
1	0.082	0.187	0.135	0.320
2	1.074	1.322	1.076	1.434
3	1.989	2.190	1.455	1.923
4	2.562	2.953	2.077	3.350
5	3.515	3.850	2.890	4.208
6	4.317	4.860	3.740	5.395
7	5.499	5.910	4.816	6.291

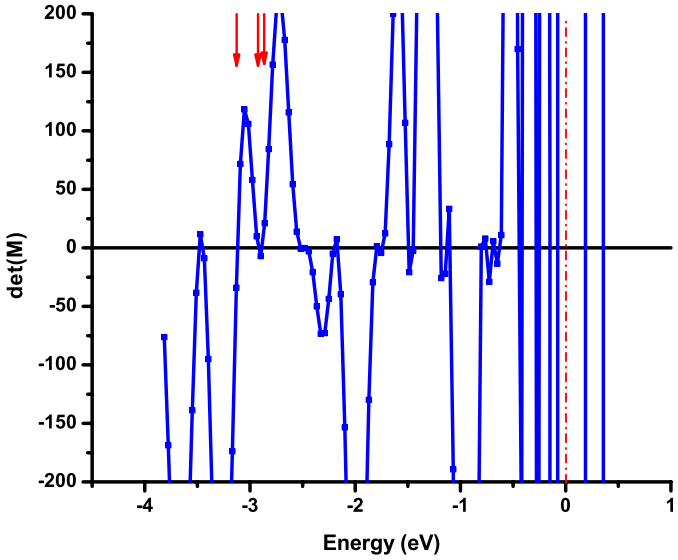

Figure 11: The determinant of the matrix which is used to determine the eigenenergies of sates with even parity and total angular momentum j=$\frac{3}{2}$. Energies at which the determinant is zero correspond to the eigenenergies. The energy reference point is the valence band maximum of CdS. The envelope functions which have the eigenenergies marked with arrows are plotted in Fig. 12 and Fig. 13.

bessel functions than those of the conduction band. Figure 11 show the determinant as a function of the energy for even sates with j=$\frac{3}{2}$. The values at which the determinant is zero correspond to eigenenergies of quantized electron states. Figure 11 shows that the states in the valence bands have smaller energy spacing that those in the conduction bands. The envelope functions for the states with eigenenergies marked with red arrows are plotted in Fig. 12 and Fig. 13.

The interesting thing about Fig. 13 is that two sates have close eigenenergies (-2.926 eV and -2.882 eV) but their envelope functions have big difference. The envelope functions in (a) have large magnitudes in the surface CdS layer. The magnitudes are so large that they are beyond the y range shown there. On the other hand, the envelope functions in (b) have large magnitudes only in the core CdS layer.

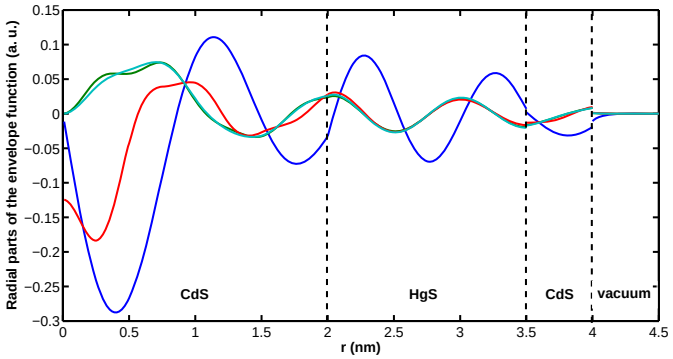

Figure 12: The wavefunction for an eigenstate with even parity and total angular momentum of $j=\frac{3}{2}$. The eigenenergy of this state is -3.118 eV. The connection of wavefunctions at the interface between the surface layer and the vacuum is not continuous. This is due to the numerical error resulting from exponentially increasing spherical bessel functions. The nanocrystal has three layers.

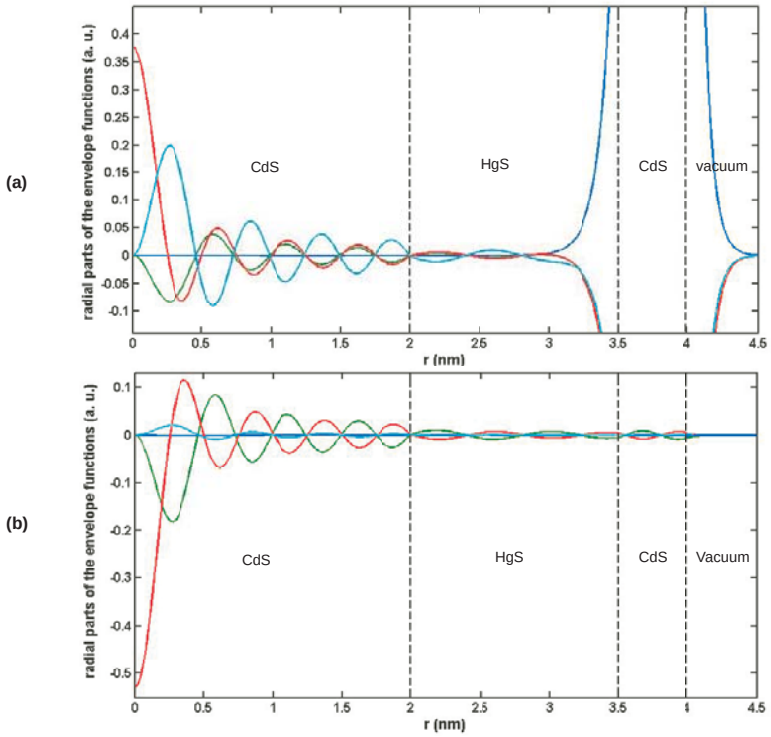

Figure 13: Envelope functions of two eigenstates with even parity and total angular momentum of $j=\frac{3}{2}$. (a) The eigenenergy is -2.926 eV. The plot doesn't show the whole envelope functions. The magnitudes of the envelop functions inside the surface CdS layer are so large that they are beyond the y axis range shown here. (b) The eigenenergy is -2.882 eV. Two states have close eigenenergies. But the wavefunctions have big difference.

CHAPTER III

SIMULATION OF TUNNELING CURRENT VOLTAGE CURVES

3.1 Introduction

Since the early 90s, tunneling spectroscopy has been used to measure electronic proprieties of semiconductor quantum dots, ultra-small metal particles, semiconductor nanocrystals, and metal nanocrystals. A typical spectroscopic experimental configuration is shown in Fig. 14. Left and right are two electrodes connected to outside circuits. There are dielectric spacers between the two electrodes and the nano-particle. Depending on the details of the experiment, one of the electrodes could be a STM tip. The dielectric spacer could be vacuum or insulating material. Electrons cross insulating gaps via quantum-mechanical tunneling. In order to get appreciable tunneling current, the gaps are very small, usually a few nanometers or less. The tunneling rates are very small. When one electron tunnels onto the nano particle, it will stays there for a while. When the electron is on the nano particle, it experiences all kinds of scattering. Its phase will be destroyed before it tunnels out of the nano particle. Therefore, the tunneling in and tunneling out are two unrelated events. This kind tunneling process is called sequential tunneling.

In tunneling experiments, one of the electrodes will be biased at a finite voltage relative to the other electrode. Two gaps between the electrodes and the nano particle form two junctions with capacitances C_1 and C_2. As shown in Fig. 14, the total bias voltage V_t is divided into V_1 and V_2. V_1 (V_2) is the voltage drop across the left (right) junction. If there is a charge Q on the nano particle, the two junctions store extra energy E_c:

$$E_c = \frac{1}{2}\frac{Q^2}{C_1 + C_2} \tag{43}$$

When one electron tunnels onto or out of the nano particle, the total charge Q will change. The change of Q changes the charging energy E_c.

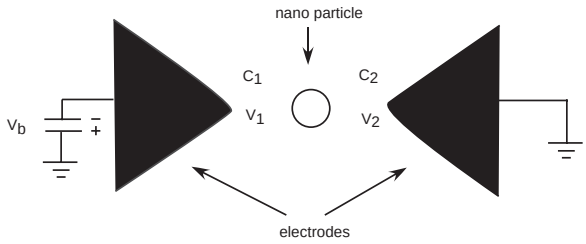

Figure 14: A typical setup for tunneling spectroscopy experiment. Two electrodes are coupled to the middle nano particle through electron tunneling. The spaces between electrodes and nano particle are insulating material or just vacuum. The thickness of spaces is small enough to have appreciable tunneling current. Spaces form junctions with capacitances C_1 and C_2. V_t is the bias voltage of the left electrode. V_1 is the voltage drop across the left junction. V_2 is the voltage drop across the right junction.

Now we consider the details of energy transfer while tunneling. Assume the left electrode in Fig. 14 is biased negatively and the right electrode is grounded. The external bias raises the energy levels of the electrons in both the nano particle and the left electrode. If one electron moves across the junction 1 (or 2) from left to right, it gains energy eV_1 (or eV_2) from the external circuit. But at the same time, it will lose some energy to compensate the change of the charging energy E_c. If the gain of energy from external bias circuit is less than the cost of compensation, then the tunneling event will not occur. Therefore the tunneling current is zero at this particular bias. Only when the bias voltage is large enough to provide enough energy for electrons to overcome the changing of E_c, current begins to increase with bias voltage. The charging energy E_c increases quadratically with charge. If the bias voltage is just high enough to charge the nano particle to Q and there is Q already on nano particles, it is not possible for one more electron to tunnel onto nano particle because charging energy of $Q - e$ is too big. Only after one electron leaves the nano particle, another electron can tunnel onto nano particle. When $Q = 0$ this phenomenon is called Coulomb blockade. A typical current voltage curve is shown in Fig. 15 [60]. The current curves have steps. These steps are related to nano particle's states with different charge. When bias voltage keeps increasing, it becomes possible to have multiple extra electrons or holes on the nano particles. The current usually is proportional to the extra charge on the nano particle. Therefore the current curve is like a staircase. This current

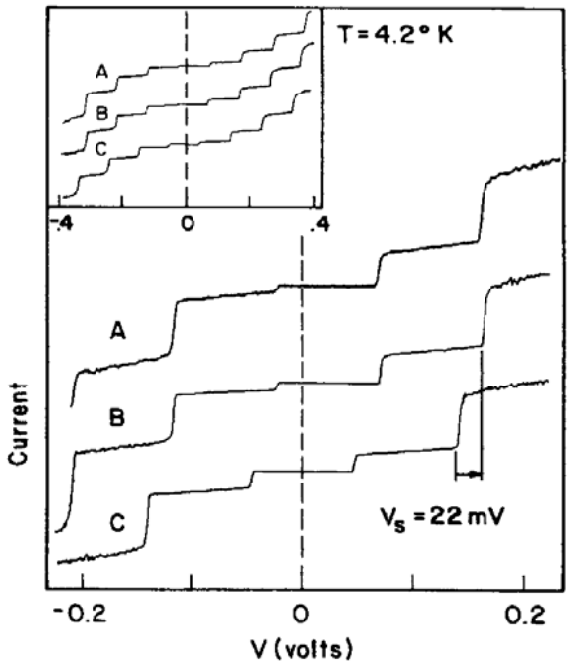

Figure 15: Tunneling current-voltage curves for an Indium droplet of 30 nm. Curve A is the measured I-V curve. Curve B and C are curves fit to Curve A with capacitances $3.5 \times 10^{-19}F$ and $1.8 \times 10^{-18}F$ for two junctions. Inset shows I-V on larger scale. [60].

shape is called Coulomb staircase. These steps have same width in voltage.

The fit curves in Fig. 15 are calculated with the double-junction model and "orthodox theory" [14, 34]. The equivalent circuit is shown in Fig. 16. The voltages drops in two junctions are described by two capacitances C_1 and C_2. The tunneling current is determined by two resistances R_1 and R_2. The currents across each junction are calculated simply by Ohm's law.

$$I_i = \frac{V_i}{R_i}, \quad i = 1, 2 \tag{44}$$

$R_{1,2}$ can be calculated by Golden rule [30].

$$R_i = \frac{\hbar}{2\pi e^2 |T_i|^2 D_a D_b}, \quad i = 1, 2 \tag{45}$$

T_i is the tunneling matrix element. D_a and D_b are the electron density of states of the electrodes involved in tunneling and nano particle.

The main points of the orthodox theory of tunneling are: (1) The energy levels in electrodes and nano particles are continuous. (2) The tunneling probability for all sates are

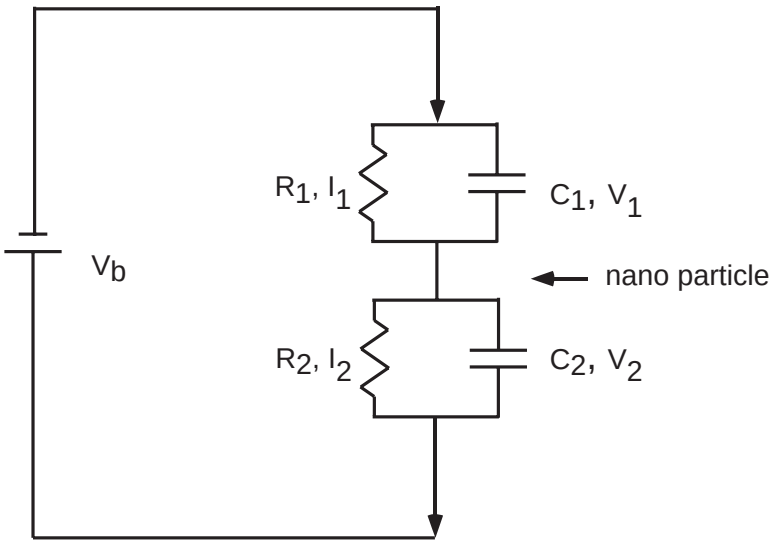

Figure 16: The double-junction model for tunneling spectroscopy of nano particles. C_1 and C_2 are capacitances of two junctions. R_1 and R_2 are corresponding resistances to calculate tunneling currents across two junctions. The tunneling current and voltage drop of each junction is simply related by the Ohmic law using the resistance of that junction.

assumed to be the same in the range of voltages applied. (3) Charging energy is significant and larger than k_bT. (4) Charges on the nano particles are discrete except some residual charge. (5) The transitions between different charge states are described by rate equations. This theory works well for large nano particles at high temperature. The corresponding dI/dV vs voltage curves of the I-V curves in Fig. 15 are formed by even spaced peaks. Each peak corresponds to a change of electron number. We call these peaks charging peaks.

The above current-voltage curves emphasize the effect of discrete charges on tunneling current. They don't contain any information about the individual electron levels inside nano particles. Such measurements are usually done on relatively large metal nano particles. In order to resolve discrete electron levels in metal nano particles, the size of particles should be very small. For example, the energy spacing for an Aluminum nano particle with diameter of 2 nm is about 2.5 meV. The temperature should be lower than 10 K in order to resolve the individual energy levels [51].

Since the mid-1990's, Al and Au nano particles down to 1.5 nm radius can be made by advanced microelectronics fabrication techniques [12, 28, 51]. In these experiments, the

effect of a single electron level on the tunneling current is observed at low temperature. Figure 17 shows two dI/dV curves for Al nano particles at 30 mK. Here all peaks are below the second Coulomb charging peak. Therefore these peaks should correspond to discrete energy levels inside Al nano particles. One interesting thing is that dI/dV peaks have cluster type structures. Except for the first peak, peaks are grouped into several clusters. The voltage distance between neighboring cluster centers is of the same order of the energy spacing of Al nano particles under investigation. Each cluster is thought to correspond to one electron level. But the exact energy of this level depends on the detail of occupations of other energy levels. Figure 18 is used to illustrate this argument. In (a). The bias voltage is small. Fermi level of the left electrode is lower than the first unfilled level i of the nano particle. In (b), the Fermi level is aligned with level i. Now electrons can tunnel onto level i. Once level i is filled with one electron, all energy levels of the nano particle are shifted upward. Electrons on level i or several levels below i can tunnel out to the right electrode. If the voltage increase further, Fermi level will be aligned with level i+1. Depending on how electrons occupy levels below level i+1 (Four different states are shown in (c)) , the actual energy of this level i+1 can vary. This explains why there are five peaks around the second energy level in Fig. 17(a). This theory emphasizes the effect of electron-electron interaction on individual energy levels. It also realizes that while in tunneling, many states maybe are involved and many of then are excited states. This theory is further improved by Narvaez et al [47]. They use the concept of "generation" to count all excited states with same charge. The "state" of a nano particle is described by the total charge and the detail distribution of electrons on the energy levels. Narvaez et al. used mean-field theory to calculate the fluctuation of energy levels due to different excited states.

Tunneling spectroscopy of colloidal synthesized gold nanocrystals has also been measured. Figure 19 shows the dI/dV vs voltage curve of a gold nanocrystal [20]. This spectrum is different from dI/dV curves predicted by orthodox theory. This indicates that some peaks are related to discrete electron energy levels.

In the next section, we will develop a model to simulate current vs voltage for nanocrystals. Particular attention is given to the effect of excited states on I-V or dI/dV curves.

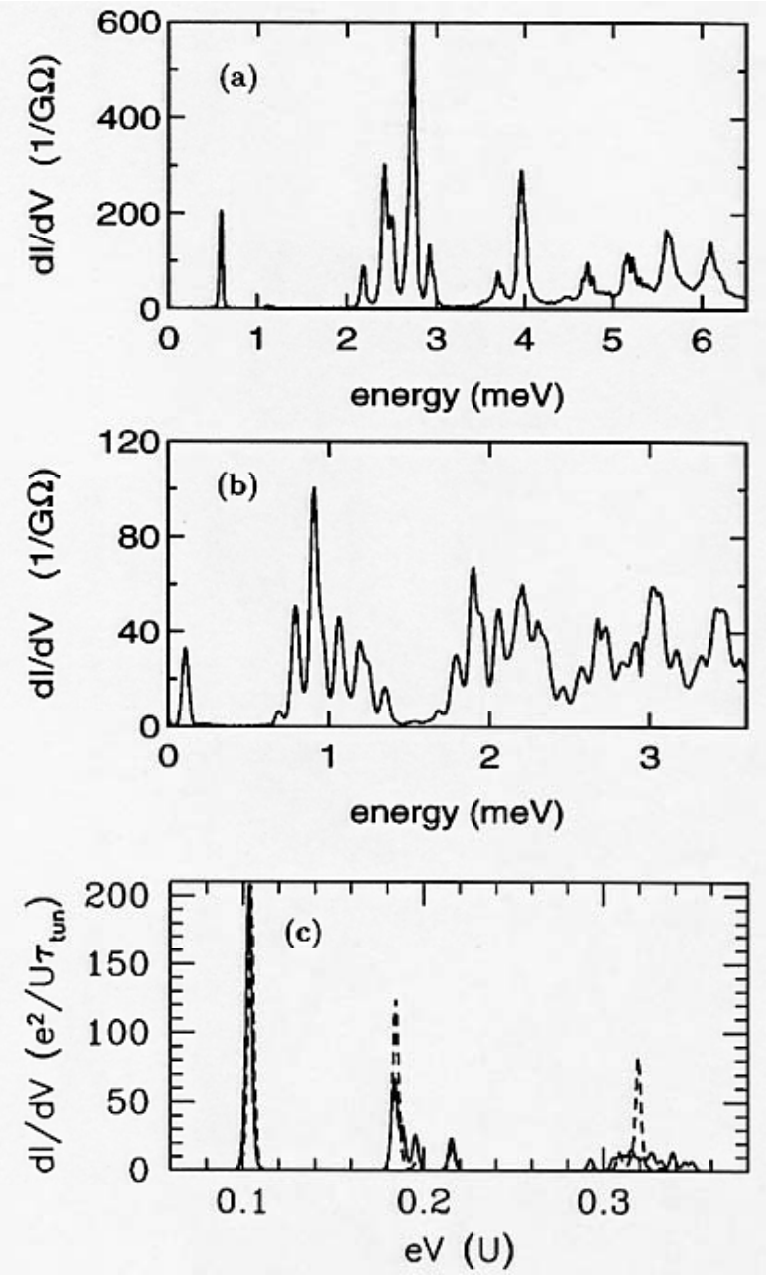

Figure 17: dI/dV vs bias voltage for Al nano particles with volumes (a)$40nm^3$ and (b)$100nm^3$ at 30 mK [12].

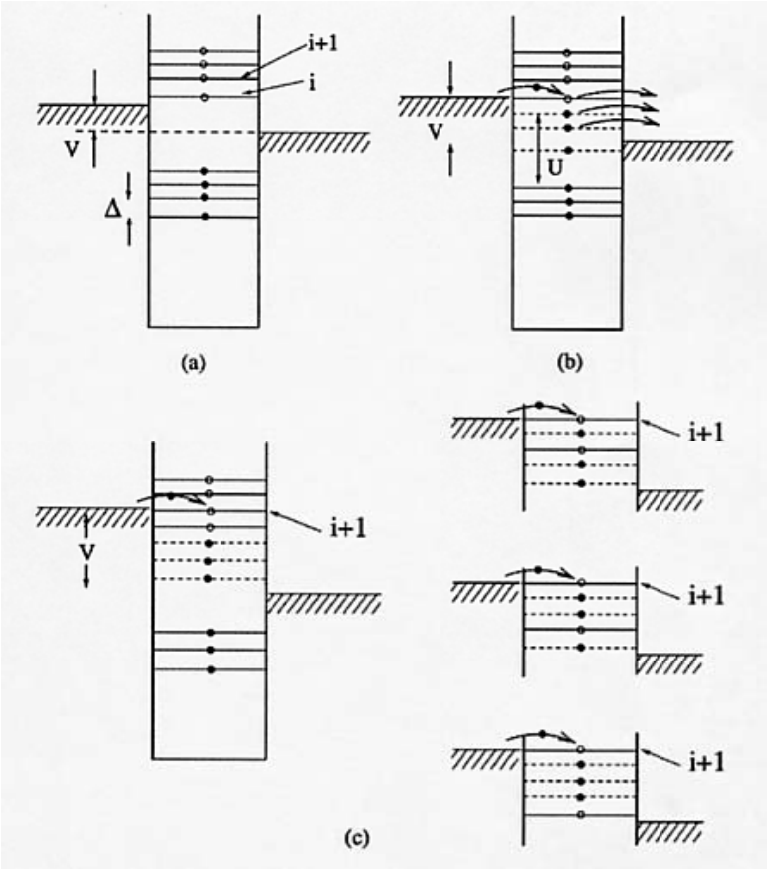

Figure 18: An illustration of electron transport through the metal particle at various values of the source-drain voltage V. Filled single particle levels are indicated by full circles and empty ones by open circles. U is the charging energy, and D is the single-particle mean level spacing. (a) The system at small bias voltage within the Coulomb blockade regime. (b) V corresponding to the first resonance in Fig. 17(a) and (b). The thin dashed lines indicate the energy of a level after an electron has tunneled into the dot. (c) V near the first cluster of resonances in Fig. 17(a) and (b). The splitting within the first cluster originates from the sensitivity of level i+1 to the different possible occupation states as shown [12].

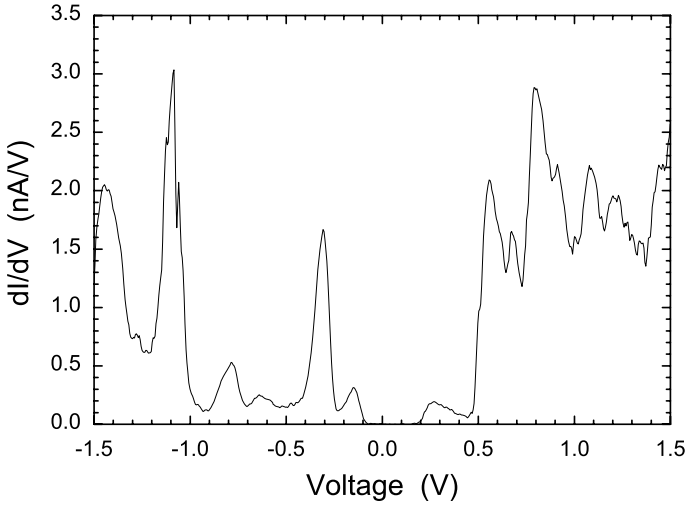

Figure 19: dI/dV vs voltage curve of a gold nanocrystal at 4 K. The set current for imaging is 100 pA and the tip bias voltage is -1 V [20].

Since all dI/dV curves we have were measured at room temperature, 77 K, and 4 K, the modification to energy levels due to electron-electron interaction is not considered. Our interests is the kinetic processes of tunneling. We want to investigate how many states are involved in the tunneling at a particular bias and what probability each of these states has. Another thing we want to investigate is how the relaxation would affect the dI/dV spectrum. Parameters like capacitances $C_{1,2}$ and residual charge Q_0 will be changed to see how they change the shape of curves. In the next chapter, BEEM current vs voltage curves will be modeled. The model developed here will be used in that chapter. The ultimate goal of these simulation is to understand how parameters affect the overall shape of I-V curves and how to extract physical information from measured spectra.

3.2 The Model

The gold nanocrystals we investigate are 1$\sim$ nm in diameter. The energy spacing between neighboring quantized energy levels is about tens of meV. Not like semiconductor nanocrystals which have big energy gap between the highest occupied energy level and lowest unoccupied energy level, the gold nanocrystals we investigate only have energy gaps of

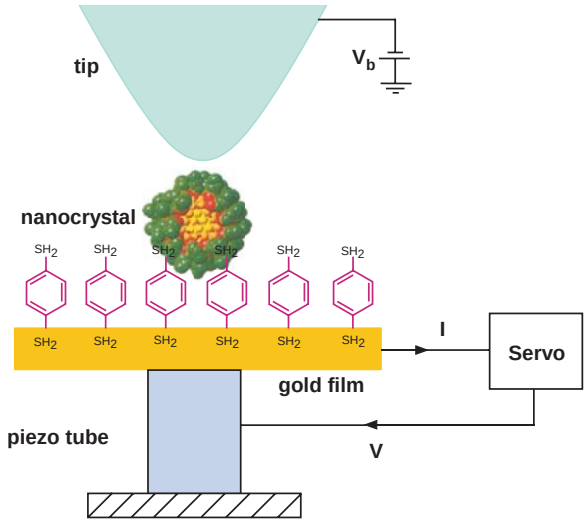

Figure 20: Basic setup of STM/STS experiments on nanocrystals. Nanocrystals with capping molecules are attached to the surface by the self-assembled monolayer(SAM) of xylenedithiol molecules. The space between tip and nanocrystal forms one junction. The SAM layer forms another junction. The bias voltage is applied to the tip. Tunneling current is detected from the substrate.

tens of meV between occupied and unoccupied levels. Therefore not only the unoccupied levels but also the occupied energy levels would be involved in the tunneling process. The work function of gold is about 5 eV, the tunneling rates for energy levels around Fermi level inside nanocrystals should be of same magnitude. We expect there would be a lot of excited states.

Figure 20 illustrates the basic setup of the STM experiment. The bias voltage is applied to the tip while the substrate is grounded by being connected to the input of a current-voltage amplifier. The space between tip and nanocrystal forms the first junction with capacitance C_1. The space between nanocrystal and the gold substrate forms the second junction with capacitance C_2. The total bias voltage is split between two junctions. The change of electrostatic potential of nanocrystal relative to the substrate will shift energy levels of electrons on the nanocrystal. The corresponding equivalent circuit is shown in Fig. 21. When the tip is biased at $-V_t$ relative to the ground (substrate), the potential difference between the nanocrystal and the tip is V_1. The difference between the substrate and the nanocrystal is V_2. $-ne + Q_0$ is the total charge on the nanocrystal. Since we will

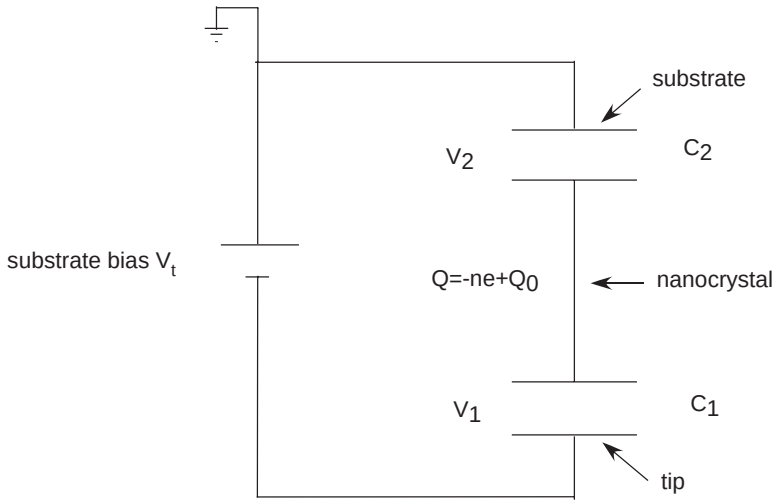

Figure 21: The equivalent circuit of the STM experiments. Here the tip is biased at a negative voltage $-V_t$ ($V_t > 0$). The potential difference between the nanocrystal and the tip is V_1. The difference between the substrate and the nanocrystal is V_2. $-ne$ is the discrete charge builded up due to electron tunneling. Q_0 is the residual charge on the nanocrystal. Its origin can be polarization. The total charge is $-ne + Q_0$.

treat tunneling related to discrete energy levels, the resistances R_1 and R_2 in Fig. 16 are not used here. V_1 and V_2 are:

$$V_1 = \frac{C_2}{C_1 + C_2} V_t + \frac{-ne + Q_0}{C_1 + C_2} \tag{46}$$

$$V_2 = \frac{C_1}{C_1 + C_2} V_t - \frac{-ne + Q_0}{C_1 + C_2} \tag{47}$$

When one electron moves across one junction in the direction from tip to the substrate, the electron extracts some energy $\Delta E_{1(2)}$ from the external bias circuit. This part has no relation to the charging energy built up inside two junctions.

$$\Delta E_{1(2)} = e \frac{C_{2(1)} V_t}{C_1 + C_2} \tag{48}$$

At the same time, when electrons tunnel onto or off of nanocrystals, the change of charging energy due to adding one electron from the tip to the nanocrystal is:

$$\Delta E_c(n \to n+1) = \frac{1}{2} \frac{[-(n+1)e + Q_0]^2}{C_1 + C_2} - \frac{1}{2} \frac{(-ne + Q_0)^2}{C_1 + C_2} \tag{49}$$

The change of charging energy due to extracting one electron from the nanocrystal to the substrate is:

$$\Delta E_c(n \to n-1) = \frac{1}{2} \frac{[-(n-1)e + Q_0]^2}{C_1 + C_2} - \frac{1}{2} \frac{(-ne + Q_0)^2}{C_1 + C_2} \tag{50}$$

If $\Delta E_c(n \rightarrow n+1)$ is positive and much larger than $eC_2V_t/(C_1+C_2)$, then the electron will not tunnel from the tip to the nanocrystal. This is just the Coulomb blockade phenomenon mentioned before. When $-ne+Q_0$ is positive, $\Delta E_c(n \rightarrow n-1)$ is positive, this will make electron tunneling out of the nanocrystal to the substrate difficult.

Figure 22 shows energy levels for several possible charging states of a nanocrystal. In Fig. 22(a), there is no net charge on the nanocrystals. States (b) and (d) have one extra electron on the nanocrystal. State (c) is neutral and has a hole below the Fermi level. State (e) has two extra two electrons. One thing that should be emphasized is that state (e) can be achieved from state (a) via state (b), (c), and (d). But at the tip bias voltage we show there, state (e) can't be achieved from state (a) by just injecting two electrons consecutively onto the nanocrystal. State (e) is achieved only via a specific path of tunneling events. The existence of path dependent states like (e) at lower bias voltage is not predictable. This makes listing all states accessible at a bias voltage very difficult. The key point here is that when one electron tunnels from the tip to the nanocrystal, it could fill a deep hole like the hole in state (d). Some lattice energy of the electron is transferred to charging energy. Therefore multiple charging is possible at low bias. We call this self-pumping of the nanocrystal.

In order to overcome the state listing problem mentioned above, a similar strategy as in [47] is used to find all states which will be involved in the tunneling process at a particular tip bias. We start with the ground state at the left in Fig. 23. This state is the state before any tunneling events. Electrons fill discrete energy levels till the Fermi level. We assign this state to the g0 group. The g0 group only has this state. The next group is the g1 group. States in the g1 are formed from the states in the g0 (only one as we said) by adding one electron to or extracting one electron from the nanocrystal. The states formed by adding one electron to different levels of the same state are thought to be different. Since the state in g0 group has no extra electron or hole, the states in g1 are in two categories. One has states which have one extra electron but no holes. the other has states which have one hole but no electrons above the initial Fermi levels. From each states in g1, adding one electron or extracting one electron can form new states which are assigned to group g2. So on we

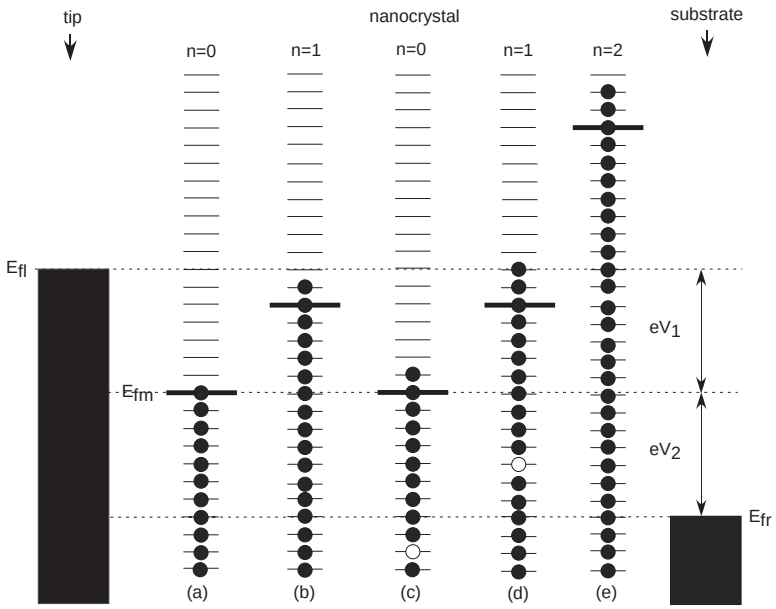

Figure 22: Sequential tunneling of electrons across two junctions.(a) is the initial state of the nanocrystal. (b) the state has extra electron compared with (a). (c) One electron tunnels out from one filled level and leaves a hole in the nanocrystal. (d) One electron tunnels onto nanocrystal with state in (c). (e) One electron tunnels onto the nanocrystal and fills the hole in (d). The nanocrystal now has two extra electrons.

can have states for g3, g4, ..., etc. Adding or extracting electrons from a particular energy level of a particular state is restricted by the tip bias. Only energy conserving tunneling processes are permitted. Figure 23 shows the state in g0 and four representative states in the g1 group.

The changing of the charging energy ΔE_c modifies the potential barrier experienced by an electron in the tunneling process. This is shown in Fig. 24. In Fig. 24, the energy levels of the nanocrystal is fixed. Therefore the electrostatic potential and the Fermi levels of the tip and the substrate are shifted when charging energy ΔE_C is not zero. Different color lines correspond to different tunneling processes and different changing of charging energy.

The energy of electron levels in the tip, the substrate, or the nanocrystal is the sum of electron's kinetic energy and the lattice potential energy. The external electrostatic potential energy is not included in that sum. The electron energy levels are referred to the Fermi levels of the tip, the nanocrystal, or the substrate. In the following, three Fermi levels are assumed to be same when no external bias and extra charge (except the residual

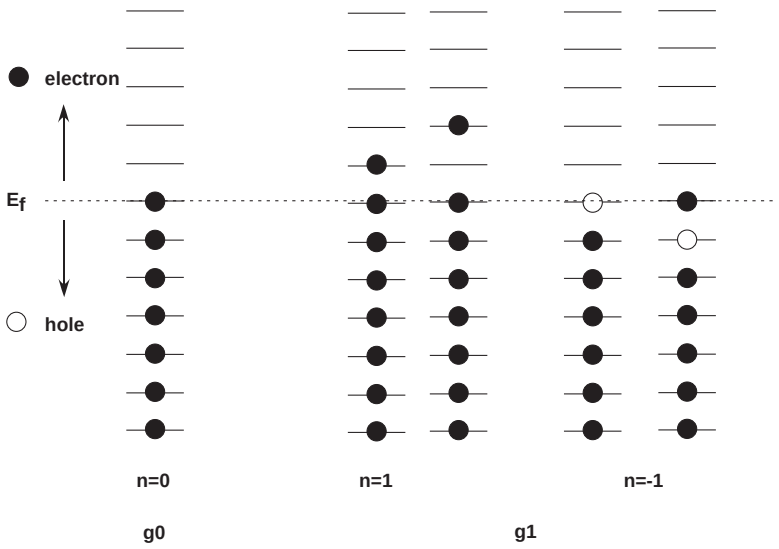

Figure 23: Generations of states. The left state is the initial state called the ground state. Electrons fill energy levels up to Fermi level. All levels above Fermi level is empty and all levels below Fermi level are filled. The level aligned with Fermi level is also filled. If energy levels below Fermi level loses one electron, then we call one hole is created on that level. The ground state is the only state in group g0. The right four states are created by adding one electron onto or extracting one electron from the nanocrystal. They are in the group g1. The number in g1 is restricted by energy consideration. If the bias is high, more state can be in g1.

charge). While tunneling, the total energy of the electron is conserved. Now consider an electron tunneling from the tip to the nanocrystal while the net charge on the nanocrystal changes from $-ne+Q_0$ to $-(n+1)e+Q_0$. The total energy conservation has the following equation.

$$\frac{C_2}{C_1+C_2}eV_t = E_n - E_t + \frac{1}{2}\frac{[-(n+1)e+Q_0]^2}{C_1+C_2} - \frac{1}{2}\frac{[-ne+Q_0]^2}{C_1+C_2} \tag{51}$$

Where E_t is the energy of the involved electron level in the tip and E_n is the energy of the involved electron level in the nanocrystal.

In order to find out when tunneling one electron from the tip to a particular energy level E_n in nanocrystal is possible, the above equation is re-written as:

$$-E_t = \frac{C_2}{C_1+C_2}eV_t - E_n - \Delta E_c(n \to n+1) \tag{52}$$

Where

$$\Delta E_c(n \to n+1) = \frac{1}{2}\frac{[-(n+1)e+Q_0]^2}{C_1+C_2} - \frac{1}{2}\frac{[-ne+Q_0]^2}{C_1+C_2} \tag{53}$$

At absolute zero temperature, the condition for tunneling electron onto level E_n on nanocrystal is $E_t \leq 0$ because of the Fermi-Dirac distribution. Therefore the condition for adding one more electron onto energy level E_n of the nanocrystal at 0 K is

$$\frac{C_2}{C_1+C_2}eV_t \geq E_n + \Delta E_c(n \to n+1) \tag{54}$$

Similarly, the condition of extracting one electron from the nanocrystal to the substrate at 0 K is:

$$\frac{C_1}{C_1+C_2}eV_t \geq -E_n + \Delta E_c(n \to n-1) \tag{55}$$

Where E_n is the energy of the electron level on the nanocrystal occupied by the electron before it tunnels out.

The tunnel rates across two junctions are calculated using Simmon's planar tunneling approach [54].

$$T(E) = \exp\left[-\frac{4\pi}{h}(2m)^{\frac{1}{2}}\int_{s_1}^{s_2}(\phi(x)-E)^{\frac{1}{2}}dx\right] \tag{56}$$

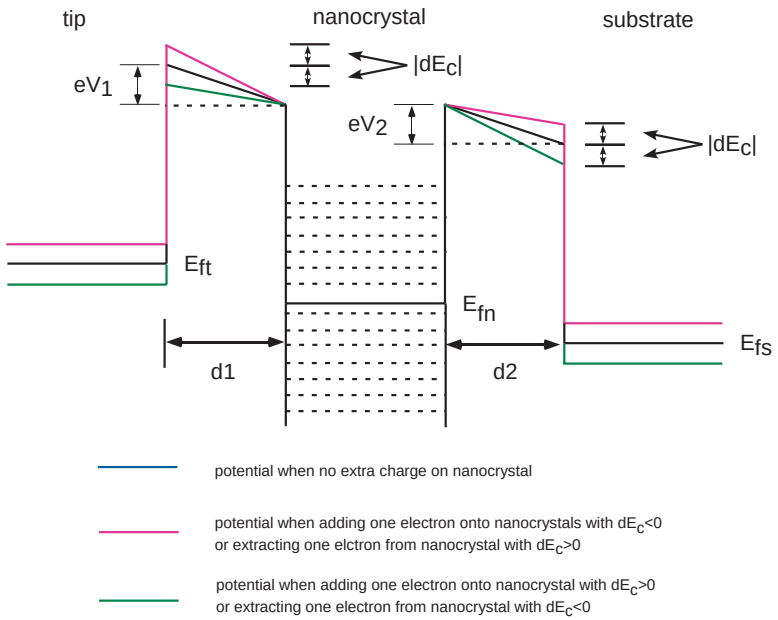

Figure 24: Energy diagram of the system. For simplicity, the energy levels of the nanocrystal are fixed. When the tip is biased at negative voltage $-V_t$, the energy levels in the tip shift upward and the energy levels in the substrate shift downward.

where $\phi(x)$ is the potential function and E is the energy of the tunneling electron. In our case, $\phi(x)$ is the vacuum level which is affected by the external bias circuit and charge on the nanocrystal. For simplicity, we assume the function $\phi(x)$ is a linear function by neglecting effects like the imaging potential. The value of $\phi(x)$ is measured from the Fermi level of the nanocrystal.

Figure 24 shows the profile of the potential. If the charging energy is neglected, Then the potential curves for electrons are the black lines. The slopes are determined by eV_1 (eV_2) and the gap distance d_1 (d_2). The energy difference between the Fermi level and the vacuum level is fixed at the surface of the nanocrystal. If there is no electric field, the potential profile is flat between the surface of the nanocrystal and the surface of the tip or substrate. The electric field from external bias circuit and extra charge on the nanocrystal will tilt the potential profile. The total tilt is the electrostatic potential difference between two sides of the junction. So if the difference of electrostatic potential at both sides of the junction, the work function of the nanocrystal, and the width of the junction are known, the potential function can be found by linear fitting.

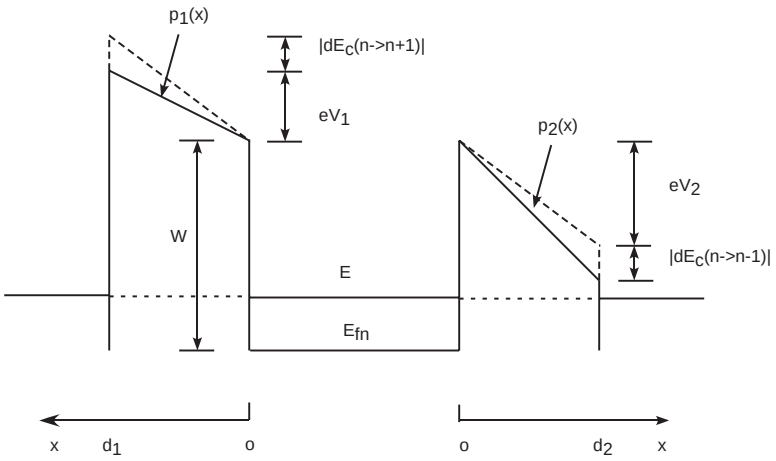

Figure 25: Potential barrier for tunneling electrons.

When one electron tunnels from the tip to the nanocrystal, it feels two electrostatic forces. One is the force originating from the external circuit. This force tilts the vacuum level by eV_1. The second is from the interaction between the tunneling electron and charges already on the nanocrystal. The change of the charging energy is equal to the work done on the tunneling electron by the charge on the nanocrystal. This required work forms part of the energy barrier experienced by the tunneling electron. Therefore, the second part of the tilting of vacuum level originating from charging is ΔE_c. Figure (24) shows the potential profile for various kinds of tunneling processes.

In Fig. 25 we show the energy barriers $p1(x)$ and $p2(x)$ for tunneling electrons. The origins of x for $p1(x)$ and $p2(x)$ are at the surface of the nanocrystal. When adding one electron from the tip to the nanocrystal, the energy barrier is

$$p_1(x) = W + \frac{eV_1 - \Delta E_c(n \to n+1)}{d_2} x, \;\; 0 < x < d_1 \tag{57}$$

Here W is the work function of the gold which is measured from the Fermi level to the vacuum level. Similarly, the potential barrier experienced by the electron when it tunnels out of the nanocrystal to the substrate is

$$p_2(x) = W - \frac{eV_2 - \Delta E_c(n \to n-1)}{d_2} x, \;\; 0 < x < d_2 \tag{58}$$

By inserting above function $p_1(x)$ and $p_2(x)$ into Equation (56), we get the tunneling

rates:

$$T_{1,2}(E) = \exp\left[-\frac{4\pi}{h}(2m)^{\frac{1}{2}}\int_0^{d_{1,2}}(p_{1,2}(x)-E)^{\frac{1}{2}}dx\right] \tag{59}$$

Each tunneling event changes the state of the nanocrystal. The transition rates related to tunneling can be calculated from tunneling rates in Eq. 59. The probability $P_i(t)$ of finding the nanocrystal in state i is determined by the following equations

$$\frac{d}{dt}\begin{pmatrix} P_1(t) \\ P_2(t) \\ .. \\ P_n(t) \end{pmatrix} = \begin{pmatrix} \Gamma_{11} & \Gamma_{12} & .. & \Gamma_{1n} \\ \Gamma_{21} & \Gamma_{22} & .. & \Gamma_{2n} \\ .. & .. & .. & .. \\ \Gamma_{n1} & \Gamma_{n2} & .. & \Gamma_{nn} \end{pmatrix} \cdot \begin{pmatrix} P_1(t) \\ P_2(t) \\ .. \\ P_n(t) \end{pmatrix} \tag{60}$$

Γ_{ij} is the rate at which the nanocrystal changes from state j to i. For example, one electron changes the state of the nanocrystal from j to i by tunneling from the tip to the α energy level of the nanocrystal. The corresponding Γ_{ij} is

$$\Gamma_{ij} = f_t(E_\alpha)T_1(E_\alpha), i \neq j \tag{61}$$

Here $f_t(E)$ is the Fermi function of the tip. If the change of state from j to i is caused by extracting one electron from the energy level E_α, then the Γ_{ij} is

$$\Gamma_{ij} = (1 - f_s(E_\alpha))T_2(E_\alpha), i \neq j \tag{62}$$

$f_r(E)$ is the Fermi function of the substrate. Their forms should take into account the energy shift because of the external bias voltage and the charging energy.

Another form of Γ_{ij} is related to relaxation. If one electron relaxes from energy level β to α to change the state from j to i, then Γ_{ij} is

$$\Gamma_{ij} = R_{\alpha\beta}, \;\; i \neq j \tag{63}$$

Here $R_{\alpha\beta}$ is the relaxation rate at which electron relaxes from energy level β to α.

Γ_{ii} is the rate at which the nanocrystal changes from state i to all other possible states j by adding one electron, extracting one electron, or relaxing one electron inside the nanocrystal. Γ_{ji} is the rate at which the nanocrystal changes from the sate i to the state j. Therefore

Γ_{ii} is calculated as:

$$\Gamma_{ii} = -\sum_{j \neq i} \Gamma_{ji} \tag{64}$$

At static state, all $P_i(t)$ are assumed to be constant. Therefore these constant P_i have the following equations.

$$\begin{pmatrix} \Gamma_{11} & \Gamma_{12} & .. & \Gamma_{1n} \\ \Gamma_{21} & \Gamma_{22} & .. & \Gamma_{2n} \\ .. & .. & .. & .. \\ \Gamma_{n1} & \Gamma_{n2} & .. & \Gamma_{nn} \end{pmatrix} \cdot \begin{pmatrix} P_1 \\ P_2 \\ .. \\ P_n \end{pmatrix} = \begin{pmatrix} 0 \\ 0 \\ .. \\ 0 \end{pmatrix} \tag{65}$$

Once all P_i are found, the current is calculated by transition rates from all possible states and energy levels of each state which can contribute to the current.

$$I = \sum_{\{i\}} P_i \sum_{\{\alpha\}} T_2(i, \alpha)(1 - f_r(E_\alpha)) \tag{66}$$

The braces for i and α mean that not all states and energy levels can contribute to current. Here the current is calculated by summing rates of electrons tunneling out from the nanocrystal to the substrate. A particular tunneling process can contribute to the current only if it satisfies Eq. 55.

3.3 Simulations

The simulation starts with the setup of the system by specifying the the energy levels of the nanocrystal(E_i), work functions (W_t, W_n, W_s for the tip, the nanocrystal, and the substrate respectively), distances of two junctions (d_1 and d_2), capacitances of two junctions (C_1 and C_2), and the residual charge (Q_0). Then a voltage is biased between the tip and the substrate. Assume that the tip is negatively biased at $-V_t$ relative to the substrate which is grounded. The next step is to find out states which are accessible at this particular bias voltage. The concept of generation introduced above is used to find states. g0 group has only one state. It is the ground state which has no net extra electron or hole. Then one electron attempts to tunnel onto various empty energy levels on the nanocrystal. This tunneling process is restricted by the Eq. 54. If this process is allowed, then the resulting state is assigned to g1 group. The attempt to attract one electron from various filled levels

of the ground state is also made. For this the restriction is Eq. 55. The resulting states are also assigned to g1 group. After all states which should be in g1 are found, all kind of attempts of adding one electron to or extracting one electron from all g1 states are made subject to the restriction of Eq. 54 and Eq. 55. All resulting states except those already in g0 and g1 are assigned to g2 group. If this generation process continues, all states which are accessible can be found. But usually we stop after several generations. This is because of our capability of computation. We believe that the probability of the high generation states are small. The argument is that the high generation states are accessed only through particular combination of tunneling events. This greatly reduces the probability of these high generation states. In the following, we only take states in g0, g1, g2, g3, and g4 into account. states in g4 can have two electron-hole pairs. Once we have all the states, then we build the matrix Γ in Eq. 60. Only those elements of Γ whose corresponding tunneling or relaxation process are allowed are not zero. For nonzero elements, the values are calculated according Eq. 61, Eq. 62, or Eq. 63. Then Eq. 65 is solved to find out all the probabilities. Finally the current is calculated using Eq. 66.

3.3.1 Simulation A

All parameters for the first simulation are listed in Table 3. All the energy levels are assumed to be even spaced. The energy spacing is 0.1 ev. C_1 and C_2 are chosen to let $\frac{1}{2}\frac{e^2}{C_1+C_2}$ be 0.5 ev. The residual charge Q_0 is $0.2e$. All parameters are listed in Table 3. Figure 26 is the calculated I-V curve. The unit for current is arbitrary. The x axis is the bias of the substrate relative to the tip. Numerical derivative is done to this tunneling I-V and the result is shown in Fig. 27.

In Fig. 27, the first several peaks are even spaced although two of them are depressed. When the bias voltage is higher than 1.1 V, the dI/dV peaks becomes complicated. Some of them are split. Also the spacing between neighboring peaks becomes irregular.

In order to understand these peaks in Fig. 27, we calculate the necessary voltages for some tunneling events. First we consider the tunneling events which will change the net electron number on the nanocrystal from 0 to 1. The state before these tunneling events

Table 3: Parameters for simulation A. Subscript 1 is for the junction between the tip and the nanocrystal. Subscript 2 is for the junction between the nanocrystal and the substrate. All work functions are assumed to be same. Temperature is 77 K.

C_1	0.3 (e/V)
C_2	0.7 (e/V)
d_1	4.8 Å
d_2	4.0 Å
hole level spacing	0.1 eV
electron level spacing	0.1 eV
residual charge	0.2 e
work functions	6 eV
temperature	77 K

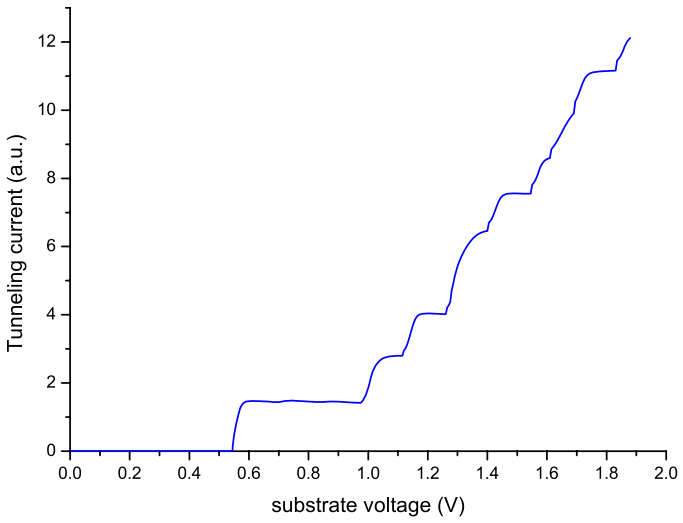

Figure 26: Calculated tunneling I-V curve for parameters listed in Table (3).

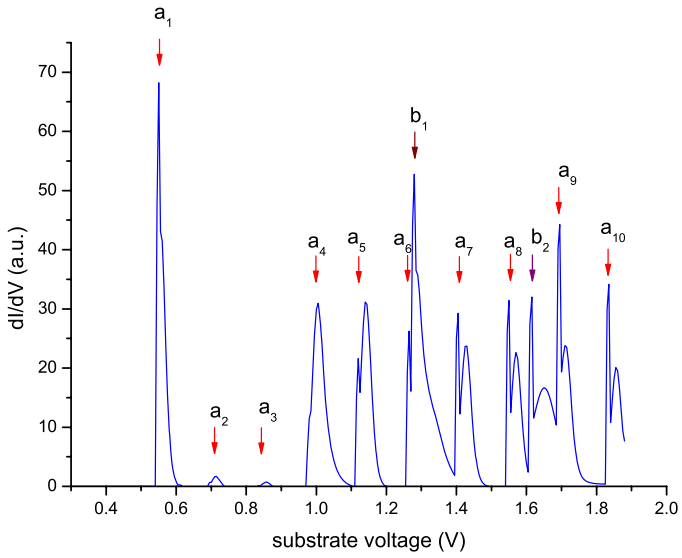

Figure 27: Numerical derivative of the current voltage curve in Fig. 26. Voltages at peaks marked by red arrows can be found in Table 4. Two voltages at peaks marked by brown arrows can be found in Table 5.

is the ground state shown in Fig. 22(a). Except the residual charge Q_0, There is no extra electron or hole on the nanocrystal. For one electron to tunneling on to the nanocrystal, it has to extract enough energy from the external bias circuit to overcome the charging energy it builds up once on the nanocrystal. The electron also needs some extra energy to compensate the energy difference between the level in tip and the level on the nanocrystal. Assume E_n is the energy of one empty level of the ground state. Then the voltage needed to tunnel one electron from the tip to the level E_n of the ground state is

$$\frac{C_2}{C_1+C_2}eV_t \geq E_n + \Delta E_c(n=0 \rightarrow n=1) - \frac{3}{2}kT \tag{67}$$

The last term $-\frac{3}{2}kT$ is an approximation. The purpose of it is to take into account the Fermi distribution at non-zero temperature. The minimum voltage for electrons tunneling out of the nanocrystal to the substrate is calculated according to Eq. 68.

$$\frac{C_1}{C_1+C_2}eV_t \geq -E_n + \Delta E_c(n=0 \rightarrow n=-1) - \frac{3}{2}kT \tag{68}$$

Table 4: Minimum bias voltage for directly adding one electron to empty electron levels of the ground state. Charge changes from Q_0 to $-e + Q_0$. Numbers in the left column refer to the first, second, ..., etc, empty levels of the ground state.

energy level	bias voltage (V)
1	0.5477
2	0.6906
3	0.8334
4	0.9763
5	1.1191
6	1.2620
7	1.4049
8	1.5477
9	1.6906
10	1.8334

Minimum voltages are calculated and listed in Table 4 and Table 5. In Table (4) and Table (5), 0 is the highest filled electron level (the Fermi level) of the ground state. -1 is the level just below the 0 level, and so on for -2 and -3. 1, 2, 3, .., are the empty levels of the ground state. 1 is the lowest empty level in the ground state.

For the system we specified above, the voltages in Table 4 and Table 5 are evenly spaced respectively. It is easy to see that these voltages are also related to other tunneling processes. For example voltages in Table 5 are related to tunneling processes which change the net electron number on nanocrystal from 1 to 2. But depends on the initial net electron number, the same voltage is related to different energy levels. If we make a table similar to Table 4 but for processes which change net electron number from n=1 to n=2, we can see there is a vertical shift of the voltages between these two tables. Similarly, voltages in Table 5 are related to processes which change net electron number from 2 to 1 or -1 to -2. For our system, there are two groups of voltages. One group is related to adding electron from the tip to the nanocrystal. The other is related to tunneling electron from the nanocrystal to the substrate.

Now we try to related peaks in Fig. 27 to voltages in Table 4 and Table 5. The 10 peaks marked with red arrows have one-to-one mapping to the voltages in Table 4. But other

Table 5: Minimum bias voltage for directly extracting one electron from filled energy levels of the ground state. Charge changes from Q_0 to $+e + Q_0$. Number 0 refers to the highest filled electron level (The Fermi level) of the ground state. Positive numbers refer to empty levels of the ground state and negative numbers refer to filled levels of the ground state.

energy level	bias voltage (V)
3	1.278
2	1.6113
1	1.9447
0	2.2780
-1	2.6113
-2	2.9447

peaks except the two peaks marked with brown arrows can't find corresponding voltages in Table 5.

We also calculate the current for electron tunneling from the substrate to the tip. In this case, the tip is positively biased relative to the substrate. The I-V and dI/dV-V curves for this bias is shown in the left side of Fig. 28. For comparison, the I-V and dI/dV-V curves in Fig. 27 and Fig. 26 are also plotted. Figure 28 is very interesting if one realize that in our model the tip and the substrate are the same. So the left side of Fig. 28 corresponds to a tip-to-substrate tunneling same as in Fig. 26 and Fig. 27 but with two junctions switched. These two tip-to-substrate tunneling cases have the same nanocrystal. But two spectra are different.

In STM/STS study of nanocrystals, the distance between the nanocrystal and the substrate is usually fixed. But the distance between the tip and the nanocrystal depends on the set current point. So depending on the distance and therefore the capacitance between tip and nanocrystal, the I-V or dI/dV-V curve can be quite different. This makes it difficult to extract accurate information about nanocrystal itself from spectroscopy data.

Now we go to the details of the above simulation. The first thing is the number of states involved in the tunneling. When the bias voltage is 0.63 V in Fig. 28, there are 35 states involved in the tunneling process. Among the 35 states, one is the ground state, seven are

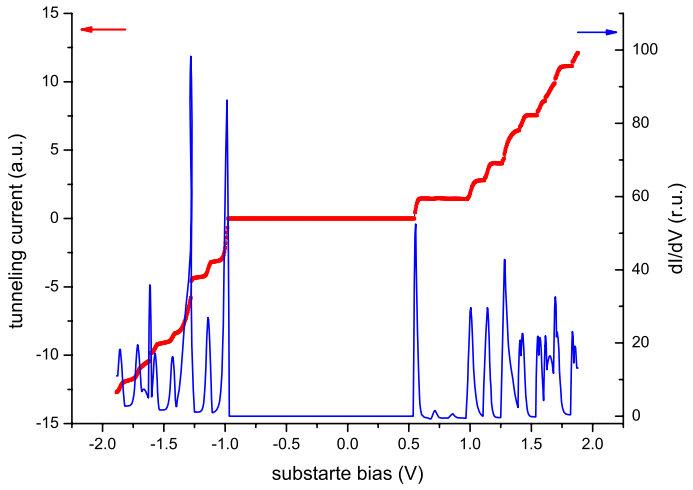

Figure 28: The numerical dI/dV-V and I-V curve for both bias directions. Parameters used are listed in Table 3

states with net charge $(-e + Q_0)$, and the rest are states with electron-hole pair. When bias voltage is 0.8 V, there are 96 states involved in the tunneling. The rapid increase of states is because of the rapid increase of possible combinations of electron-hole pair. When the bias is 1.01 V, there are 470 states involved in the tunneling. Among them there are states with net charge $(-2e + Q_0)$ and $e + Q_0$. Two things should be emphasized here. One is that at this bias it is impossible to charge the nanocrystal to $(-2e + Q_0)$ just by adding two electrons sequently to the ground state. Figure 22 can be used to explain why doubly charged states are involved in the tunneling when the bias is 1.01 V. The other thing is that it is also impossible to directly extract one electron from ground state to create a hole in the nanocrystal when voltage is at 1.01 V. The existence of the state with $(e + Q_0)$ when voltage is 1.01 V can also be explained using Fig. 22.

Now we try to explain the magnitude of the second and the third peak in Fig. 27. As we said earlier, these two peaks correspond to adding one electron to the second and the third unfilled electron level of the ground state. Once one more electron level is directly accessible, there are more pathways to move electrons from the tip to the substrate. We expect there is a jump of tunneling current. But in Fig. 26, there is almost no significant

change of the current when the bias increases from 0.63 V to 0.8 V.

We count the current by summing all the rate at which electrons tunnel from the nanocrystal to the substrate. This summation is over all states involve in tunneling at that particular bias voltage and over all possible energy levels of those states. At 0.63 V, the numbers of states with net charge $(0e+Q_0)$ and $(-e+Q_0)$ are 28 and 7 respectively. We know at this bias, it is impossible to extract one electron from the nanocrystal to change the net charge from $(0e+Q_0)$ to $(+1e+Q_0)$. Therefore only 7 states can contribute to the tunneling current. When the bias voltage is 0.8 V, the numbers of states with net charge $(0e+Q_0)$ and $(-e+Q_0)$ are 76 and 20 respectively. So when the voltage increases from 0.63 V to 0.8 V, the ratio of the number of states which can contribute to the tunneling current to the number of states which can't doesn't change much. The ratio is 0.2 for 0.63 V and 0.2083 for 0.8 V. The tunneling rates are almost same for electron levels close to the highest filled level of the ground state because the work function determines the tunneling rate. Therefore we expect the summation of Eq. 66 doesn't change much. This explains why the second and the third peak are so small.

3.3.2 Simulation B

The purpose of this simulation is to illustrate how the hole levels affect the current-voltage curves. Parameters used here are listed in Table 6. The choice of the capacitances are chosen to let the $e^2/2(C_1+C_2)$ be 0.25 eV. The level spacing below the Fermi level (hole level spacing) is smaller than the level spacing above the Fermi level (electron level spacing). The calculated tunneling current for the forward bias direction (the tip is biased negatively relative to the substrate) is plotted in Fig. 29. Some voltages are calculated and listed in Table 7.

In the Fig. 29, voltages at which the tunneling current has a sudden jump are marked with red and blue arrows. Corresponding voltages are used to label each arrow. Voltages for red arrows can be found in the left column of Table (7). Those for blue ones are in the right column. The mapping is one-to-one (the calculation stops before the bias is 1.333 V). Both the first red and the first blue arrows will produce positive big peaks in the dI/dV

Table 6: Parameters for simulation B.

C_1	0.9 (e/V)
C_2	1.1 (e/V)
d_1	4.8 Å
d_2	4.0 Å
hole level spacing	0.09 eV
electron level spacing	0.1 eV
residual charge	0.2 e
work functions	6 eV
temperature	77 K

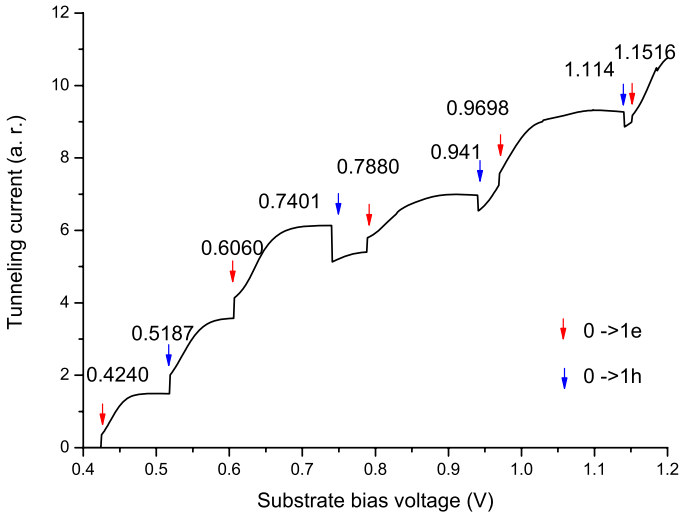

Figure 29: Calculated tunneling current curve for parameters listed in Table 6. Voltages marked with red arrows are related to tunneling processes changing the charge from -ne+Q_0 to -(n+1)e+Q_0. Voltages marked with blue arrows are related to tunneling processes changing the charge from -ne+Q_0 to -(n-1)e+Q_0.

Table 7: Minimum bias voltages for some tunneling processes in simulation B. Voltages in the left column are minimum voltages needed for directly adding one electron to empty levels of the ground states. Higher minimum voltages corresponds to higher electron levels. Voltages in the right column are minimum voltages needed for extracting one electron from the ground state. The higher voltages correspond to deeper levels below Fermi level.

$Q_0 \rightarrow -e + Q_0(V)$	$Q_0 \rightarrow e + Q_0(V)$
0.424	0.5187
0.606	0.7401
0.788	0.941
0.9698	1.114
1.1516	1.34
1.333	1.54

plot. Actually they are both related to the first empty level of the ground state. 0.424 V corresponds to the tunneling process in which one electron tunnels from the tip to the first empty level of the ground state. This process changes total charge on the nanocrystal from Q_0 to $(Q_0 - e)$. 0.5187 V corresponds to the process in which one electron tunnels out to the substrate from the first level above the Fermi level. But this time the state before the tunneling event is not the ground state. It is a state which has one electron above the Fermi level and one hole below the Fermi level (For simplicity, we assume the Fermi level are same for all states). This tunneling event changes the total charge from Q_0 to $Q_0 + e$. This is very interesting since two well separated peaks correspond to one electron level of the nanocrystal.

The other interesting feature of Fig. 29 is the current dips at other voltages marked by blue arrows. At these voltages, events in which electrons tunnels from "hole" levels to the substrate increases. Usually electrons on "hole" levels see higher barrier than those on "electron" levels. So the average tunneling rate decreases. Therefore the total tunneling current decreases.

The dips in the tunneling current means negative differential conductance. In the before, Terry Bigioni measured dI/dV spectra of gold nanocrystals [4]. Figure [4] shows a measured dI/dV versus V curve. The curve has a deep valley where negative differential conductance

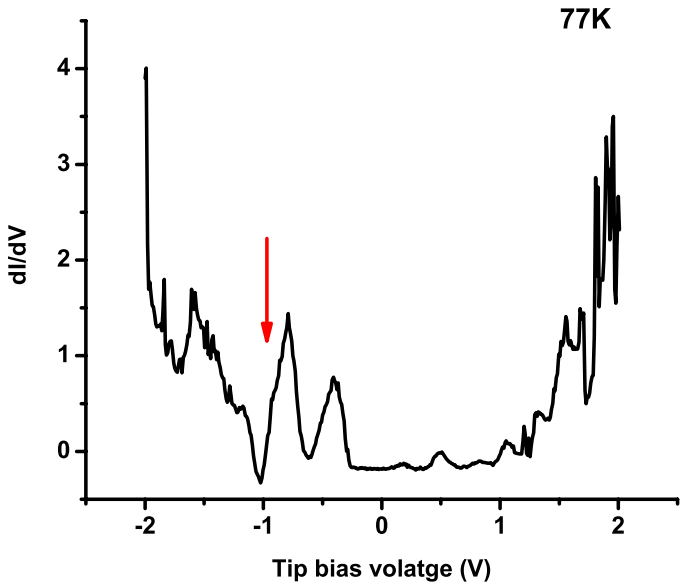

Figure 30: Measured dI/dV curve of a gold nanocrystals at 77 K. The valley marked with the red arrow has negative value [4].

exists. The simulation here maybe can be used to explain the appearance of negative differential conductance.

3.3.3 Simulation C

The purpose of this simulation is to show how the residual charge changes the meaning of band gap in tunneling spectroscopy. Parameters used in this simulation are listed in Table 8. Residual charge Q_0 is negative now.

For the parameters listed in Table (8), we calculate the minimum voltages needed to start the tunneling for both bias directions. When the tip is biased negatively relative to the substrate, electrons will tunnel for the tip to the substrate. The minimum voltage V_1 needed to add one electron to the ground state of the nanocrystal is determined by the following equation:

$$\frac{C_2}{C_1 + C_2} eV_1 = \Delta(E_c(0- > 1e)) + E_n(1) - \frac{3}{2}kT \tag{69}$$

Where $E_n(1)$ is the first empty electron level above the Fermi level. V_1 is 0.7880 V. The

minimum voltage V_2 needed to extract one electron from the ground state to the substrate.

$$\frac{C_1}{C_1+C_2}eV_2 = \Delta(E_c(0- > 1h)) - E_n(0) - \frac{3}{2}kT \tag{70}$$

Where $E_n(0)$ is the highest occupied level of the ground state. V_2 is 0.2964 V. So V_2 is the minimum voltage to start the tunneling when the tip is biased negatively to the substrate.

For the reverse bias case in which the tip is biased positively to the substrate, electrons tunnel from the substrate to the tip. The corresponding voltages to V_1 and V_2 are:

$$\frac{C_1}{C_1+C_2}eV_3 = \Delta(E_c(0- > 1e)) + E_n(1) - \frac{3}{2}kT \tag{71}$$

and

$$\frac{C_2}{C_1+C_2}eV_4 = \Delta(E_c(0- > 1h)) - E_n(0) - \frac{3}{2}kT \tag{72}$$

V_3 is 0.9631 V and V_4 is 0.2425 V. So the minimum voltage to start the tunneling for the reverse bias direction is V_4. The sum of V_2 and V_4, 0.5389 V, is the voltage gap at the center of the current-voltage curve. The simulated current voltage curve is shown in Figure (31). The current voltage curve for $Q_0 = 0.2e$ is also shown in the same figure for comparison. Except the value of Q_0, all other parameters are same for two curves.

From above equations, we have the voltage gap ΔV_1 for $Q_0 = -0.2e$:

$$\Delta V_1 = \left(\frac{1}{C_1}+\frac{1}{C_2}\right)\left(\frac{1}{2}(e^2+2eQ_0) - E_n(0) - \frac{3}{2}kT\right) \tag{73}$$

The corresponding voltage gap $\Delta V_2$for $Q_0 = 0.2e$ case is

$$\Delta V_2 = \left(\frac{1}{C_1}+\frac{1}{C_2}\right)\left(\frac{1}{2}(e^2-2eQ_0) + E_n(1) - \frac{3}{2}kT\right) \tag{74}$$

Voltage gap ΔV_1 and ΔV_2 can't be simply related to meaningful quantities of the system.

This is contrast to the system in simulation A. In simulation A, tunneling begins across junction 1 for both bias direction. The corresponding voltage gap in that case is:

$$\Delta V = \frac{C_1+C_2}{C_2}\left[\frac{e^2}{C_l+C_r} + E_n(1) - E_n(0) - 3kT\right] \tag{75}$$

The first term inside the brace is related to the charging energy. The sum of the second and the third term is the energy gap between the lowest unoccupied level and the highest

Table 8: Parameters for simulation C.

C_1	0.9 (e/V)
C_2	1.1 (e/V)
d_1	4.8 Å
d_2	4.0 Å
hole level spacing	0.09 ev
electron level spacing	0.1 ev
residual charge	-0.2 e
work functions	6 ev

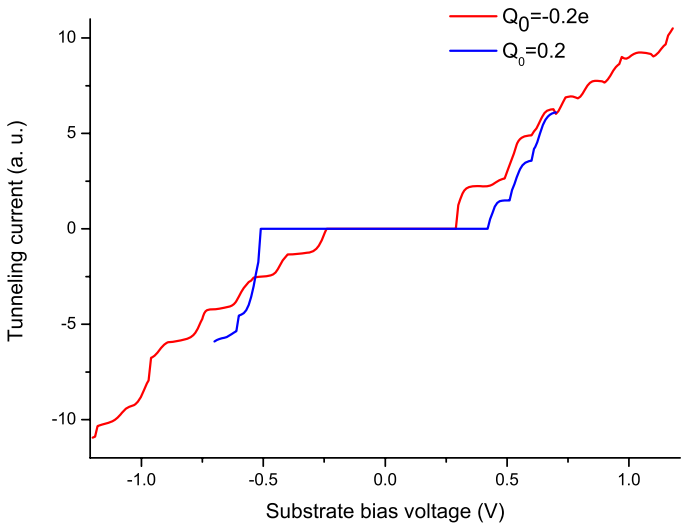

Figure 31: Tunneling currents for different residual charges. All other parameters are listed in Table (8).

occupied level of ground state. The last term at the right side is just related to thermal broadening. This voltage gap has some physics meaning. If the charging energy is negligible, then ΔV is proportional to the intrinsic band gap inside the nanocrystal. This case is proper for tunneling spectroscopy of semiconductor nanocrystals. For that case, the size dependence of voltage gap is a direct indication of the size dependence of energy gap.

CHAPTER IV

SIMULATION OF BEEM SPECTRUM OVER NANOCRYSTALS

4.1 Introduction to BEEM and BEES

Ballistic Electron Emission Microscopy (BEEM) is a variation of scanning tunneling microscopy which is developed soon after the invention of STM [40]. BEEM has every component that a conventional STM has. But BEEM has one more connection which is used to collect the so called BEEM current. Figure 32 shows the basic setup of a BEEM experiment. A very thin (∼10 nm) layer of gold is deposited on silicon. One lead, the tunneling (or base) lead, is connected to the surface of this thin gold film. Another lead, the BEEM (or the collector) lead, is connected to the silicon below the gold film. The STM tip is biased negatively with respect to the gold film. The tip, the base lead, and the external circuit forms a complete STM. When the tip is scanned the surface of the gold film, the majority of the electrons tunneling out from the tip will be collected by the base lead. This current is the tunneling current (or base current) and is fed back to the servo to provide control of the tip position. A very small portion of the electrons ($\sim 1\%$) will enter the silicon and be collected by the BEEM lead. This current is the BEEM current.

When an electron moves inside a solid, it experiences forces from atoms and other electrons. In an ideal lattice without electron-electron (e-e) or electron-phonon (e-p) interactions, the electron will be in a stationary Bloch state. It moves without any resistance. But in reality, the lattice has defects and impurities. These defects and impurities will introduce perturbations from which the electron can scatter. Scattering can change the momentum and the energy of the electron. The e-p interaction originates from the potential perturbations due to the deviation of atoms from their equilibrium positions. High energy electrons usually lose energy via phonon emission. The mean free path is the average

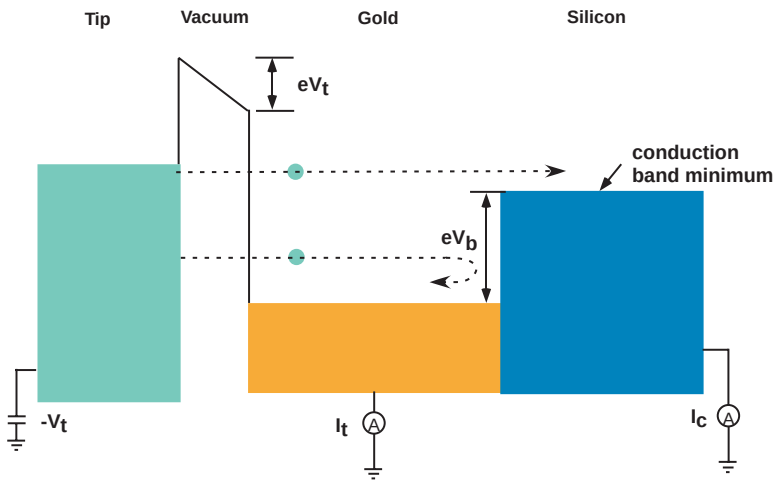

Figure 32: Illustration for the basic setup of a BEEM experiment. The left is a negatively bias tip. $-V_t$ is the tip voltage. Thin gold film is grown on clean silicon surface. eV_b is the Schottky barrier formed at the interface between the gold and the silicon. Electrons coming from the tip with high energy can overpass the Schottky barrier and form the BEEM current I_c. Most of the electrons will be collected at the gold base and form the tunneling current I_t. The gold and silicon should have same potential.

distance an electron travels before losing its initial momentum, energy, or phase (depending one's interest). In Fig. 32, if the thickness of the gold film is smaller than the mean free path both for momentum and energy, then some of the electrons can cross the gold film without experiencing any scattering. When these electrons approach the interface some of them have the same energy and momentum as when they entered the surface of the gold film.

The energy of electrons tunneling out from the tip can be controlled by the tip bias voltage. When the tip is biased at $-V_t$, all energy levels inside the tip are raised by eV_t with respect to the substrate. Electrons of the occupied levels in the tip tunnel into the gold film. When eV_t increases, the average energy of the electrons entering the gold increases. At the interface of the gold and the silicon, the energy difference eV_b between the Fermi level of gold and the silicon conduction band minimum forms an energy barrier for electron to enter the silicon. This barrier is called Schottky barrier and is about 0.8 eV for the gold-silicon interface. When the tip bias is high enough, some of the electrons entering the gold will have energy higher than the conduction band minimum of silicon. If these electrons cross

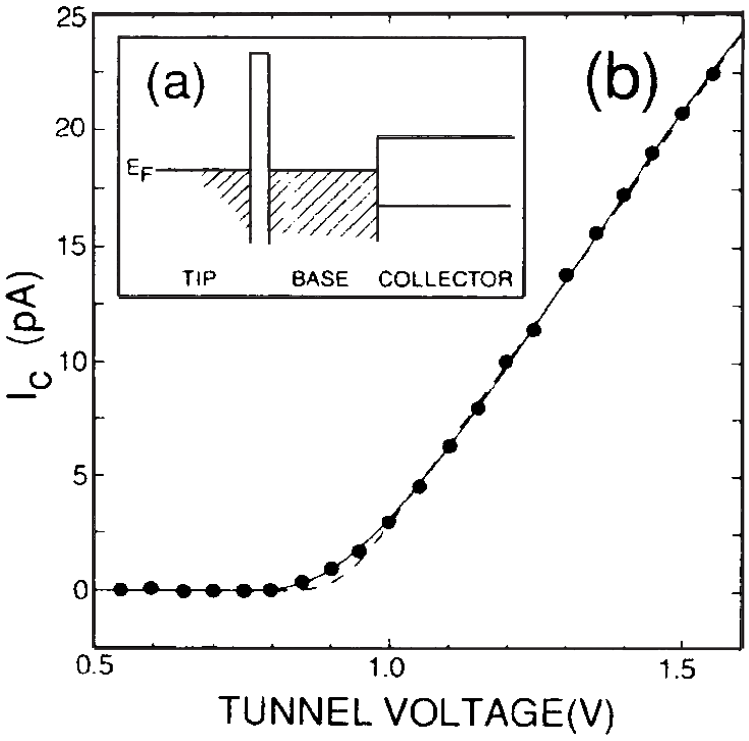

Figure 33: (a) Energy band diagram. (b) The collector current vs voltage curve for gold on silicon. The dots are measured data. Solid and dashed lines are calculated curves. The threshold voltage for BEEM current is 0.82V [17].

the thin gold film without scattering, they can pass the energy barrier and enter the silicon. Those which have energy lower than the conduction band minimum or lose energy due to the scattering in the gold can't pass the Schottky barrier. The Schottky barrier basically forms a high-pass energy filter for the tunneling electrons. The BEEM current only consists of the electrons with energy higher than the conduction band minimum of silicon.

Ballistic electron emission spectroscopy (BEES) is the spectroscopy mode of BEEM experiments. The BEEM current is measured as a function of the tip-base bias voltage. The measurement is usually done with the tunneling current is kept at a constant value. Figure 33 shows a BEEM current versus voltage curve for gold and silicon system [40]. When the tip bias voltage V_t is smaller than V_b, there is no BEEM current. When the bias voltage increases above the turn-on voltage V_b, the BEEM current begins to increase from zero.

One application of BEEM/BEES is to measure the Schottky barrier at the metal-semiconductor interfaces of metal and semiconductor materials. This type of measurement provides very accurate information about the band alignment between metal and semiconductor materials. Compared with other characterization techniques, the advantage of BEEM/BEES is the high lateral resolution. The lateral resolution can be of the order of 1 nm. This is ideal for investigating lateral variation of interface quality or Schottky barriers. BEEM/BEES has also been used to investigate other heterostructure systems. Band alignment at the interface of different semiconductor layers is a very important problem in microelectronics. BEEM can be used to measure the band offset at the interface. BEEM is also used to investigate the ballistic transport of quantum well structures like double-barrier resonant tunneling structures.

In the previous chapter, we showed that there are a lot of excited states involved in the tunneling process. As mentioned in chapter III, STM spectroscopy can't tell the origins of dI/dV peaks. Peaks could be due to hole levels or electron levels. But if electrons come from "hole levels" of the nanocrystal, i.e. those levels fully occupied at T=0 in the initial state, the energy of these electrons would be lower than those from electron levels. Since BEES filters the electron energies, current versus voltage ($I_c(V)$) curves may suppress some feature seen in STS spectra. In principle, by comparing BEES and STS spectra, more information could be extracted.

Another motivation for applying BEES to nanocrystals is to study dynamic processes inside nanocrystals. The knowledge of dynamics inside nanocrystals is valuable for future applications of quantum dots or nanocrystals, especially in optoelectronics and "single-electron" devices. The dynamical properties like relaxation time will directly affect the performance of device based on quantum dots or nanocrystals. Relaxation processes are related to electron-electron and electron-phonon interactions in confined systems. Thus study of dynamics inside nanocrystals could shed light on some very important physics problems.

There has been extensive works on dynamical processes inside nanocrystals in the last 15 years. Most studies utilizes ultra-fast optical spectroscopy. The typical experiments are

the pump-probe type. An ultrafast optical pulse (the pump pulse) is used to excite electrons and holes inside nanocrystals. After a controlled time delay, another ultra-fast pulse (the probe pulse) is used to detect the change of optical properties such as transmission or reflection. After the pump pulse, electrons inside nanocrystals absorb photon energy and are excited above the Fermi level. This changes the electron distribution. For example, after excitation by the pump pulse, nanocrystals will have many holes below the Fermi level and same number of electrons above the Fermi level. At this time, the electron distribution is not described by the Fermi-Dirac function. This non-equilibrium distribution affects the optical absorbtion greatly. The probe pulse provides information about optical absorption by monitoring, for example, the change of transmission coefficient. The absorption is related the electron distribution. Electron distribution will change by e-e interactions. Therefore monitoring the change of transmission coefficient in time domain by varying the delay time of the probe pulse can illustrate the e-e integration in nanocrystals.

After excitation by the pump pulse, the electron distribution will achieve an equilibrium in a very short time (few hundreds of femto seconds) via e-e interactions. But the electron system will be in a temperature higher than the temperature of the lattice. Then the e-p interaction will transfer some energy from the electron gas to the lattice. Gradually the electron gas comes to thermal equilibrium with the lattice. This relaxation due to e-p process is slower than the relaxation due to e-e scattering. For gold nanocrystals, the relaxation time due to e-p interaction is about 1 picosecond [37].

Figure 34 shows the change of the transmission with time for nano particles with diameter of 11 nm. The change of transmission decays exponentially.

$$\frac{\Delta T}{T} \propto \exp[-\frac{t}{t_{ep}}] \tag{76}$$

Whether these relaxation time constants change with size and how are under intensive debate. The e-e interaction is not the bare Coulomb interaction between two point charges. This interaction is mediated by the presence of other electrons. If the electron density is high, the e-e interaction is reduced by screening coming from the other electrons. In small nanocrystals, the total number of electrons is limited because the number of atoms

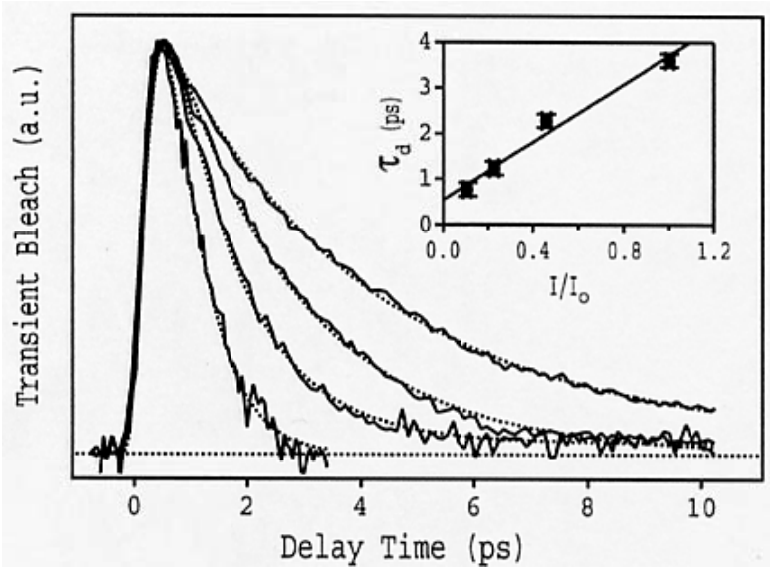

Figure 34: Transient bleach versus delay time data for $\sim$ 11 nm diameter gold nano particles. Different traces correspond to different pump pulse intensities. Higher power gives slower decays. The insert shows a plot of the decay constant versus relative pump laser intensity [37].

is small. Therefore the interaction between two electrons can't be screened as well as in bulk materials. The larger surface-to-volume ratio is another very important factor for the relaxation time constant. Near the surface one electron is surrounded by less other electrons than in the core of the nanocrystal. It is expected that the e-e interaction happened at the surface is stronger than inside the nanocrystal. So the "average" e-e interaction in small nanocrystals is stronger than in the bulk material [13, 57]. Stronger interaction means faster relaxation. Therefore the e-e relaxation time constant is supposed to increase when the size decreases. This trend should also apply to the e-p interaction. The e-p interaction is basically the interaction between electron and ion. The strength also depends on the screening efficiency.

Figure 35 shows the size dependence of the e-p relaxation time constant for gold nanocrystals. Different groups give different result.

The situation is even more complicated for very small nanocrystals. For gold, very stable nanocrystals composed of 11 atoms and 28 atoms have been synthesized. The study of relaxation in Au_{11} shows that the e-p relaxation time constant is as long as 526 picosecond

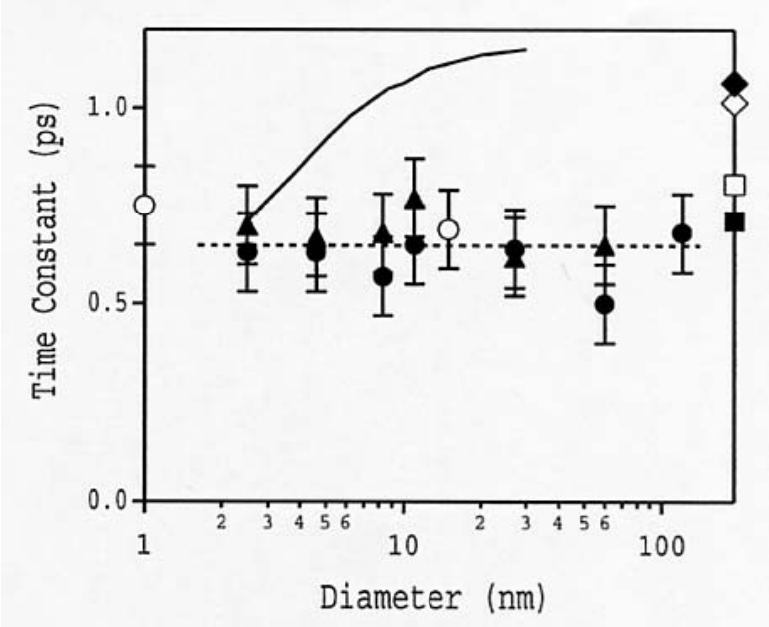

Figure 35: Decay time constants due to e-p interaction as a function of the diameter. Different groups give different values. Close triangles and closed circles are measured by Hartland and co-workers [37]. Solid lines are data measured by Voisin and co-workers. Open circles are data measured by El-Sayed and co-workers. The symbols on the right axis are measured data of the bulk material by different groups. See [37] and references therein.

[33]. This long time constant can't be simply explained by the reduced interaction between electrons and ions. Experiments show that there is a big energy gap between the highest occupied level and the lowest unoccupied energy level. People tend to believe that these gold nanocrystals are more like molecules than metal clusters [42].

One of the problems related to ultra-fast optical spectroscopy is that the relaxation time is intensity dependent. In order to accurately measure the relaxation time, the optical intensity should be as low as possible. But when the intensity is low, the signal-to-noise ratio is also lowered. So it is not likely that optical spectroscopy can provide information about single electron excitation inside nanocrystals. Another issue related to optical spectroscopy is that optical measurements are always an average over many nanocrystals. The size dispersion of nanocrystals makes the data less accurate. Optical measurements are also affected by the time response of the measurement equipment. This poses another restriction to the optical measurements.

BEES experiments can be used to provide information about relaxation processes inside nanocrystals and bypass some of the difficulties mentioned above. In our BEEM/BEES experiments, if the tunneling current is kept at constant of 100 pA, then the average time for moving one electron from the tip to the substrate is about 1.6 ns. The residence time for electrons on the nanocrystal should be of the same magnitude. If the time for electrons to relax from higher levels to lower levels through e-p interaction is shorter than 1 ns, then relaxation would affect the magnitude of the BEEM current. If relaxation exists and is faster than the average transport time of tunneling electrons, then electrons coming out from the nanocrystal will already have lost some energy to the lattice of the nanocrystal. Therefore fewer of these electrons can overcome the Schottky barrier. For example, if the threshold voltage for charging the nanocrystal is lower than the Schottky barrier and all tunneling electrons relax to the lowermost level on the nanocrystal, then all electrons tunneling off the nanocrystal will have energy lower than the Schottky barrier. We would expect the BEEM current to be zero in this case. The advantage of BEES is that one can study a single nanocrystal in the regime of single-electron excitation. Tunneling events are discrete. At lower bias, most of the time there is only one extra electron or hole on the nanocrystal.

STM can resolve single nanocrystals on surface, therefore the BEEM/BEES measurement is not an ensemble average over nanocrystals with different size. The measured data can be directly related to the size measured simultaneously by STM.

Some BEEM/BEES works on semiconductor quantum dots has been done by others. Reddy and co-workers investigated two systems. One was AlInP quantum dots capped inside GaP [52]. The other was InP quantum dots capped inside AlInP [53]. Figure 36 shows the latter system. Figure 36(a) is a cross section of the structure. A layer of AlInP was grown on the GaAs substrate. An amount of InP equivalent to 40 monolayers was then deposited on the surface of AlInP. InP self-assembled into 3-dimensional quantum dots instead of forming an uniform layer. Another layer of AlInP was deposited to cover the InP quantum dots. Because of the band offset between InP and AlInP, two layers of AlInP form potential barriers for electrons residing in the InP quantum dots. Finally, a GaAs was deposited, followed by a base layer of gold. Figure 36 (b) shows the BEES current versus voltage curves collected on and off the quantum dots. The current is enhanced on quantum dots since a quasi-bound levels of the InP quantum dots enhances electron transmission below the AlInP barrier.

The BEEM/BEES experiment we undertake is different from above. We first grow a thin layer of Au on silicon(111) as the base layer. A xyendithiol self-assembled monolayer (SAM) is then grown on the gold [18, 19]. Nanocrystals of gold or semiconductor will be deposited onto the top of the xylenedithiol SAM. The sample is shown schematically in Fig. 37. In order to better understand our BEES experiments, computer simulations were performed to calculate the BEES current versus voltage spectra in the next section. The tunneling current calculation presented in the previous chapter serves as the input for the calculation of the BEEM collector current versus applied voltage $I_c(V)$.

4.2 Simulation of BEES $I_c(V)$ Spectra

4.2.1 Transport Coefficient Across the Au-Si(111) Surface.

The early theory of BEEM models the metallic base and the semiconductor using free electron band structure with appropriate effective mass [40]. This simple picture can only

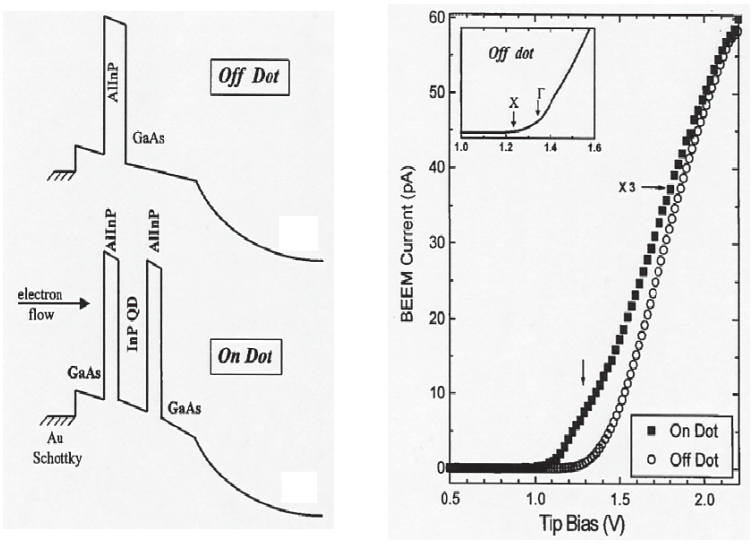

Figure 36: (a) Band diagram for the InP quantum dot system. The conduction band offset between InP and AlInP forms a well for electrons in InP. InP is self-assembled to quantum dots. (b) BEES I-V curves measured on and off quantum dots. Insert is the specially averaged BEES I-V [53].

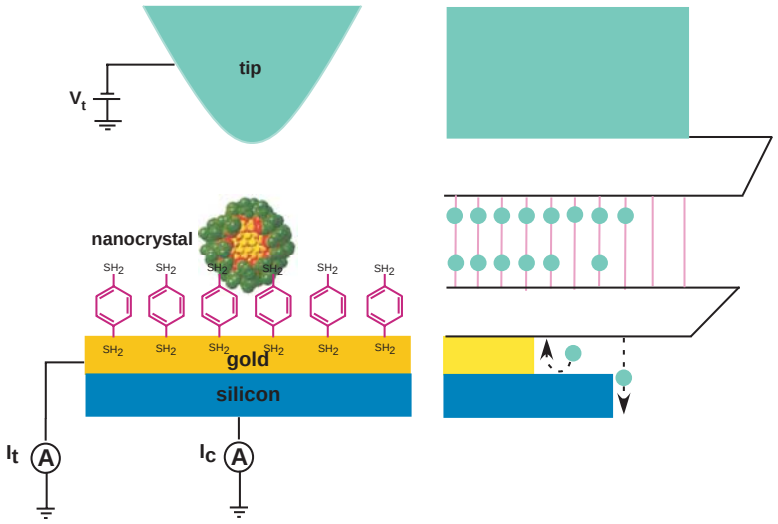

Figure 37: The setup for BEES experiments on gold nanocrystals.

be applied to electrons with energy close to the conduction band minimum where the band can be approximated as parabolic. This model also assumes that the conduction band minimum is at the zone center. Electron states inside the metal are described by k and $E(k)$.

For gold nanocrystals under investigation, the bias voltage used can be as high as 1.5 volts. If electrons starting from the tip don't lose energy before they enter the silicon, then some of them have energy far above the conduction band minimum of the silicon. Therefore, one simple parabolic band structure is not appropriate. For silicon, the second band minimum is only 1 eV higher than the first minimum. In order to describe the transport process accurately, we can't neglect the other second band minima.

The second difficult comes from the scattering of the non-epitaxial metal base and the scattering at the metal-semiconductor interface. Non-epitaxial base makes free electron model a very good one. But the increased scattering make the transport less ballistic. The scattering also change the k distribution when electrons move across the base. The scattering at the interface makes the parallel momentum not conserved across the interface anymore. Some work has addressed this problem [55].

Because of the difficulties mentioned above, we will not model the detailed transport process inside the gold and silicon. We extract the information from experimental data as far as possible. As for the momentum distribution of injected electrons with fixed energy in the metal base, we assume that it is the same for tip-gold-Si system and tip-nanocrystal-gold-Si system. Figure 38 shows the tip-gold-Si system. The tunneling current I_t is:

$$I_t = \int_{E_f}^{E_f+eV} eD(E)\Gamma(E,V)dE \tag{77}$$

The BEEM (collector) current is

$$I_c = \int_{E_f+eV_b}^{E_f+eV} eD(E)\Gamma(E,V)T(E)dE \tag{78}$$

The energy reference point is the bottom of the gold conduction band. V is the tip bias relative to the metal. eV_b is the Schottky barrier between gold base and the silicon collector. $\Gamma(E,V)$ is the tunneling rate from the tip to the gold film. $T(E-E_f-eV_b)$ is the

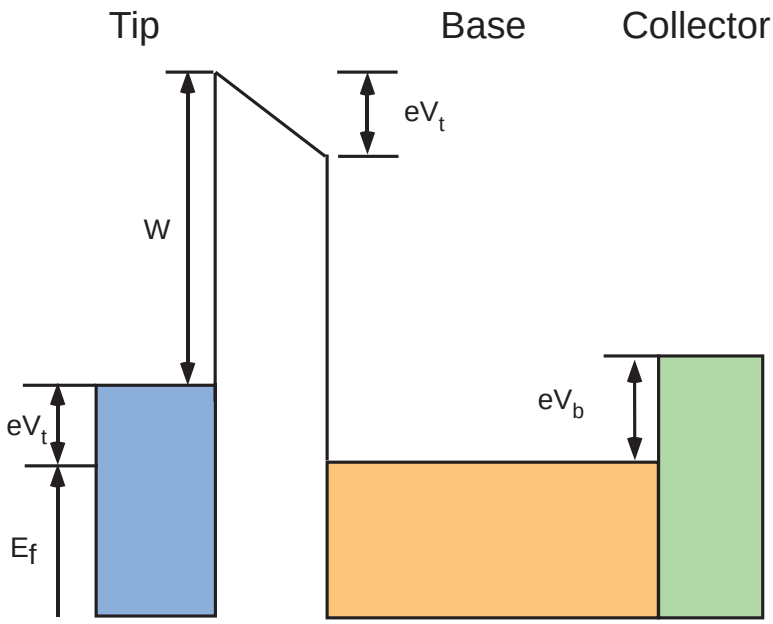

Figure 38: Energy diagram for BEEM experiments. Left blue area is the tip. Middle yellow is the gold base layer. The right green area is the silicon collector. E_f is the Fermi surface of the gold film. When bias voltage V_t is zero, the Fermi levels of the tip and the gold base are aligned (the reference point for electron energy is at the bottom of the gold conduction band). At bias V_t, the energy of electrons at the tip Fermi surface is $E_f + eV_t$. W is is the work function of the tip. eV_b is the Schottky barrier at the gold-silicon surface.

transmission rate of electrons across the gold-silicon interface. $T(E - E_f - eV_b)$ is zero for $E < E_f + eV_b$. In Eq. 77 and Eq. 78, $\Gamma(E)$ and $T(E - E_f - eV_b)$ are the averaged value over different k with the same energy E. $D(E)$ is the electron density inside the tip. We assume it is a constant in the range we are interested.

The derivatives of I_t and I_c over V are:

$$\frac{\partial I_t}{\partial V} = \int_{E_f}^{E_f+eV} eD(E)\frac{\partial \Gamma(E,V)}{\partial V}dE + e^2 D(E_f + eV)\Gamma(E_f + eV, V) \tag{79}$$

$$\frac{\partial I_c}{\partial V} = \int_{E_f+eV_b}^{E_f+eV} eD(E)\frac{\partial \Gamma(E,V)}{\partial V}T(E-E_f-eV_b)dE+e^2 D(E)\Gamma(E_f+eV,V)T(E_f+eV) \tag{80}$$

The tunneling rate $\Gamma(E, V)$ is modeled as the rate of planar tunneling [54]. For an electron with energy E inside the tip, the rate at which the electron tunnels to the gold base is:

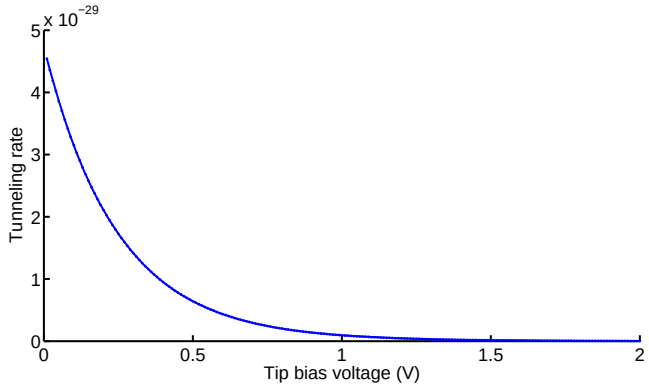

Figure 39: Tunneling rate defined in Equation (81) as a function of tip bias for fixed energy. For electrons with fixed E (with respect to $E = 0$ in the base), the barrier increases while V increases. So $\Gamma(E, V)$ decreases.

$$\Gamma(E,V) = \exp\left[-\frac{4\pi}{\hbar}(2m)^{\frac{1}{2}}\int_0^d [W(x,V) - (E - E_f - eV)]^{\frac{1}{2}}dx\right] \tag{81}$$

d is the distance between the tip and the gold surface. Here we assume initially work functions of the gold and the tip are same. $W(x, V)$ is related to the work function W_0 of the tip.

$$W(x,V) = W_0 - eV\frac{x}{d} \tag{82}$$

The origin of x is at the tip surface. $\Gamma(E, V)$ is plotted as a function of V at $E = 1eV$ for $W_0 = 5eV$ and $d = 0.5nm$ in Fig. 39. The reason why $\Gamma(E, V)$ decreases when V increases is that E is relative to the fixed conduction band of the gold. The barrier for electrons with energy E is $W_0 + E_f + eV(1 - \frac{x}{d})$. For the same E, the barrier shifts upwards when V increases. Therefore $\Gamma(E, V))$ decreases with V when E is fixed.

Now we estimate the relative magnitude of two terms in Eq. 79. The ratio of the second to the first term is plotted in the Fig. 40. The second is several orders of magnitude smaller than the first term. Therefore we have the following good approximation.

$$\frac{\partial I_t}{\partial V} \approx \int_{E_f}^{E_f+eV} eD(E)\frac{\partial\Gamma(E,V)}{\partial V}dE \tag{83}$$

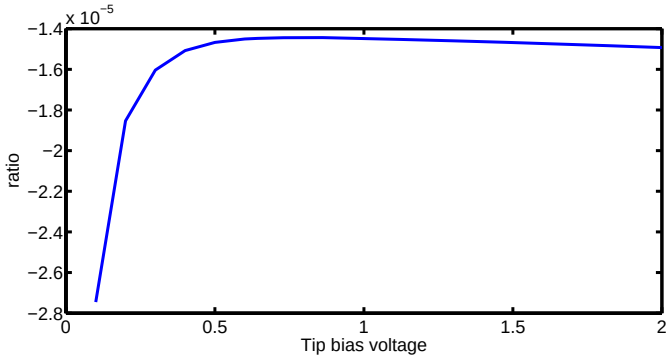

Figure 40: The ratio of the second term to the first term in Eq. 79.

$$\frac{\partial I_c}{\partial V} \approx \int_{E_f+eV_b}^{E_f+eV} eD(E)\frac{\partial \Gamma(E,V)}{\partial V}T(E)dE \tag{84}$$

$\partial\Gamma(E,V)/\partial V$ is calculated and displayed in Fig. 41 as a function of E at V=2 V. It increases exponentially. The y axis is $\partial\Gamma(E,V)/\partial V$ and x axis is the energy in electron volts. The green area under the $\partial\Gamma(E,V)/\partial V$ curve is just the integral at the right side of Eq. 83. The left side blue rectangle has the same area as the green one. Its height is $\partial\Gamma(E,V)/\partial V|_{E=V}$. The width is only 0.1227 ev. Therefore we have a good approximation for $\partial I_t/\partial V$:

$$\frac{\partial I_t}{\partial V} \approx eD\left.\frac{\partial \Gamma(E,V)}{\partial V}\right|_{E=E_f+V}\Delta E_t \tag{85}$$

Where ΔE_t is about 0.12 eV. Similarly we have the approximation for $\partial I_c/\partial V$.

$$\frac{\partial I_c}{\partial V} \approx eD\left.\frac{\partial \Gamma(E,V)}{\partial V}\right|_{E=E_f+V}T(E_f+eV))\Delta E_c \tag{86}$$

ΔE_c is similar to ΔE_t.

From above two equations, the transmission rate across the gold-silicon interface can be expressed as:

$$T(E_f+eV) \approx \frac{\Delta E_t}{\Delta E_c}\frac{\partial I_c/\partial V}{\partial I_t/\partial V} \tag{87}$$

The factor $\Delta E_t/\Delta E_c$ is chosen as 1.5. The reason is that $\frac{\partial\Gamma(E,V)}{\partial V}T(E)$ changes faster than $\frac{\partial\Gamma(E,V)}{\partial V}$. Therefore ΔE_B is smaller than ΔE_t.

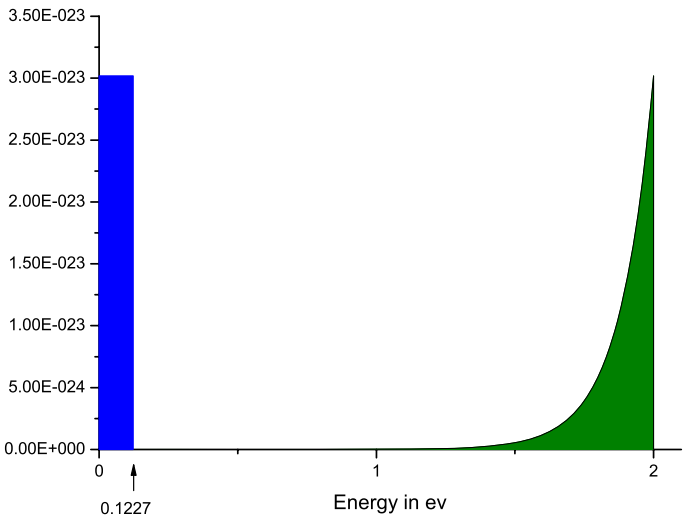

Figure 41: $\partial\Gamma(E,V)/\partial V$ as a function of E at $V = 2V$. $\partial\Gamma(E,V)/\partial V$ increases exponentially with V. The blue block at the left side has the same area as the green area. The height of the blue area is same as $\partial\Gamma(E,V)/\partial V$ at the end of E and the width is 0.1227 eV.

In the previous chapter, the tunneling current was simulated. In that simulation, the energy of each electron coming out of the nanocrystal can be tracked. Therefore, the BEES current can be calculated easily by multiplying $T(E)$ with the tunneling rate of electrons with energy higher than $E_f + eV_b$.

On the experimental side, for a nanocrystal sample, we first chose an area which didn't have any nanocrystals. Once the STM tip was there, the feedback wa disabled temporarily, so that distance between the tip and the gold surface was fixed. Then the tunneling current versus voltage curve and the BEES current versus voltage curve were measured by sweeping the bias voltage. Figure 42 shows the simultaneously measured tunneling current I-V and BEES current I-V. The $T(E)$ curve is extracted and plotted in Fig. 43(b). In the following simulation, the smoothed curve will be used. This is because that the features in the extracted $T(E)$ will create features in the simulated BEES I-V curves. These features would complicate the interpretation of the BEES I-V curves.

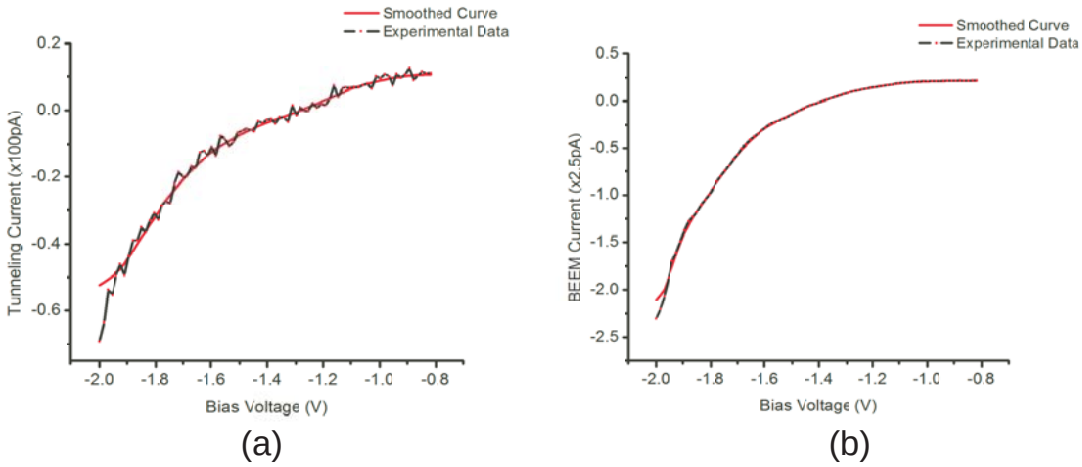

Figure 42: (a) Experimental tunneling current versus voltage curve. The black curve is the measured data. The red curve is smoothed by 5-points averaging. (b) BEEM current versus voltage curve. Black is the measured data. Red is the 5-point smoothed data running average.

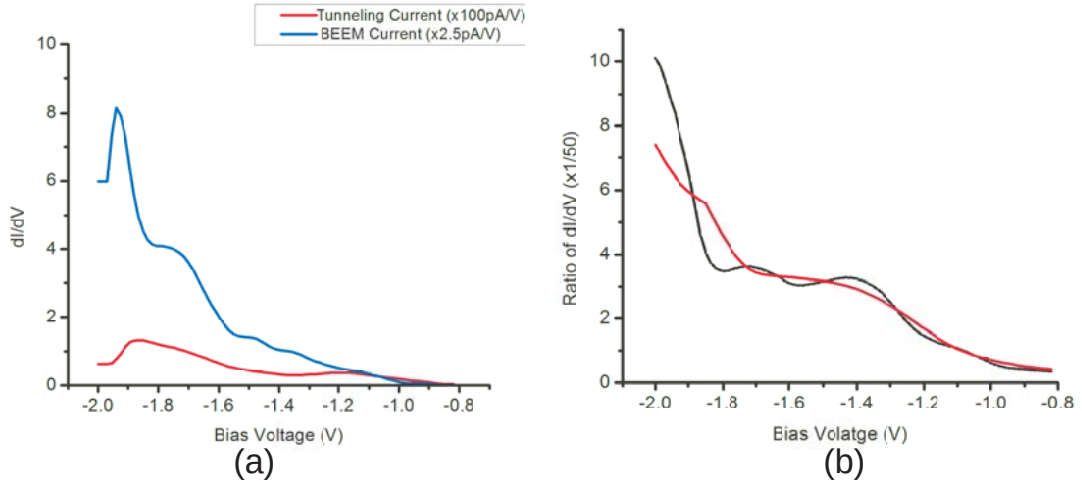

Figure 43: (a) The numerical dI/dV versus voltage curves for tunneling I-V and BEEM I-V in Fig. 42. (b) The ratio of BEEM dI/dV to tunneling dI/dV. The black curve is from (a) and smoothed by 5-point averaging. The red is 20-point averaging of the black curve.

Table 9: Parameters for simulation A.

C_1	0.9 (e/V)
C_2	1.1 (e/V)
d_1	4.8 Å
d_2	4.0 Å
hole level spacing	0.09 eV
electron level spacing	0.1 eV
residual charge	0.2 e
work functions	6 eV
temperature	77 K

4.2.2 Simulation A.

We now study how the nanocrystal and its coupling to the environment affect the BEES I-V curve. The parameters used for the following simulation are same as those for simulation B in Chapter III. They are listed in Table 9.

The BEES current calculated as described earlier and the tunnel current are plotted in Fig. 44. The calculation was done while keeping the distance between the tip and the surface to be constant. One of the striking features is that the threshold voltage for the BEES current is smaller than V_b (We set it to be 0.85 V in the calculation). Actually the BEES current is only zero when the bias voltage is below 0.5 V. When the voltage is 0.5 V, there is a very small probability for two electrons to occupy the lowest unoccupied levels of the ground state. The reason why this state appears when the bias voltage is only 0.5 V is the "self-pumping" we described in Chapter III. After a particular sequence of the tunneling-in and tunneling-out events, the nanocrystal can be doubly charged. The close look at the numerical simulation confirms this. The very weak BEES current starting from 0.5 V is due to electron tunneling out from this state. When one electron tunnels out of this state, a big portion of charging energy is added to the energy of this electron. When this electron is in the gold base, its energy could be higher than the conduction band minimum of the silicon.

There is a abrupt jump in the BEES current at 0.745 V bias. Above this threshold,

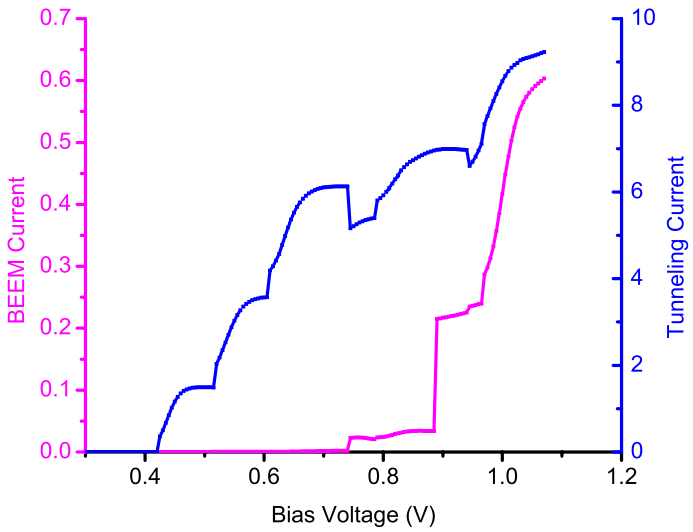

Figure 44: The BEES current and the tunneling current calculated using parameters in Table 9. The pink curve is the BEES current and the blue curve is the tunneling current.

if the nanocrystal is charged with one electron and the fourth unoccupied energy level of the ground state is occupied, then one electron tunneling out from the fourth level would have energy of 0.88 eV in the gold base. This energy enables the electron to overcome the Schottky barrier of 0.85 eV and enter the silicon to form BEES current. At this bias voltage, electrons can't directly tunnel onto the fourth unoccupied level of the ground state. So the probabilities of states which have electrons on the fourth level are small. Therefore the BEES current is still small. The jump of BEES current at 0.89 V can be explained in a similar way. This time electrons tunneling out from the third unoccupied level of the ground state can contribute to the BEES current. Compared with the jump at 0.745 V, the jump at 0.89 V is much bigger. This is because that at 0.89 V, electrons can directly tunnel onto the third unoccupied level of the ground state. Therefore the probabilities of states which have electrons on the third level are relatively large. Starting from 0.97 V, electrons can directly tunnel onto the fourth unoccupied level of the ground state. After that the BEEM current increases rapidly.

Table 10: Parameters for simulation B.

C_1	0.3 (e/V)
C_2	0.7 (e/V)
d_1	4.8 Å
d_2	4.0 Å
hole level spacing	0.1 eV
electron level spacing	0.1 eV
residual charge	0.2 e
work functions	6 eV
temperature	77 K

4.2.3 Simulation B.

As mentioned earlier, the relaxation of electrons inside nanocrystals is very important for future applications of nanocrystals. Unlike ultrafast optical spectroscopy, STM-related measurements can't directly measure fast relaxation processes introduced by electron-electron interaction. Our picture of tunneling is composed of discrete energy levels and independent electrons. So STM-related measurement can be applied to investigate electron relaxation processes between discrete energy levels by emitting phonons. Here we study how the relaxation due to e-p interaction affects the tunneling I-V and BEES I-V.

In the previous chapter, $R_{\alpha\beta}$ in Eq. 63 is the relaxation rate from level β to level α. Assume we have two states i and j. j has one electron in level α and zero electrons in level β. i has zero electrons in level α and one electron in level β. The occupation of other levels is same for α and β . If the energy of level β is higher than that of levle α, then the nanocrystal can change from state j to i by one electron relaxing from level β to level α.

In the calculation, we apply some restriction to the relaxation. The energy level spacing is 0.1 eV. For real systems, this is very big for phonon energy. The relaxation processes due to e-p interaction between energy levels which have energy difference larger than 0.1 eV should seldom happen. We model the relaxation rates in the following way.

$$R_{\alpha\beta} = R_0 \exp\left[-\frac{\Delta E - \Delta E_0}{\Delta E_0}\right] \tag{88}$$

Where ΔE_0 is the energy level spacing, 0.1 eV here. R_0 is an input constant. ΔE is the energy spacing between level β and α. According to this equation, the relaxation rate decreases exponentially with the energy difference. So the relaxation is "neighboring relaxation".

Table 10 lists the parameters used in the simulation. The result is shown in Figs. 45 and 46. Figure 45(a) shows four I-V curves. The black one doesn't take into account relaxation. The red and the blue one use Eq. 88. the R_0 for the blue curve is 5 times of the R_0 for the red one. For the green curve, the relaxation rates $R_{\alpha\beta}$ is fixed to the same value of R_0 as for the red one, for any possible pairs of α and β. The interesting thing is that at low bias voltage, the tunneling current with relaxation is larger than the tunneling current without relaxation. When the bias voltage is around 1.4 V, the black curve is larger than the other three. In Fig. 45(b), the numerical dI/dV curves are plotted. The black curve without relaxation has two suppressed peaks. These two peaks come back when there is relaxation. The stronger the relaxation rate, the higher the peaks.

The calculated BEES I-V curves are plotted in Fig. 46. Relaxation increases the BEES current throughtout the whole voltage range.

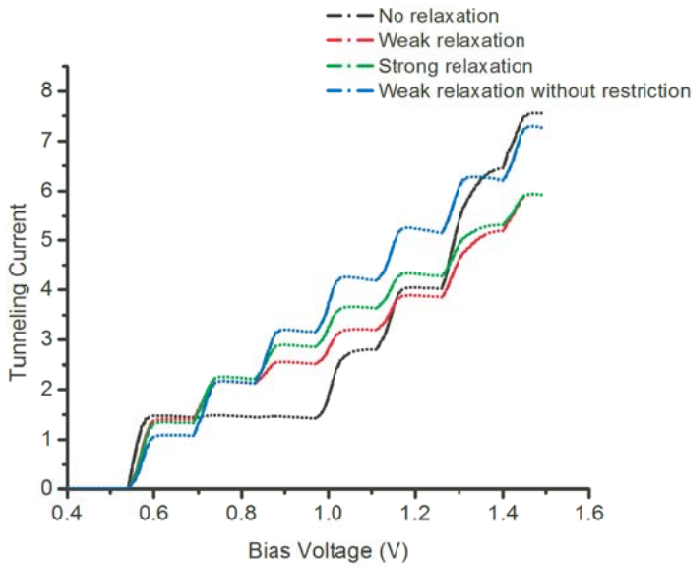

(a)

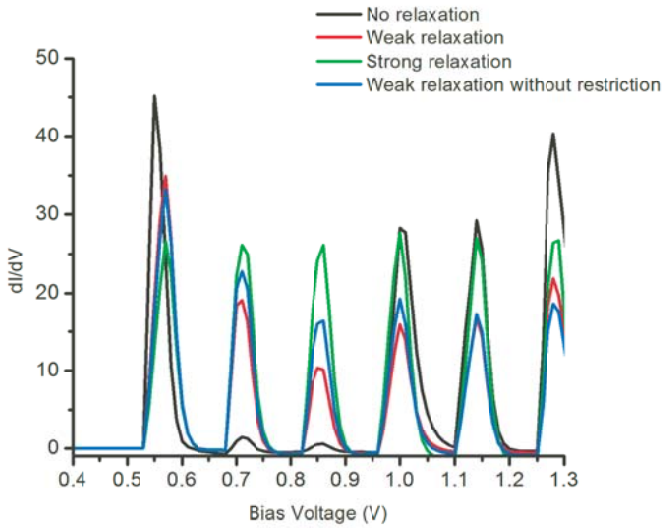

(b)

Figure 45: (a) Tunneling currents simulated using the parameters in Table 10. There is no relaxation for the black curve. For the red and the blue curves, the relaxation is restricted to "neighboring levels" as mentioned in the text. The rate is weaker for the red than for the blue. For the green curve, the relaxation has no restriction. The rates are same for all level pairs (no exponential weighting). (b) The numerical dI/dV curves calculated from (a). The suppressed peaks of the black curve come back in the curves which have relaxation.

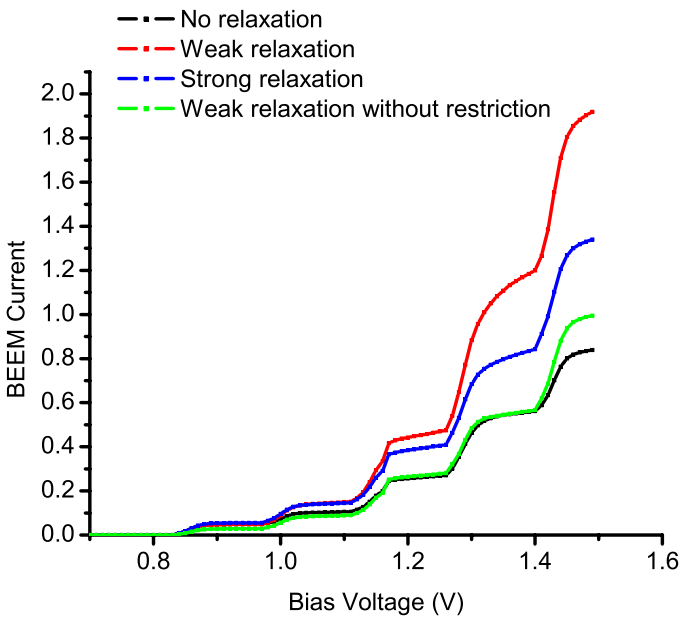

Figure 46: BEES current versus voltage curves simulated using parameters in Table 10. The black curve is without any relaxation. The relaxation for the red and the blue curves is restricted to "neighboring levels". The relaxation for the green one is not restricted to neighboring levels.

CHAPTER V

STM AND BEEM INSTRUMENTATION AND EXPERIMENT PREPARATION

5.1 UHV and Low-temperature STM System

The scanning tunneling microscope (STM) system we use is home-made [35]. Figure 47 illustrates the configuration of the STM and the vacuum system. The vacuum system is equipped with a Low Energy Electron Diffraction (LEED) system, a sputtering gun, and two tungsten-filament heaters. These additional capabilities enable basic sample treatment and surface analysis. Metal films can be sputtered and annealed. Surface lattice structure can be analyzed by the LEED system.

The whole vacuum chamber can be pumped by a turbo molecule pump and an ion pump. Ultrahigh vacuum of (2×10^{-10} Torr) can be achieved by baking the system at 150^oC for 24 hours. After the baking, the stainless walls are de-gassed very well. The ion pump can pump the chamber down to $1 \sim 2 \times 10^{-10}$ Torr. Ultrahigh vacuum is essential for surface experiments to prevent surface contamination. For our vacuum, sample surfaces can kept clean more than 10 hours. This provides the necessary time for observing the clean surface, especially with atomic resolution. In order to keep this ultrahigh vacuum, each sample is first loaded into a separate load-lock area. Then the load-lock area will be pumped for more than 2 hours by the turbo pump. When the vacuum inside the load-lock is in the mid-of 10^{-7} Torr range, the gate valve between the load-lock and the main chamber is opened and the sample is loaded into the main chamber. A sublimation pump runs once a day to more effectively pump hydrogen.

The bottom portion of the UHV chamber where the STM locates, can be immersed in a dewar filled with liquid nitrogen or liquid helium. So experiments can be performed at 77 K (liquid nitrogen) or 4 K (liquid helium). Approximately 36 hours is required for the

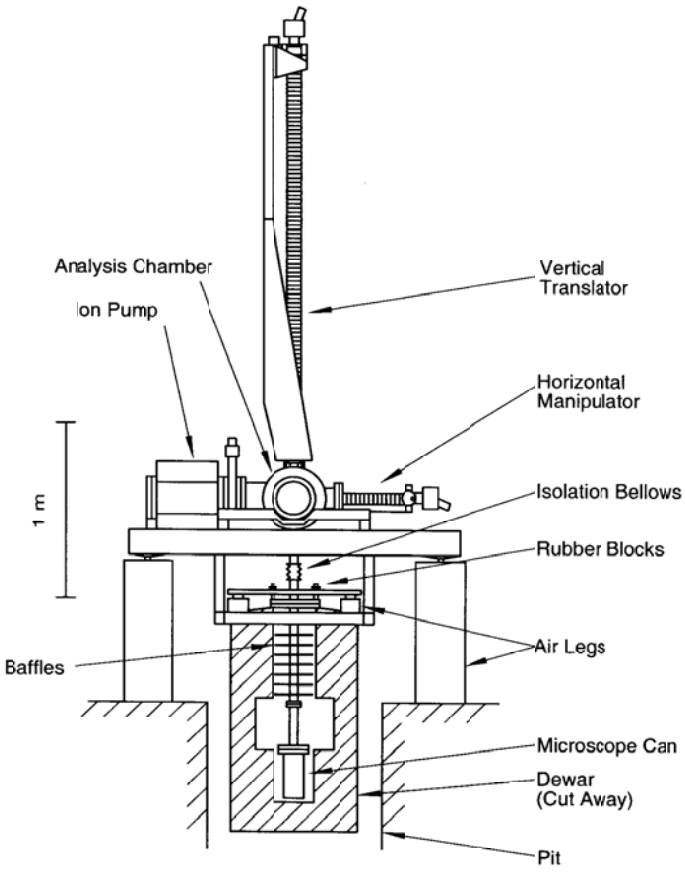

Figure 47: The whole structure of the home-made ultra high vacuum and low temperature scanning tunneling microscope system [36].

STM to cool to 77 K, but a new sample will reach a stable temperature (as judge by a low-drifting rate) within 12 hours. In order to isolate the STM from the vibration due to boiling of the cryogen, an exchange gas can covers the the bottom part of the STM. The exchange gas can is pumped down to a few milli torr in order to provide acoustic isolation. A few torr of helium gas is introduced to the exchange gas can in order to provide some thermal transport.

The core part of the STM is composed of piezo electric tubes as described by Harrel [35]. One center piezo tube is used to control the distance between the tip and the sample surface. Three outside piezo tubes are used to control the lateral motion between the tip and the sample. The outside wall of each tube has a silver coating. The surface is divided evenly into four electrically isolated quadrants by cuts along the tube axis. The inside wall also has a silver coating, which is continuous. A grounding wire is connected to it. If a voltage difference is applied across the tube wall, the length of that side will change. When opposite voltages are applied to opposite sides of the outer walls while the inner wall is grounded, then the tube will bend along that direction because the wall at one side becomes longer and the wall at the other side becomes shorter. If all outer walls have the same bias voltage, the tube will change its length instead of bending along some directions. For our STM, the center piezo supports the sample and is used to control the distance between the tip and the sample surface. So the voltages applied to the outer walls are same. For the other three tubes supporting the tip, opposite voltages are applied to opposite outside walls to make scanning laterally along the surface possible.

For the center piezo tube, the rate of length change with applied voltage is 24.42 Å per volt. For the outside three piezo tubes, the lateral rate is 163.06 Å per volt. Offset and scanning voltages are supplied by a 12-bit digital-to-analog conversion (DAC) board, so the distance between the tip and the surface can be controlled down to 0.0074 Å. The lateral position can be controlled within 0.045 Å. These calibrations are for room temperature. Good control of position is a key to atomic-resolution STM.

For imaging surface morphology, the STM operates in "constant current" mode. When the three outside tubes move the tip laterally, the center piezo tube automatically adjusts

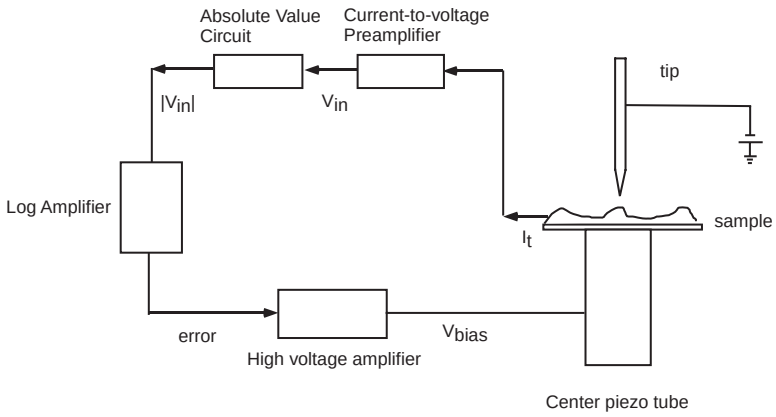

Figure 48: The feedback circuit for the center piezo tube.

the distance between the tip and the sample surface to keep the tunneling current constant. Figure 48 shows the basic servo control circuit for the center piezo tube. The tunneling current is used as the feedback to the servo. The tunneling current is first converted to voltage and amplified by a pre-amplifier. The model of this preamplifier is Ithaco 1211 Current Preamplifier from DL Instruments [6]. The absolute value is then fed into a log amplifier. This V_{in} is compared with a reference signal $V_{ref} = 1\,V$. The log amplifier output is:

$$V_{err} = -A \log_{10}(\frac{V_{in}}{V_{ref}}) \tag{89}$$

Here A is the gain of the log amplifier. For illustration purpose, we assume the tunneling current is proportional to $e^{-2\kappa d(x)}$. Then $V_{in}(s)$ is:

$$V_{in}(x) = Ce^{-2\kappa d(x)} \tag{90}$$

We define d_0 as:

$$V_{ref} = Ce^{-2\kappa d_0} \tag{91}$$

Insert above two equations into Eq. 89, we have:

$$V_{err}(x) = 2\kappa A(d(x) - d_0) \log_{10} e \tag{92}$$

This $V_{err}(x)$ is linear to the difference between instantaneous $d(x)$ and reference distance d_0. This signal is amplified and transferred to a voltage signal V_z which is applied to the

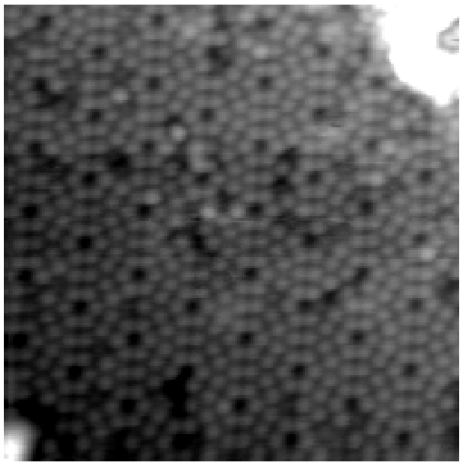

Figure 49: STM of reconstructed Si(111) surface at room temperature. The image size is 200 Å x 200 Å.

center piezo tube.

$$V_z = 2AG\kappa[d(x) - d_0]\log_{10} e \tag{93}$$

Here G is the gain of the output stage. In our case G is positive. When $d(x)$ is bigger than d_0, a positive V_z is applied to the center piezo tube. The extension of the center piezo will reduce $d(x)$. So the total circuit is a feedback circuit which keeps $d(x)$ close to d_0.

Figure 49 is an atomic resolution image of the silicon (111) 7×7 surface reconstruction. This image indicates that our home-made system is capable of atomic imaging.

The spectroscopy current versus voltage curve is measured while temporarily disabling the servo feedback, so that the tip remains at a distance from the surface. Then the computer changes the voltage applied to the tip in small steps. At each step, the corresponding current is measured and recorded. From the current versus tip voltage measurements, the I-V curve is obtained. The dI/dV curve can be found by numerical differentiation of the I-V curve.

The dI/dV curve can also be measured using a lock-in amplifier directly. An AC signal $V_{in}(\omega)$ with frequency $\frac{\omega}{2\pi}$ higher than the servo response frequency is summed with the DC tip bias voltage V_d. The total voltage V is applied to the tip. The detected tunneling

current I has both AC and DC components.

$$I = I_d + I(\omega) \tag{94}$$

If $V_{in}(\omega)$ is very small, we would expect the following relation.

$$I(V_d + V_{in}(\omega)) = I(V_d) + \left.\frac{\partial I}{\partial V}\right|_{V_d} V_{in}(\omega) \tag{95}$$

Comparing the above two equations, we have

$$I(V_d) = I_d \tag{96}$$

$$I(\omega) = \left.\frac{\partial I}{\partial V}\right|_{V_d} V_{in}(\omega) \tag{97}$$

So the amplitude ratio of $I(\omega)$ and $V_{in}(\omega)$ is just $\frac{\partial I}{\partial V}|_{V=V_d}$.

Experimentally the ratio is measured by a lock-in amplifier. The tunneling current is amplified by a current-to-voltage amplifier. This voltage signal is fed into the input of the lock-in amplifier. The output $I(\omega)(V_{in}(\omega))$ remains constant and is recorded by the computer. In order to get a dI/dV curve, the computer changes the DC bias voltage in small steps. Within the interval between steps, the $I(\omega)$ is determined. Therefore the derivative of $I(V)$ at different V is measured.

5.2 BEEM Setup

The Ballistic Electron Emission Microscope (BEEM) is implemented by modifying the sample holder in order to make two contacts (base and collector) for the sample. The original sample holder stage was one piece of stainless steel allowing a single electrical contact to the sample. The design implemented here has split the holder into two electrically-isolated pieces. Each piece has wire connected to the outside. One of them is used for the tunneling current. The other is used for the BEEM current.

The sample platens to which BEEM samples attach are specially designed. A stainless steel disk is split into two pieces ($\frac{3}{4}$-circle and $\frac{1}{4}$-circle sectors). They are glued together by insulating Epoxy [7] as shown in Fig. 51. One side is for BEEM current and the other is for tunneling current. When the sample platen is sitting on the sample holder, each piece of

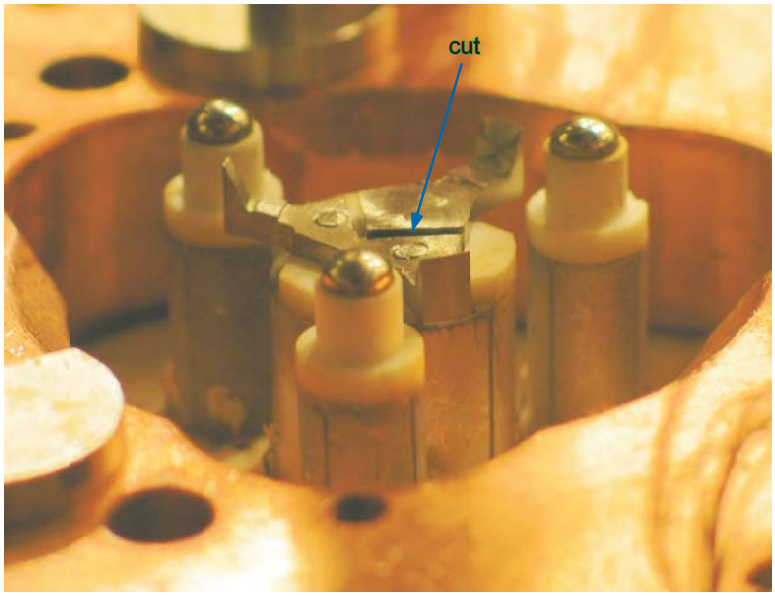

Figure 50: The sample stage. The cut is used to divide the whole sample stage into two parts electrically isolated from one another. One part is for the tunneling current and the other is for the BEEM current.

the platen touches the corresponding part of the sample holder in Fig. 50. The connection to the front side gold surface of BEEM samples (the base contact) is made by a rotatable clip. The clip is attached to one part of the BEEM sample holder by a screw. The second connection, for the BEEM collector current, is made by the contact between the back of the silicon wafer and the $\frac{3}{4}$-sector of the sample holder. The back of the silicon wafer is scratched by a diamond scribe and fresh indium is scraped onto it. This forms a good Ohmic contact between the silicon and the indium. Then the indium directly touches the sample platen. A BEEM sample mounted on its platen is shown in Fig. 51

In this work we performed two types of BEEM measurement: constant current mode and constant separation mode. In constant current mode, the tunneling current is kept constant by the STM servo. This mode is used for both BEEM imaging and BEEM spectroscopy. The constant separation mode is only for BEEM spectroscopy. While sweeping the tip bias voltage, the servo feedback control is disabled temporarily. So the tip is held at a fixed distance from the sample surface when the spectrum is being recorded. This constant separation mode eliminates current dependence on the separation and the physical processes

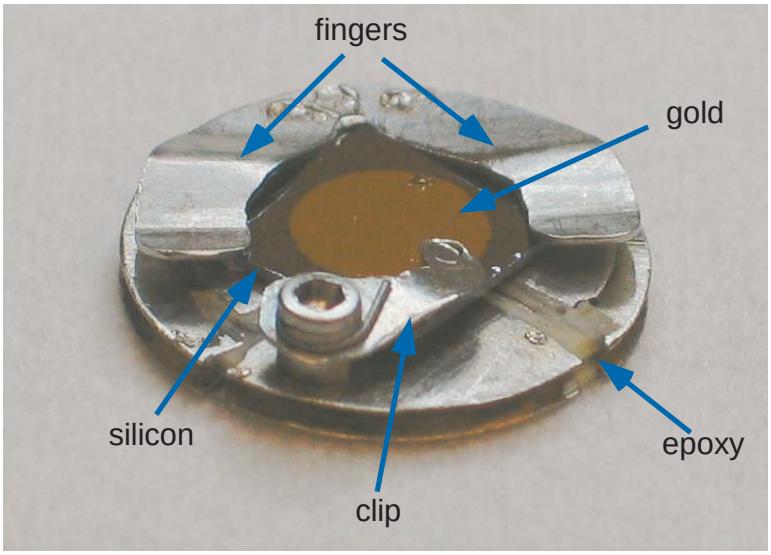

Figure 51: The BEEM sample platen. Two fingers are used to hold the sample solidly to the surface.

can be more easily modeled.

There are two stages for the BEEM current amplification. The first stage is a SR570 current amplifier from Stanford Research System [5]. The gain is typically set to 500 pA/V. The second stage is a voltage amplifier (Stanford Research System SR560 [5]). The typical gain is set to 20. The tunneling set current for both BEEM modes is generally 1 nA. Since the BEEM current is usually one percent of the tunneling current, the typical BEEM current is about 10∼20 pA in our measurement if the tunneling current is set to 1 nA . Such a small current has to be averaged over a long time in order to reduce noise. In acquiring a BEEM spectrum, the current at one tip bias usually is sampled by 40,000 times. At the same time, two amplifiers for the BEEM current are set in low-pass mode, with a cut-off frequency of 1 Hz.

5.3 Tip Preparation

Several types of tip are used for STM imaging. The most simple tip is mechanically cut Pt/Ir tip. A Pt/Ir (80% Pt and 20% Ir) wire with diameter of 0.01 inch from Wilkinson [9] is cut by scissor. This type of tip works well for relatively flat surfaces. The advantage of a Pt/Ir tip is that it is not easily oxidized. Once the tip is prepared, it doesn't need special

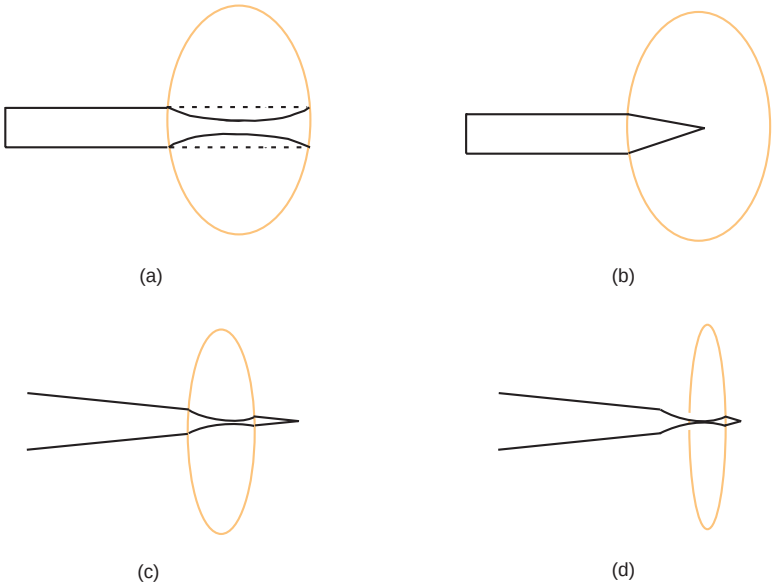

Figure 52: Etching tungsten tip using 1M KOH solution.

treatment inside the UHV chamber. The disadvantage is that this type of tip may have multiple asperities at the end. Consequently different parts of the tip can contribute to the tunneling current. This produces "ghost images" particularly on rough surfaces.

Most frequently used tips are made from tungsten. A thin tungsten wire with 0.075 mm diameter is spot-welded to a 1mm-diameter tungsten shank. The tip wire is etched in $1M$ KOH solution. The thin wire is first etched in a large drop of KOH solution as shown apparently to scale in Fig. 52. The tungsten will be etched away faster at the middle of the drop as shown in Fig. 52(a). The wire ultimately will break at the middle as shown in Fig. 52(b). Then the narrow end is etched by a smaller drop of KOH as shown in Fig. 52(c). Once the neck is thin enough, the KOH drop is moved to the other end as shown in Fig. 52(d). The right-side protrusion in (d) should be etched as small as possible but still leaving a neck. The final step is etching through or breaking the neck while moving the drop from left to right. The etching should be ended immediately after the neck is broken. The wire is observed by an optical microscopy. After etching, the tip is rinsed well using de-ionized water, followed by ethanol. Tips made by this method usually have a radius of 20$\sim$30 nm at the end. Figure 53 shows an SEM image of an etched W tip.

Tungsten is easily oxidized in air. So W tips were loaded into the UHV chamber as soon

Figure 53: SEM images of etched W tip.

as possible. Inside the chamber, W tips were heated in order to remove the oxide layer. The heating is made by electron bombardment. A W filament is brought close to the tip via a linear motion feedthrough. Electron bombardment is done by running 3∼4 A current through the filament, which is biased at -1,000 V relative to the tip. Electrons thermally emitted by the filament will hit the tip with high kinetic energy. This bombardment provides an efficient way to heat tips.

Gold tips are also made by etching. The solution used was a 50:50 mixture of hydrochloric acid and ethanol. The basic setup is shown in Fig. 54. The voltage used for gold tip etching is 1.8 V DC. The value of the bias voltage should be properly chosen. If the voltage is too large, Cl gas evolves. Etching at too large voltage results in a rough tip.

5.4 STM Sample Preparation

Two types of samples were made: one for tunneling spectroscopy, and the other for BEES and STS. The first type used mica as an atomically-flat substrate. A 130 nm layer of gold was deposited onto the mica substrate. The mica substrates were cut into small triangular pieces and cleaved mechanically. Then 5 pieces were placed onto a small metal fixture and secured using a metal ring. The fixture was loaded into the evaporation chamber. Once the

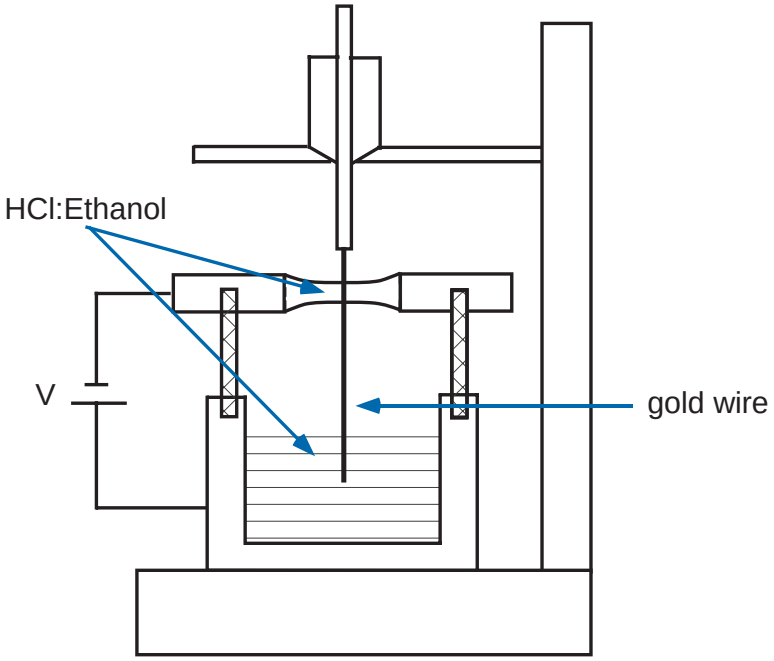

Figure 54: Setup for gold tip etching [8].

vacuum was in the 10^{-6} Torr range, the bottom of the metal fixture was heated by electron bombardment. The temperature of the metal fixture was measured by a thermocouple. Usually the mica pieces would be degassed for several hours at 360^oC. After mica was well degassed and the pressure went down to 10^{-7} Torr, a gold wire wound around a V-shaped tungsten filament was heated by adjusting the current through the filament. After melting, the gold formed a liquid drop in the "V" of the filament and evaporation proceeded at somewhat higher filament current. Once the evaporation rate stabilized at 0.5 Å/sec measured by a quartz monitor, the deposition started. The surface temperature of the metal fixture was kept around 450^oC during the evaporation. This high temperature enhanced the diffusion of gold atoms so that they could find the minimum energy sites and formed a high quality (111)-oriented gold film. After the deposition finished, the gold film on mica was annealed for half an hour at 400^oC.

After gold films were taken out of the evaporation chamber, they were spot-welded onto the surface of molybdenum sample holders using tantalum strips. Then the sample holder with gold film on mica was loaded into the UHV chamber. In UHV chamber, the surface of

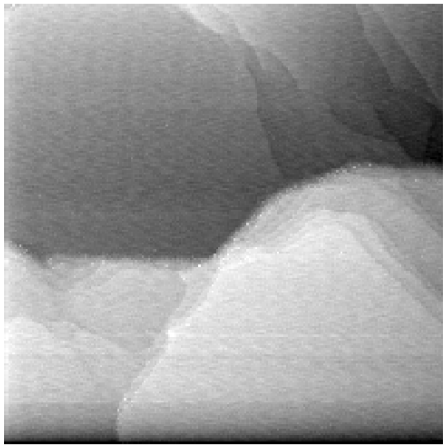

Figure 55: Gold film on mica. The dimension is 400 nm×400 nm.

the gold films were sputtered by neon at 6.2×10^{-5} Torr (measured on the iongauge with no correction for sensitivity). Samples were sputtered for 10 minutes with an emission current of 20 mA. After sputtering, gold films were annealed at 400^oC for 15∼20 minutes. Figure 55 is the STM image of a gold film which had been prepared in the same manner described.

When the distance between the STM tip and the nanocrystal is within the tunneling range, there can be a very strong interaction between the tip and the nanocrystal. One kind interaction is the Coulomb force between the nanocrystal and the the tip when the nanocrystal is charged. In experiments a finite tip voltage is applied to the tip. Since the distance between the tip and the substrate is of nanometer scale, the electrical field is very strong. when the nanocrystal is charged by tunneling electrons, it may experience a very strong repulsion force from the tip. Another kind interaction is between the the tip and the capping molecules of the nanocrystal. Usually the capping layer (ligand layer) is assumed to be a simple insulating layer, which only create a tunnel barrier. Tunneling occurs directly between the nanocrystal and the tip. Tunneling current decays exponentially with the distance between the nanocrystal and the tip. In the constant current mode, if the tunneling current is set at a relative large value, the tip could penetrate into the capping layer in order to achieve the required tunneling current. Penetrating of the capping layer

could result in an adhesive interaction, which may cause the tip to move nanocrystals on the surface, instead of imaging them.

In order to fix nanocrystals to a flat gold surface, the surface has to be modified. One successful approach was shown to be the growth of a self-assembled monolayer (SAM) of organic molecules [18, 19]. Usually the SAM consists of thiolate molecules, which at least one end terminates with a sulfur atom. The sulfur atom can form bond with gold atom of the substrate. The other end of the molecule should bind to the nanocrystal itself or to the capping molecules of the nanocrystal. Xylenedithiol molecules with two sulfur groups were used for all gold nanocrystals. For semiconductor nanocrystals, different molecules are used for different capping agents. The growth of the self-assembled monolayer will be discussed in the next chapter.

After a proper SAM layer is grown, nanocrystals were added to the surface. This procedure will be discussed in detail in the next chapter. Those nanocrystals which not bound to the SAM were rinsed away using the SAM solvent. Once the sample surface was clean and dry, the sample was loaded into the vacuum for experiments.

5.5 BEEM Sample Preparation

Silicon wafers with (111) orientation were bought from Silicon, Inc. [10]. The doping level is low, in order to form a good Schottky barrier between gold and silicon. The resistivity of the wafer is 1∼5 Ohms-cm. In order to reduce the surface roughness coming from wafer processing, the native oxide layer of silicon wafer was etched away by brief dip in dilute HF solution. Before the HF dip, the silicon wafer was cleaned by standard wafer cleaning processes to remove organic and metal contamination on the surface [11]. After dipping, the wafer was load into a dry oxide furnace. A uniform and high quality SiO_2 of 8 nm thickness (this part is done in Georgia Tech MiRC by staffs there) was grown. Subsequently the wafer was diced into 0.76 mm×0.76 mm square pieces.

The Schottky barrier was formed by depositing gold onto the Si(111) surface. Before the deposition, each piece was cleaned successively with trichloroethylene, acetone, and ethanol. Beakers for each solvent were put into an ultrasonic bath for 4 minutes. Then

Si pieces were then dipped for 150 seconds in an HF:ethanol solution with volume ratio of 1:10. The Si surfaces which resulted were hydrogen terminated [58], which protects the silicon surface from oxidation. Etched silicon pieces were rinsed thoroughly with water to remove any residual HF. After blowing dry with nitrogen, silicon substrates were assembled into a specially designed holder with a deposition mask, and loaded into e-beam evaporator (inside Georgia Tech MiRC cleanroom) as soon as possible. The masks were 5mm-diameter holes over the center of each substrate.

The Gold evaporation was done with the pressure in the range of 10^{-7} Torr, at a rate of 2 Å/sec. Diffusion of Si atoms to the surface of golf film was often a problem, as judged from STM images. Si oxides at the surface, creating non-conductance region which can damage the STM tip. In order to remove the SiO_2 "boulders", the samples were dipped in HF:ethanol (10 seconds) before further processing. Most of the Si out-diffusion appeared to take place during Au deposition. The deposition rate used can produced gold grains with sizes of 15$\sim$20 nm. After the HF dip, samples were immersed into deionized water and then ethanol. The use of water is to remove any HF. The Ethanol is used to remove water from the surface and let the sample dry more quickly.

Figure 56 is a current versus voltage curve for a BEEM sample. Figure 57 shows an STM image of a Au/Si sample surface without any organic molecules or nanocrystals.

Once the Au/Si Schottky barrier was ready, a SAM layer and nanocrystals were deposited onto the gold, as for STM samples. Before mounting onto the BEEM sample holder, a good Ohmic contact was made on the back of the silicon wafer. A simple method was applied to get a fine Ohmic contact. First the back of the silicon wafer was scratched by a diamond scribe. This produces many defects at the surface. Fresh indium is then rubbed onto the scratched surface. The defects produce states which have energies in the energy gap of silicon, creating an Ohmic contact. Finally, the BEEM samples were mounted onto the BEEM platen and loaded into the UHV chamber.

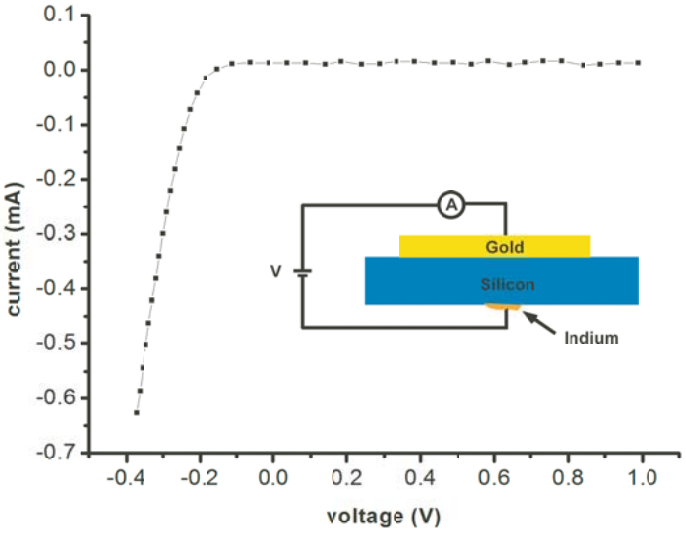

Figure 56: Schottky current versus voltage curve of a BEEM sample at room temperature.

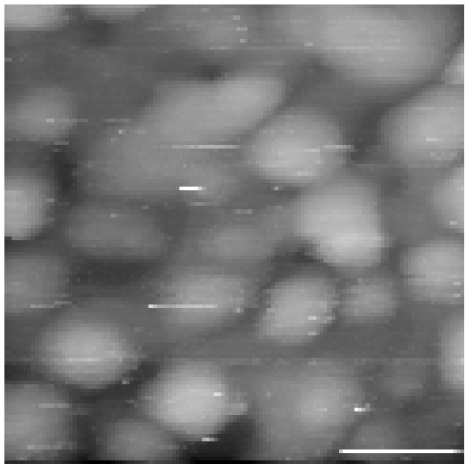

Figure 57: STM image of a BEEM sample surface without any organic molecules and nanocrystals at 77 K. The size is 80 nm×80 nm. The set current is 100 pA. The bias voltage is -1 V.

CHAPTER VI

EXPERIMENTAL RESULTS AND ANALYSIS

6.1 STM Imaging of Gold Nanocrystals

This section we investigate several kinds of gold nanocrystals. Gold nanocrystals of 22 kDa (1 kDa=1.66×10^{-24} kg), 28 kDa, 65 kDa, and 100 kDa were imaged using our STM [2]. The 22 kDa, 28 kDa, and 65 kDa Au nanocrystals are capped with benzenethiol [50]. The 100 kDa nanocrystals are capped with dodecanthiol. For all of these systems, the SAM layers were 1,4-benzenedimethanethiol molecules (xylenedithiol). All the gold nanocrystals are dissolved in toluene.

The growth and the treatment of the gold films was described in the previous chapter. Once the gold film was taken out of the vacuum, it was immediately immersed into solution of organic molecules. The organic solution used was xylenedithiol in Tetrahydrofuran (THF). Xylenedithiol has two sulfur groups. When the Au(111) surface is immersed in the xylenedithiol solution, the molecules self-assemble into a monolayer (SAM) with one sulfur atom bound to the gold surface and the other sulfur group sticking out from the surface. Usually after 24 hours, a very dense SAM can be formed on Au(111) surface. When Au nanocrystals were deposited from solution in toluene onto this surface, the free sulfur atom end of the SAM can penetrate the capping layer of Au nanocrystals and form another sulfur-gold bond. If several xylenedithiol molecules form bonds with a nanocrystal, then the nanocrystal could be fixed to one place solidly enough to survive interaction with the STM tip while scanning. It was found that a very dense SAM is not the best for fixing nanocrystals to the gold surface [18**?**]. Instead, experiments showed that a SAM layer formed when the Au(111) surface is immersed in the solution only for one hour is the optimal SAM for fixing nanocrystals. After the gold film was taken out of the SAM solution, it was rinsed very well using pure THF in order to remove any residual xylenedithiol molecules which were not bound to the gold surface. Usually it would take about 15 minutes for THF to

evaporate completely from the surface.

After the SAM was ready, the nanocrystal solution was added onto the surface. Depending on the concentration of the solution (typically 0.2 nM), several 1-μL drops of the solution were deposited on the surface. Toluene evaporates very fast. In order to let the nanocrystals have enough time to diffuse on the surface and be fixed by the SAM, the sample was covered by a beaker to reduce the evaporation rate. After the sample was dry, it was carefully rinsed by toluene. This remove unbound nanocrystals from the surface. Before the sample was loaded into the vacuum, it was allowed to dry for 10 minutes.

6.1.1 22 kDa Au Nanocrystals

Figure 58 shows an STM image of the Au 22 kDa nanocrystals at 77 K. The coverage was high enough that nanocrystals aggregated on the surface. The height profile of four nanocrystals are shown in Fig. 59. The average height is about 1.66 nm. The lateral sizes are much larger than the heights due to the convolution with the tip shape. Assuming gold nanocrystals are approximately spherical, the height measures the nanocrystal diameter more accurately than does the lateral size [19].

Another sample with lower coverage is shown in Fig. 60. Individual gold nanocrystals are resolved on the flat gold substrate in this room-temperature image. The white streaks in the image indicate that the nanocrystals were moved by the STM tip. The height analysis is consistent with the 77 k measurement in Fig. 59.

6.1.2 28 kDa Au Nanocrystals

An STM image of 28 kDa Au nanocrystals is shown in Fig. 61. Individual nanocrystals are resolved on the surface. Narrow white streaks again indicate that something on the surface was dragged by the tip. The analysis of the cross sectional profiles shows that the average height is about 1.2 nm. The lateral sizes of the nanocrystals in Fig. 61 have a broad range.

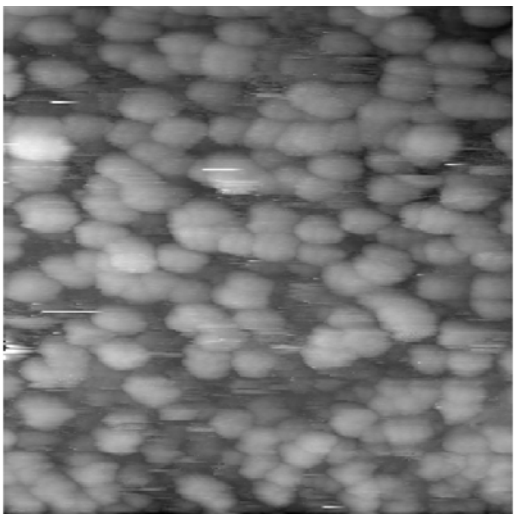

Figure 58: An STM image of Au 22 kDa nanocrystals at 77 K. The image size is 133 nm × 133 nm. The set point current is 100 pA. The tip bias is -1 V [2]

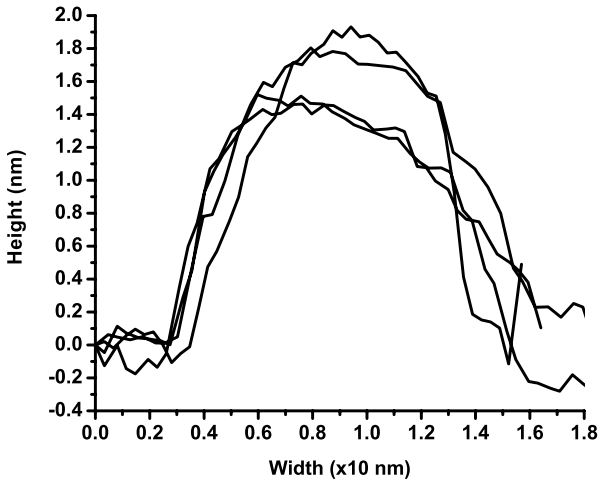

Figure 59: The cross sectional profiles of four nanocrystals in Fig. 58. The average height is about 1.7 nm.

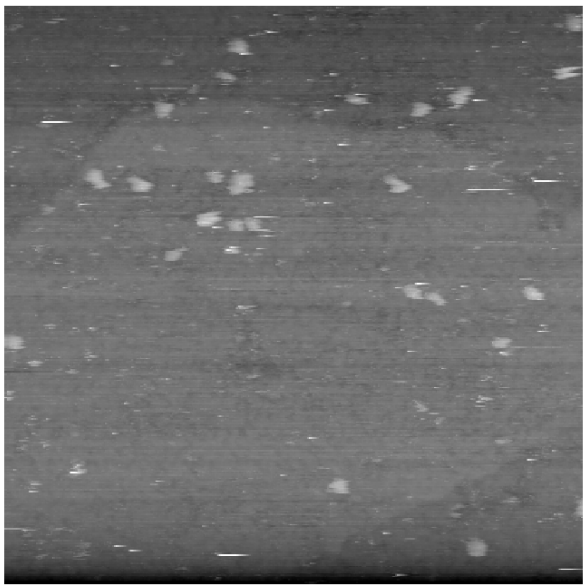

Figure 60: An STM image of Au 22 kDa nanocrystals at room temperature. The coverage was low so individual nanocrystals were resolved. The image size is 200 nm $\times$ 200nm. The set point current is 100 pA. The tip bias is -1V [2]

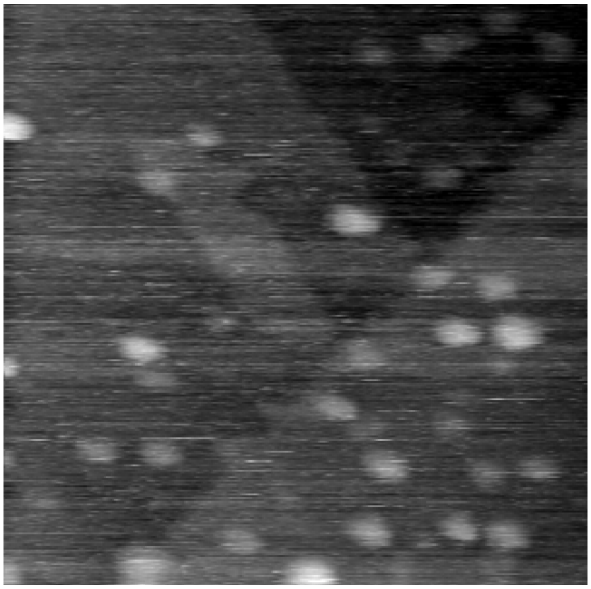

Figure 61: An STM image of 28 kDa Au nanocrystals at room temperature. The image size is 150 nm $\times$ 150 nm. The set point current is 100 pA. the tip bias is -1 V [2].

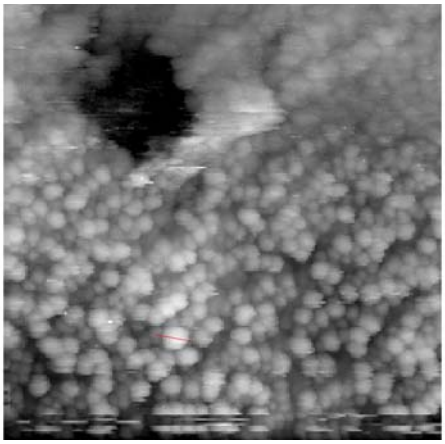

Figure 62: An STM image of 65 kDa Au nanocrystals at 77K. The coverage is high. Nanocrystals form layers [2].

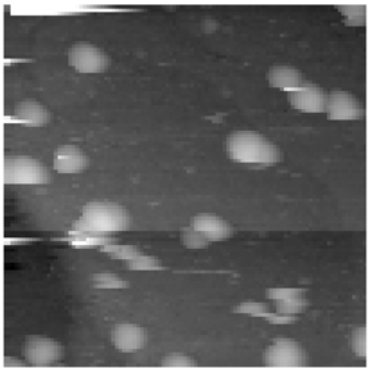

Figure 63: An STM image of 100 kDa Au nanocrystals capped with dodecanthiol at room temperature. The image size is 100 nm×100 nm. The set point current is 100 pA. The tip bias is -1 V [2].

6.1.3 Large Au Nanocrystals

An STM image of 65 kDa gold nanocrystals is shown in Fig. 62. The scanning was done at 77 K. The coverage was high so nanocrystals were piled together on the surface. The cross sectional profiles show that the mean height is about 2 nm.

Figure 63(a) resolves individual nanocrystals on the surface at room temperature. Some of them have nearly spherical shapes. Height analysis shows that the mean height is about 3.5 nm. In Fig. 64(a) are two well resolved nanocrystals; Fig. 64 (b) is a 3D construction of the nanocrystals in (a).

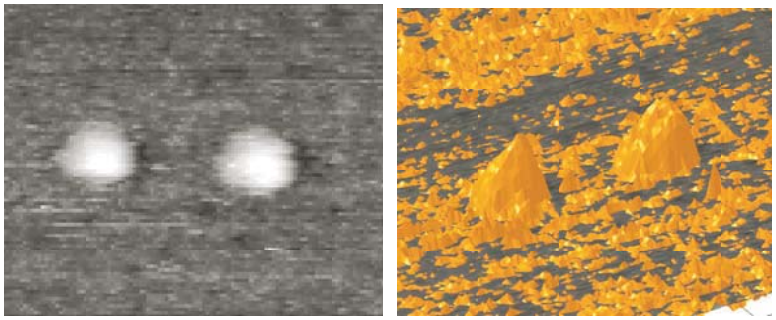

(a) (b)

Figure 64: (a) An STM image of two 100 kDa Au nanocrystals at room temperature. The image size is 100 nm × 100 nm. The set point current is 100 pA. The tip bias is -1 V. (b) The 3D construction of two nanocrystals shown in (a) [2]

6.2 STM Imaging of Semiconductor Nanocrystals

In this section, we show representative STM images for semiconductor nanocrystals of CdS and CdSe. To image CdS and CdSe nanocrystals is more challenging than to image gold nanocrystals. The bulk CdS and CdSe are wide band gap semiconductors. At the same time, quantum confinement induced energy band gaps are more significant than in gold nanocrystals. In order to inject electrons onto semiconductor nanocrystals, the tip bias has to be large. But a large tip bias voltage means strong electrostatic interaction between the tip and a nanocrystal. Therefore good SAM-nanocrystal bond is extremely important for STM experiments.

The CdS nanocrystals are capped with dodecanthiol. There are two types of CdSe nanocrystals. One of them is capped with trioctylphosphine oxide (TOPO). The other is capped with Mercaptan. For dodecanthiol capped CdS and TOPO capped CdSe, the SAM was formed of xylenedithiol. For the Mercaptan capped CdSe, The SAM was formed of 4-aminothiolphenol (4-ATP).

6.2.1 CdS Nanocrystals Capped with Dodecanthiol

The CdS nanocrystals imaged here were synthesized by Alex Schill in Profesor Mostafa El-Sayed's group at the Georgia Tech School of Chemistry. The CdS nanocrystals were produced using the colloidal technique [1]. These nanocrystals have a capping layer of dodecanethiol to prevent aggregation in toluene solvent. The substrate used was flat Au(111)

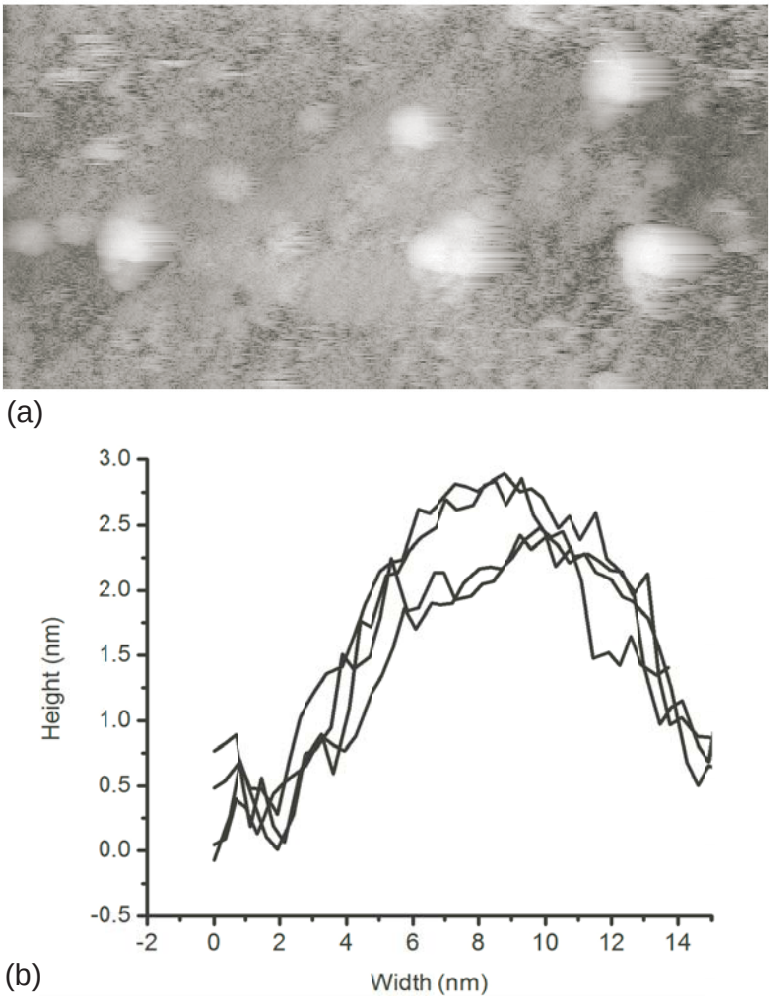

Figure 65: (a) An STM image of the CdS nanocrystals capped with dodecanthiol at 77 K. The image size is 133 nm × 66.7 nm. The set point current is 100 pA. The tip bias is -3 V.(b) The cross sectional profiles of several nanocrystals in (a) [1].

prepared as described in Chapter IV. We used the same xylenedithiol SAM as for the gold nanocrystals.

Bulk CdS has a band gap of 2.48 eV. Assuming the Fermi level of the CdS nanocrystal is aligned with the tip Fermi level at zero bias, the magnitude of the tip bias has to be well above 1 V in order to inject electrons into the conduction band of the nanocrystal. In order to ensure that there are always states for tunneling, the bias voltage magnitude should be close to 2.48 V.

Figure 65 is the STM image of the CdS nanocrystals at 77 K. (a) is the constant current image with 100 pA set point current and -3 V tip voltage. (b) is the cross sectional profiles of

several nanocrystals in (a). Large white regions in the image are nanocrystals. The shapes are not perfectly circular. The fuzzy edges indicate that the nanocrystals are moving back and forth under the tip. This movement means that the attachment of the nanocrystals to the surface is not strong enough to cancel the strong interaction between the tip and the nanocrystal. Figure 65(b) shows the cross sectional profiles of four nanocrystals. The average height is about 2 nm.

6.2.2 CdSe Capped with Trioctylphosphine Oxide (TOPO)

Here we study the CdSe nanocrystals capped with trioctylphosphine oxide (TOPO). The nanocrystals were prepared by Qusai Darugar in Professor Mostafa El-Sayed's group at the Georgia Tech School of Chemistry [3]. The nanocrystals were dissolved in toluene. Figure 66 shows the surface image of a CdSe nanocrystal sample at 77 K. The surface is not well resolved. White streaks indicate that something is moving on the surface. large white spots appear to be aggregation of nanocrystals. There are also many smaller features whose origins are uncertain. These features may derive from the solvents for the SAM layer and for the nanocrystals. The cross sectional profiles for the nanocrystals marked with "A" and "B" in Fig. 66(a) are shown in (b) and (c). One height is about 1.8 nm and the other is about 1.2 nm.

6.2.3 CdSe Nanocrystals Capped with Mercaptan

Here we study CdSe nanocrystals capped with mercaptan. Nanocrystals capped with mercaptan attract great interest because they can be dissolved in water. Consequently this type of nanocrystals is compatible with biological systems. In order to bind these CdSe nanocrystals to the gold substrates, 4-aminothiophenol (4-ATP) molecules were used to form the SAM layer. 4-ATP has one sulfur group and the molecule can be self-assembled into a dense monolayer on the Au(111) surface. The $[H_2N]^-$ group of 4-ATP can form a strong bond with the $[HS\text{-}C{=}O]^-$ group of the mercaptan on the nanocrystals. Therefore, the CdSe nanocrystals with mercaptan can be bound to gold substrates by 4-ATP SAM's.

Here we study this system at room temperature. Figure 67 shows an STM image of this type of sample. In part (a) four CdSe nanocrystals are resolved clearly. This indicates that

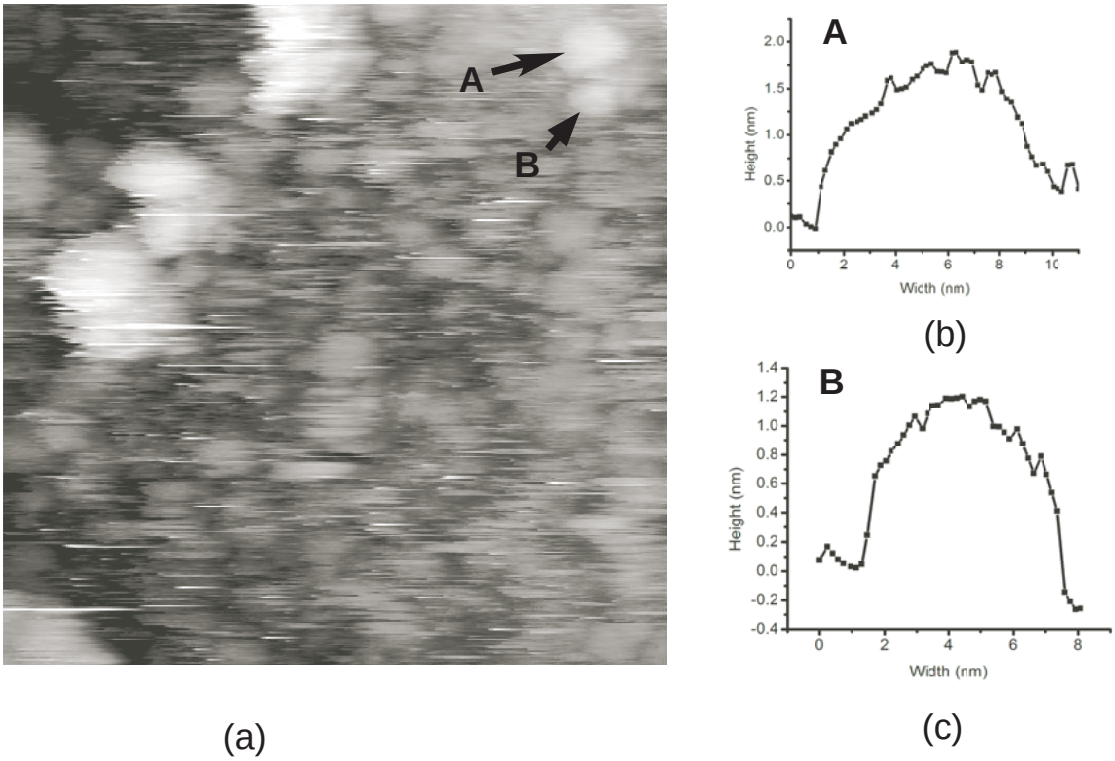

Figure 66: (a) An STM image of CdSe nanocrystals capped with TOPO at 77K. The set current is 100 pA and the tip bias is -2 V. Two nanocrystas are marked with "A" and "B". (b) The cross sectional profile of the nanocrystal marked with "A" in (a). (c) The cross sectional profile of the nanocrystal marked with "B" in (a) [3].

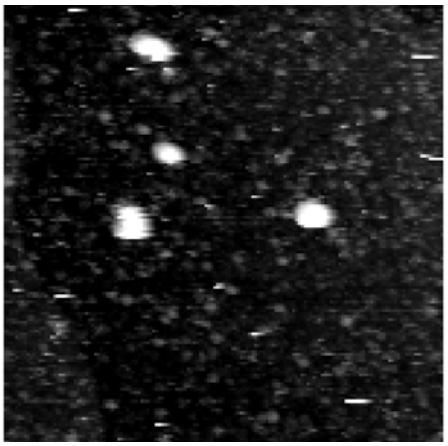

Figure 67: An STM image of CdSe nanocrystals capped with mercaptan at room temperature. The SAM is formed by 4-ATP. The image size is 50 nm×50 nm. The set point current is 100 pA. The tip bias is -2 V [3].

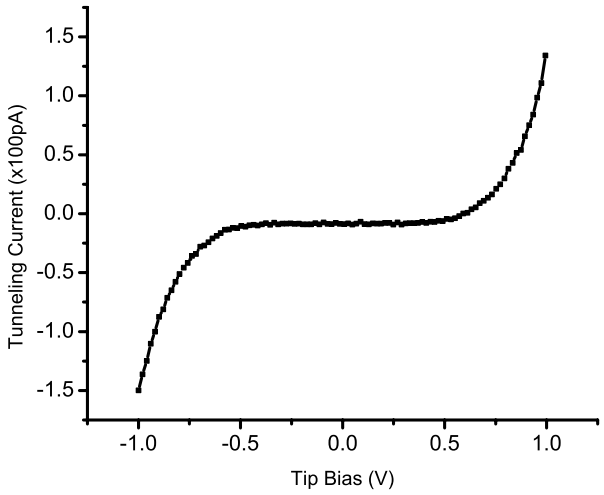

Figure 68: Tunneling current versus voltage curve of Au 100 kDa nanocrystals capped with dodecanthiol at 77 K. There is a Coulomb blockade gap about 1.0 V in the middle [2].

the binding mechanism mentioned above is practical. The cross sectional profiles are shown in (b). The average height is about 3.5 nm.

6.3 STM Spectroscopy of Gold Nanocrystals

In previous sections, we obtained STM images of several types of nanocrystals. In the constant current mode, the information we get is the size of nanocrystals. In order to investigate the nanocrystal electronic structure and the electrostatic coupling to the environment, we performed spectroscopic measurements on gold nanocrystals. There are at least two ways to do scanning tunneling spectroscopy (STS). The first is a current-versus-voltage measurement. While the tip is in tunneling range, the feedback mechanism of the STM system is disabled temporarily. The tip is be held at a fixed position above the surface. Then the tip bias is ramped through the interesting voltage range. The corresponding tunneling current is recorded. Figure 68 shows a current versus voltage curve of a Au 100 kDa nanocrystal capped with dodecanethiol acquired at 77 K. At the center of the spectrum (-0.5 V to 0.5 V), the tunneling current is zero. This voltage gap is due to Coulomb Blockade [16, 32].

The differential conductance dI/dV curve generally is related to the local density of

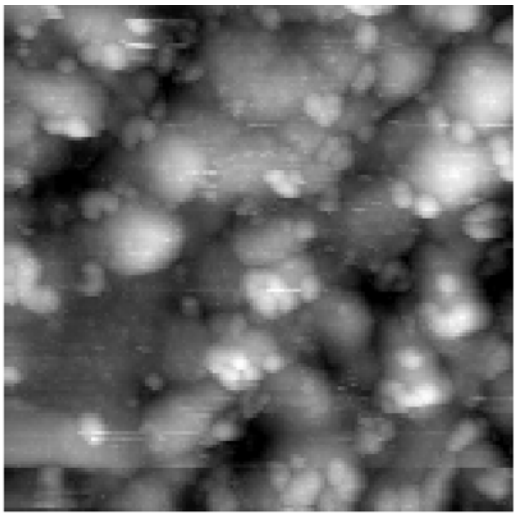

Figure 69: An STM image of 29 kDa Au nanocrystals on a BEEM sample substrate at 77 K. The image size is 125 nm×125 nm. The tip bias is -1.5 V. The set point current is 100 pA [2].

states. From the measured current-versus-voltage spectra, we can get the dI/dV curve by numerical differentiation. Another way to find the dI/dV versus voltage spectrum is to use a lock-in amplifier to directly measure the dI/dV versus V curve. The basic idea has been described in the previous chapter.

Figure 69 is an STM image of 29 kDa Au nanocrystals sample using a BEEM sample substrate (10 nm Au on Si(111)). For BEEM samples, the silicon substrate is not heated during or after gold deposition. This is because the heating will cause silicon atoms to diffuse into the gold film (oxidation of surface Si atoms ruins the tunneling since SiO_2 regions are not conducting). The small spots in Fig. 69 are the 29 kDa Au nanocrystals. Most of them sit at valleys between large gold grains.

Figure 70 shows dI/dV spectra measured using a lock-in amplifier. An AC voltage from the output port of the lock-in amplifier is summed with the DC bias voltage. The amplitude of this AC voltage is 50 mV and the frequency is 5 kHz. Two stages are used for the tunneling current. The gain of the first current-to-voltage amplifier is 10^7. The output of this amplifier is fed into the input of the lock-in amplifier and into a voltage amplifier. The lock-in amplifier detects the 5 kHz AC components, which is proportional to dI/dV at the DC bias voltage. The second voltage amplifier has a low-pass corner frequency of 1

kHz and a gain of 1,000. After this stage, the total gain for the tunneling current seen by the servo is 100 pA/V. The low-pass filter of the second amplifier reduces the amplitude of the AC component to negligible small value. At the same time, the servo can't respond to AC signal above ∼1.5 kHz, therefore the servo will not respond to the AC component of the bias voltage. It only responds to slower changes of the current, therefore the AC bias voltage will not affect STM imaging.

There is always stray capacitance between the tip and the sample. If an AC voltage is applied to the tip, there will be some AC current going through the system due to the capacitor coupling. This AC displacement current has a 90 degree phase-difference to the resistive AC current due to tunneling. If the phase is set correctly at the lock-in amplifier, the AC component due to the capacitance coupling can be reduced to a low value. In order to achieve this, the phase of the internal reference signal of the lock-in amplifier is adjusted to make the input signal is largest when the tip is retracted from the surface (pure capacitance coupling). Then the phase is increased by 90 degrees and the tip is release to tunneling range. In this way, the effect of capacitance coupling between the tip and surroundings can be reduced.

In Fig. 70, the red curve was measured when the DC tip bias voltage swept from -2.0 V to 2.0 V. The blue curve was measured when tip bias voltage swept from 2 V to -2 V. There are slight differences between these two curves. Both curves have a Coulomb blockade gap of 1.17 V. On the positive bias side, the red curve has three prominent peaks. The voltage spacings between them are 0.711 V and 0.258 V respectively. Actually the large spacing (0.711 V) is almost three times of the small one (0.258 V). This kind irregularity is similar to the calculated dI/dV curve with two peaks suppressed in Chapter III. The irregularity of the voltage spacings means that these peaks can't be simply assigned as charging peaks because pure charging peaks should be spaced evenly at one side.

Figure 71(b) are dI/dV curves measured with the lock-in amplifier for a 29 kDa Au nanocrystal. The nanocrystal is shown in (b), with dI/dV positions marked by numbers. The black and red curves were measured at the point marked by 1 in (b). The green and the blue curves were measured at the point marked by 2. (c) is the cross sectional profile

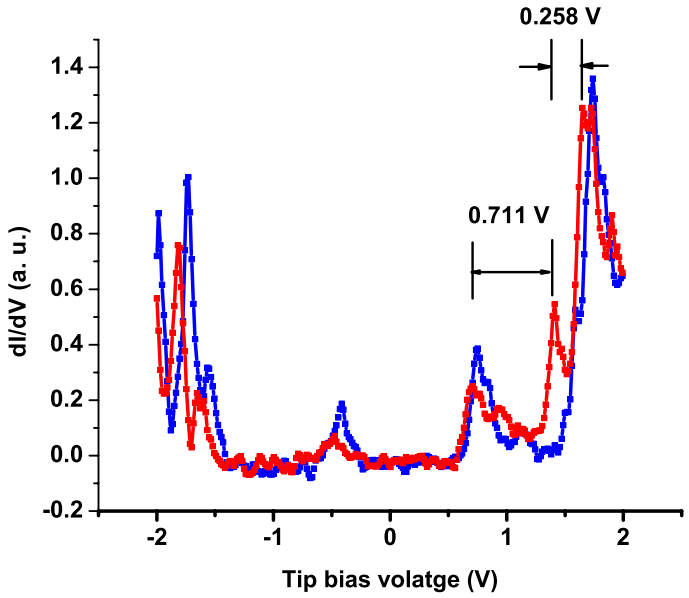

Figure 70: The dI/dV versus voltage curves measured directly using a lock-in amplifier at 77 K. The nanocrystals are 29 kDa Au nanocrystals capped with dodecanthiol. The set point current is 100 pA [2].

of the nanocrystal in (b).

6.4 BEEM Spectroscopy of Gold Nanocrystals

For BEEM measurements, two connections are made to the sample. One connection is for the normal tunneling current (the base current). The other is for the collector (BEEM) current. The amplification of the BEEM current uses two amplifiers. The first one is current-to-voltage amplifier, Stanford Research System SR570. The second is a voltage amplifier, Stanford Research System SR560. The gain for the first one was set for 500 pA/V, the second one used a gain of 20, producing a total gain of 25 pA/V. This means one volt detected by the computer corresponds to 25 pA BEEM current. Usually the BEEM current is of order 1% of the tunneling current. In our measurement, the set point current was usually 1 nA. So the BEEM current was in the range of 10 to 20 pA. There are several noise sources which can obscure such small current. In order to improve the signal-to-noise ratio, the BEEM current at each voltage bias point was averaged over several seconds.

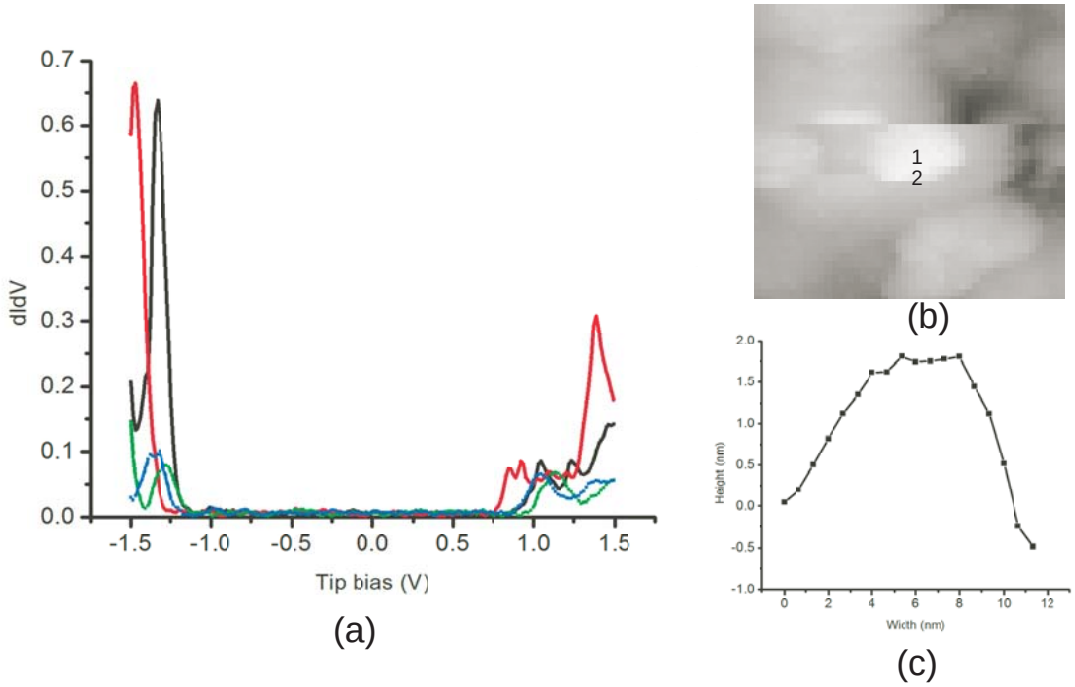

Figure 71: (a) The dI/dV versus V curves of 29 kDa Au nanocrystals capped with dodecanethiol acquired at 77 K. The red and the black curves were measured at point 1 in (b). The green and blue curves were measured at point 2. (b) The STM image of the sample surface. One nanocrystal is clearly resolved. The dI/dV curves were measured at points marked with 1 and 2. (c) The cross sectional profile of the nanocrystal marked with 1 and 2 in (b) [2].

BEEM sample preparation was described in the previous chapter. To recap, 13 nm gold film was deposited on an HF treated Si(111) surface. A SAM was grown on the gold surface and Au nanocrystals were deposited from solution. A connection to the gold surface collected the tunneling current. A connection on the back of the silicon collected the BEEM current.

Figure 72(a) shows an STM image of a BEEM sample acquired at 77 K. Several nanocrystals are resolved on the surface. The tip was moved to sit above the nanocrystal which is indicated by the arrow. The cross sectional profile of that nanocrystal is shown in (b). The spectroscopic data are shown in (c) and (d). The current-versus-voltage curve in (c) has a voltage gap of 1.5 V. An interesting feature about of the BEEM I-V is that the threshold voltage is shifted to 1.1 V (recall that the Au/Si Schottky threshold is about -0.8 V). This shifting should directly related to the big voltage gap in (c). From (c) we know that the charging energy is high. On the negative bias side, the tunneling current begins to increase from zero when the bias voltage is about -0.8 V. At -1.1 V, the tunneling current is still very small, although not zero. Because of all kinds of scattering, the electrons entering the silicon are few. This explains why the BEEM current is zero till the bias voltage is about -1.1 V.

In order to illustrate possible effects on the BEEM current due to nanocrystals, we compared the BEEM spectrum acquired over a gold nanocrystals with that measured over the SAM. Figure 73 (a) shows the surface of a BEEM sample. The coverage of the nanocrystals is so high, so a layer of nanocrystals were formed on the surface. A BEEM I-V was measured when the tip was near the center of the image. The measured curve is shown in red curve in Fig. **??**(b). Before nanocrystals were deposited onto the surface, we measured the BEEM I-V of of the same gold film with only a SAM on it. The measured BEEM I-V from the SAM is the blue curve in (b). The BEEM I-V acquired over nanocrystals increases much more slowly than the spectrum from the SAM. It also shows that the nanocrystal reduces the BEEM current magnitude, so energy relaxation must take place in the nanocrystal.

The above BEEM I-Vs were measured when the servo was operating and the tunneling current was kept at a constant value. Figure 74 shows the tunneling I-V and the BEEM

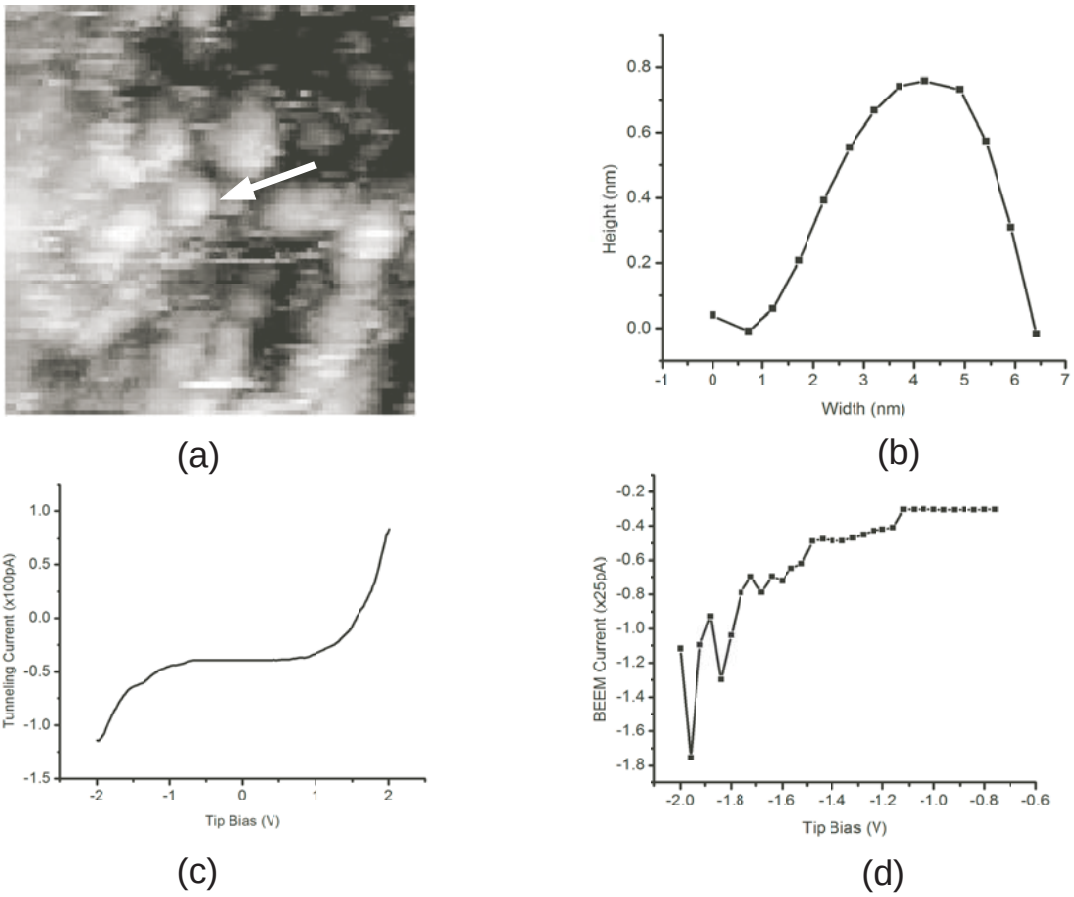

Figure 72: (a) The STM image of a BEEM sample surface. Spectroscopy measurements were done on the nanocrystal indicated by the arrow. (b) The cross sectional profile of the nanocrystal in (a). (c) The tunneling current verse voltage curve was measured when tip was sitting on the nanocrystals in (a). (d) The measured BEEM current versus voltage curve [2].

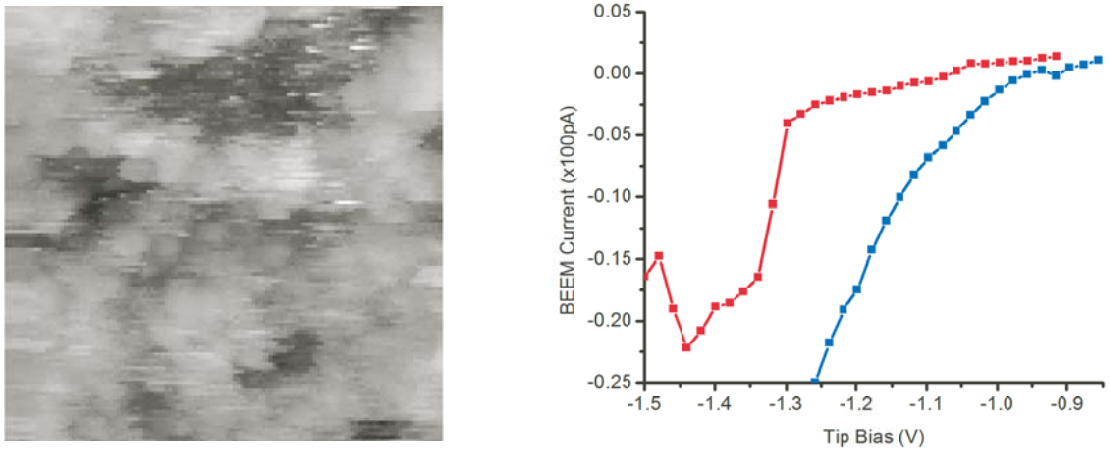

Figure 73: (a) The STM image of a BEEM sample with high nanocrystal coverage. Nanocrystals formed a layer on the surface. (a) Tunneling I-V was done when the tip was at the center of (a). (c). The red curve is the BEEM I-V measured at the center of (a). The blue curve was measured on the same BEEM sample before nanocrystals were put on to the SAM [2].

I-V acquired when the tip was held at a fixed distance from the surface.

In summary, we found the nanocrystals affect the BEEM I-V curves in two ways. The first is that the BEEM I-V curves over nanocrystals are less smooth that those on bare gold as shown in Fig. 72 and Fig. 73. These BEEM I-V curves have step like structures. This is consistent with our calculations. It is not surprise to see these kind step structures since the electron levels are discrete in the nanocrystals we used. The other effect is that the nanocrystals reduce the BEEM currents. This suggests that there are some energy relaxation processes inside the nanocrystal while tunneling.

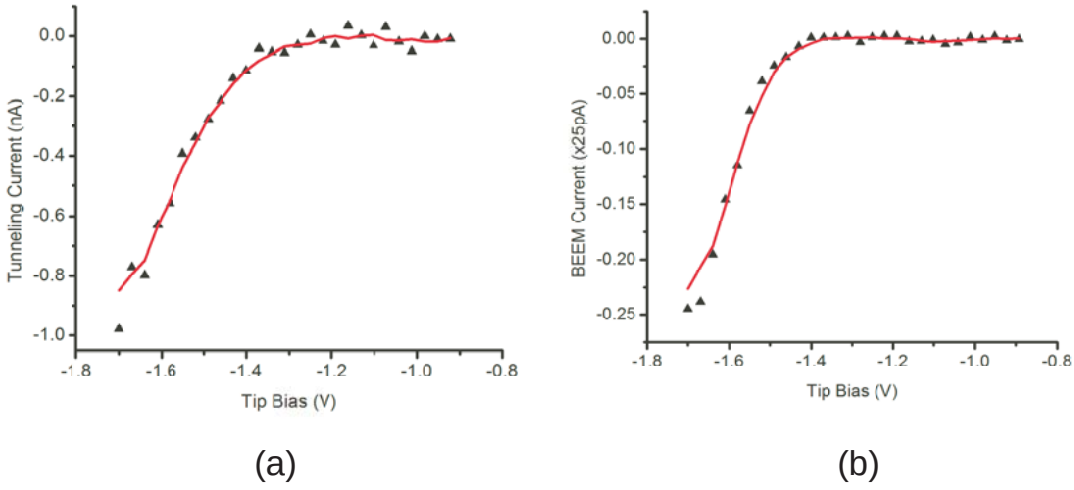

Figure 74: (a) The tunneling I-V measured on BEEM sample. (b) The simultaneously measured BEEM I-V [2].

CHAPTER VII

CONCLUSIONS

7.1 Summary

A multiple-band envelope function method was applied to the CdS/HgS/CdS quantum-well-quantum-dot semiconductor nanocrystals. Bulk HgS is a narrow band gap semiconductor. The wave functions of discrete energy levels close to the band edges of HgS should be a strong mixture of both the valence band and the conduction band states. At the same time, the band edges of HgS are near the center of the forbidden gap of the bulk CdS. For those sates with eigenenergies close to the band edges of HgS, their wave functions inside the CdS layers should also be a strong mixing of the valence bands and the conduction bands of CdS. We used the eight-band method (including spin degeneracy) to calculate the eigenenergies and the corresponding wave functions of the discrete electron states in the CdS/HgS/CdS system. The effects of other bands are taken into account in the second order perturbation theory. For a fixed energy E, eight independent solutions and four k values were found inside each layer. Inside each layer, the general solution for the envelope function is a combination of the eight independent solutions. Eight coefficients, the weights of each independent solution in the general solution, are unknown variables. The boundary conditions at the interfaces connect the coefficients in neighboring layers. The requirements for the wave functions, being finite both at the core and at infinite distance, determine the eigenvalues of the energy and the coefficients in the layers.

We use spherical Bessel functions and modified spherical Bessel functions as the trial functions for the independent solutions in each layer. For the energies above the conduction band minimum, two independent solutions consist of the spherical Bessel functions $j_l(r)$ and $y_l(r)$ while the other six consist of the modified spherical Bessel functions $i_l(r)$ and $k_l(r)$. When the energy is inside the forbidden energy gap of the bulk material, all eight solutions consist of the modified spherical Bessel functions. When the energy is below

the maximum of the valence bands, six solutions consist of the spherical Bessel functions and two consist of the modified spherical Bessel functions. We found that it was difficult to find exact solutions of the energy eigenvalues. This difficulty is due to the modified spherical Bessel functions, which either increase or decrease exponentially. These functions introduce very large and very small terms to the numerical calculation at the same time which makes makes the numerical matrix inversion difficult. Actually it proved impossible to find the wave functions for those sates with energy above the conduction band minimum of the HgS, since the wave functions of these states are composed of six modified spherical Bessel functions and two spherical Bessel functions inside the HgS layer. For states with energies below the valence band maximum of bulk HgS, it is easier to find the wave functions since these wave functions are composed of two modified spherical Bessel functions and two spherical Bessel functions inside the HgS layer.

We acquired spectra from chemically synthesized gold nanocrystals with diameters of 1.5 nm and 1.8 nm. If we assume these nanocrystals are spherical and apply the free-electron model to them, we find that the voltage gaps between the neighboring dI/dV peaks in STS measurements could be as large as 0.2 V. This corresponds to an energy spacing about 0.1 eV$\sim$0.2 eV (the exact value depends on the voltage division between the two junctions). Some of our experiment data show that the voltage gap related to the single electron charging energy of these nanocrystals is in the range around 0.5 V. So the charging energy and the energy spacing between discrete electron levels are of the same order. Unlike bulk semiconductors, gold doesn't have a big forbidden energy gap. The comparability of the electron level spacing and the charging energy makes the interpretation of the STS spectra of gold nanocrystals challenging. Our calculation shows that both levels above and below the Fermi level will be involved in the tunneling current. Electron-hole pairs are expected to exist inside gold nanocrystals during tunneling. The model that we developed to understand and interpret the STS spectra which considers the effects of discrete electron levels and excited states with up to two electron-hole pairs. Electron relaxation between discrete levels has also been taken into account.

We found that it is not straightforward to find all the states involved in the tunneling

at a particular tip bias. The difficulties are due to the existence of path-dependent states. When an electron tunnels from the tip to the nanocrystal, some of its kinetic energy can be transferred to the electrostatic energy inside two junctions. Therefore multiple charging is possible at low tip bias. We call this self-pumping. In order to overcome this state counting problem, we used the "generation" concept to find out which states are involved in the tunneling at a particular bias. The purpose of this was to find the path-dependent states.

The first effect of electron-hole pairs excited states on the tunneling spectra is that some of the dI/dV peaks are suppressed. This makes the apparent spacing of dI/dV peaks irregular. This simulation result may be used to interpret some of our experimental spectra. The second effect of the excited states is that negative differential conductance can appear. There are some experimental data show the existence of negative differential conductance.

We also simulated BEES current versus voltage spectra. The transport coefficient across the gold-silicon interface was extracted from the measured BEES I-V curve with the tip is held at a constant position. The most striking effect of the gold nanocrystals on the BEES current is that the threshold voltage for the BEES current can shift. Further more, our calculations predict that, because of the self-pumping mechanism, the BEES current could be nonzero *below* the threshold voltage for normal BEES experiments.

An ultra-high vacuum and low-temperature STM system was re-designed and rebuilt. BEEM/BEES capability was implemented. We imaged gold nanocrystals with different sizes and different capping molecules. Spectroscopic measurements were also done on many of these gold nanocrystals. We also imaged some semiconductor nanocrystals of CdS and CdSe. Good Schottky barriers between thin gold films and the Si(111) surfaces were made successfully. BEES current versus voltage spectra on gold nanocrystals were measured and compared with calculations.

7.2 Future Work

In the simulation of tunneling current, the effects of the capping layer and the SAM layer were not considered carefully. They are treated as "vacuum". Some of the gold nanocrystals are capped with benzenethiol. The tunneling resistance of the benzenethiol molecules is in

the MΩ range [59]. This resistance is lower than typical tunneling resistances. Therefore, junctions with benzenethiol may require some modification of the model. One possible approach would be to use a modified value of the work function. At the same time, more spectra of Au nanocrystals capped with benzenethiol but with different sizes should be collected. The tunneling spectra of Au nanocrystals capped with benzenethiol are worthy to be compared with spectra of those capped with dodecanethiol in order to find out the effect of the capping agents.

For the BEES measurements, it is worthy to investigate the size dependence of the BEES current on gold nanocrystals. The electron dynamics inside gold nanocrystals may be very different for nanocrystals with different sizes. Simultaneous measurement of dI/dV curves and BEES I-V curves would provide rich information.

Bibliography

[1] Alex Schill in Professor Mostafa El-Sayed's group at the Georgia Tech School of Chemistry provides CdS nanocrystals. These nanocrystals aree capped with dodecanthiol.

[2] All the gold nanocrystals we used in the experiemnts were synthesized by Ryan Price in Professor Whetten's group at Georgia Institute of Technology School of Chemistry.

[3] Qusai Darugar in Professor Mostafa El-Sayed's group at the Georgia Tech School of Chemistry provides CdSe nanocrystals. There are two types of CdSe samples. One is capped with trioctylphosphine oxide (TOPO). The other is capped with mercaptan.

[4] Terry Bigioni measured dI/dV versus V curves on Au 29 kDa nanocrystals at 77 K using the STM in Dr. First's group. Some of the data used in theis belong to him.

[5] The amplifiers were purchased from Stanford Research Systems, Inc. 1290-D Reamwood Ave., Sunnyvale, CA 94089. http://www.thinksrs.com.

[6] The current preamplifier we used for the tunneling current is Ithaco 1211 Current Preamplifier from DL Instruments, 233 Cecil A. Malone Drive Ithaca, New York 14850. http://www.dlinstruments.com.

[7] The epoxy we used were purchased from Epoxy Technology, Inc. (www.epotek.com). The conducting epoxy is E4110. The insulating epoxy is H77.

[8] The etching machine was built by Professor Marchenkov. We thank him for allowing us to use this machine.

[9] The Pt/Ir wire was purchased from the Wilkinson Company, Westlake Village, CA.

[10] The silicon wafer used for BEEM samples were purchased from Silicon, Inc. (http://www.siwafers.com). These 4 in wafer are n type. The sheet resisance is 1-5 ohms-cm. The thickness is 450+/-25 micro. Only one side is polished.

[11] The standard procedures to clean silicon wafers (RCA1 and RCA2) can be found athttp://www.ampel.ubc.ca/nanofab/sop/rca-clean-1.pdf and http://www.ampel.ubc.ca/nanofab/sop/rca-clean-2.pdf.

[12] Agam, O., Wingreen, N. S., Altshuler, B. L., Ralph, D. C., and Tinkham, M., "Chaos, interactions, and nonequilibrium effects in the tunneling resonance spectra of ultrasmall metallic particles," *PHYSICAL REVIEW LETTERS*, vol. 78, no. 10, pp. 1956–1959, 1997.

[13] Arbouet, A., Voisin, C., Christofilos, D., Langot, P., Del Fatti, N., Vallee, F., Lerme, J., Celep, G., Cottancin, E., Gaudry, M., Pellarin, M., Broyer, M., Maillard, M., Pileni, M. P., and Treguer, M., "Electron-phonon scattering in metal clusters," *PHYSICAL REVIEW LETTERS*, vol. 90, no. 17, p. 177401, 2003.

[14] Averin, D. V. and Likharev, K. K., *Mesoscopic Phenomena in Solids*, p. 169. Elsevier, Amsterdam, 1991.

[15] Bastard, G., *Wave Mechanics Applied to Semiconductor Heterostructures*. Halsted Press, 1990.

[16] BEENAKKER, C. W. J., "Theory of coulomb-blockade oscillations in the conductance of a quantum dot," *PHYSICAL REVIEW B*, vol. 44, pp. 1646–1656, July 1991.

[17] BELL, L. D. and KAISER, W. J., "Observation of interface band-structure by ballistic-electron-emission microscopy," *PHYSICAL REVIEW LETTERS*, vol. 61, pp. 2368–2371, Nov. 1988.

[18] Bigioni, T. P., Harrell, L. E., Cullen, W. G., Guthrie, D. E., Whetten, R. L., and First, P. N., "Imaging and tunneling spectroscopy of gold nanocrystals and nanocrystal arrays," *EUROPEAN PHYSICAL JOURNAL D*, vol. 6, pp. 355–364, June 1999.

[19] Bigioni, T. P., Schaaff, T. G., Wyrwas, R. B., Harrell, L. E., Whetten, R. L., and First, P. N., "Scanning tunneling microscopy determination of single nanocrystal core sizes via correlation with mass spectrometry," *JOURNAL OF PHYSICAL CHEMISTRY B*, vol. 108, pp. 3772–3776, Mar. 2004.

[20] Bigioni, T. P., *Scanning Tunneling Microscopy and Spectrosopy of Passivated Gold Nanocrystals*. PhD thesis, Georgia Institute of Techologu, 1999.

[21] Bir, G. L. and Pikus, G. E., *Symmetry and Strain-Induced Effects in Semiconductors*. Wiley, 1975.

[22] BRUST, M., WALKER, M., BETHELL, D., SCHIFFRIN, D. J., and WHYMAN, R., "Synthesis of thiol-derivatized gold nanoparticles in a 2-phase liquid-liquid system," *JOURNAL OF THE CHEMICAL SOCIETY-CHEMICAL COMMUNICATIONS*, pp. 801–802, Apr. 1994.

[23] Bryant, G. W. and Jaskolski, W., "Tight-binding theory of quantum-dot quantum wells: Single-particle effects and near-band-edge structure," *PHYSICAL REVIEW B*, vol. 67, p. 205320, May 2003.

[24] BURT, M. G., "An exact formulation of the envelope function-method for the determination of electronic states in semiconductor microstructures," *SEMICONDUCTOR SCIENCE AND TECHNOLOGY*, vol. 2, no. 7, pp. 460–462, 1987.

[25] BURT, M. G., "An exact formulation of the envelope function-method for the determination of electronic states in semiconductor microstructures," *SEMICONDUCTOR SCIENCE AND TECHNOLOGY*, vol. 3, no. 8, pp. 739–753, 1988.

[26] BURT, M. G., "The justification for applying the effective-mass approximation to microstructures," *JOURNAL OF PHYSICS-CONDENSED MATTER*, vol. 4, no. 32, pp. 6651–6690, 1992.

[27] Callaway, J., *Quantum theory of the solid state*. Academic Press, 1990.

[28] Davidovic, D. and Tinkham, M., "Coulomb blockade and discrete energy levels in au nanoparticles," *APPLIED PHYSICS LETTERS*, vol. 73, no. 26, pp. 3959–3961, 1998.

[29] Efros, A. L. and Rosen, M., "Quantum size level structure of narrow-gap semiconductor nanocrystals: Effect of band coupling," *PHYSICAL REVIEW B*, vol. 58, pp. 7120–7135, Sept. 1998.

[30] Ferry, D. and Goodnick, S. M., *Transport in Nanostructures*. Cambridge University Press, 1997.

[31] FOREMAN, B. A., "Effective-mass hamiltonian and boundary-conditions for the valence bands of semiconductor microstructures," *PHYSICAL REVIEW B*, vol. 48, p. 4964, 1993.

[32] Grabert, H. and Devoret, M. H., eds., *Single Charge Tunneling, NATO Advanced Study Institute, Series B: Physics*. Plenum, New York, 1991.

[33] Grant, C. D., Schwartzberg, A. M., Yang, Y. Y., Chen, S. W., and Zhang, J. Z., "Ultrafast study of electronic relaxation dynamics in au-11 nanoclusters," *CHEMICAL PHYSICS LETTERS*, vol. 383, no. 1-2, pp. 31–34, 2004.

[34] Hanna, A. E. and Tinkham, M., "Variation of the coulomb staircase in a 2-junction system by fractional electron charge," *PHYSICAL REVIEW B*, vol. 44, no. 11, pp. 5919–5922, 1991. no discrete energy levels resolved. cosidering the charge at different bias voltage.

[35] Harrell, L. E. and First, P. N., "An ultrahigh vacuum cryogenic scanning tunneling microscope with tip and sample exchange," *Review of Scientific Instruments*, vol. 70, p. 125, 1999.

[36] Harrell, L. E., *Investigation of Gold Nanocrystals by Ultrahigh Vacuum Cryogenic Scanning Tunneling Microscopy*. PhD thesis, Georgia Institute of Technology, 1998.

[37] Hartland, G. V., "Measurements of the material properties of metal nanoparticles by time-resolved spectroscopy," *PHYSICAL CHEMISTRY CHEMICAL PHYSICS*, vol. 6, no. 23, pp. 5263–5274, 2004.

[38] HOHENBERG, P. and KOHN, W., "Inhomogeneous electron gas," *PHYSICAL REVIEW B*, vol. 136, no. 3B, pp. B864–&, 1964.

[39] Jaskolski, W. and Bryant, G. W., "Multiband theory of quantum-dot quantum wells: Dim excitons, bright excitons, and charge separation in heteronanostructures," *PHYSICAL REVIEW B*, vol. 57, p. R4237, 1998.

[40] KAISER, W. J. and BELL, L. D., "Direct investigation of subsurface interface electronic-structure by ballistic-electron-emission microscopy," *PHYSICAL REVIEW LETTERS*, vol. 60, no. 14, pp. 1406–1409, 1988.

[41] KOHN, W. and SHAM, L. J., "Self-consistent equations including exchange and correlation effects," *PHYSICAL REVIEW*, vol. 140, no. 4A, pp. 1133–&, 1965.

[42] Link, S., Beeby, A., FitzGerald, S., El-Sayed, M. A., Schaaff, T. G., and Whetten, R. L., "Visible to infrared luminescence from a 28-atom gold cluster," *JOURNAL OF PHYSICAL CHEMISTRY B*, vol. 106, no. 13, pp. 3410–3415, 2002.

[43] LUTTINGER, J. M. and KOHN, W., "Motion of electrons and holes in perturbed periodic fields," *PHYSICAL REVIEW*, vol. 97, no. 4, pp. 869–883, 1955.

[44] Millo, O., Katz, D., Cao, Y. W., and Banin, U., "Scanning tunneling spectroscopy of inas nanocrystal quantum dots," *PHYSICAL REVIEW B*, vol. 61, no. 24, pp. 16773–16777, 2000.

[45] Murray, C. B., Kagan, C. R., and Bawendi, M. G., "Synthesis and characterization of monodisperse nanocrystals and close-packed nanocrystal assemblies," *ANNUAL REVIEW OF MATERIALS SCIENCE*, vol. 30, pp. 545–610, 2000.

[46] MURRAY, C. B., NORRIS, D. J., and BAWENDI, M. G., "Synthesis and characterization of nearly monodisperse cde (e = s, se, te) semiconductor nanocrystallites," *JOURNAL OF THE AMERICAN CHEMICAL SOCIETY*, vol. 115, pp. 8706–8715, Sept. 1993.

[47] Narvaez, G. A. and Kirczenow, G., "Electronic excitations and tunneling spectra of metallic nanograins," *PHYSICAL REVIEW B*, vol. 68, no. 24, p. 245415, 2003.

[48] PIDGEON, C. R. and BROWN, R. N., "Interband magneto-absorption and faraday rotation in insb," *PHYSICAL REVIEW*, vol. 146, no. 2, pp. 575–&, 1966.

[49] Pokatilov, E. P., Fonoberov, V. A., Fomin, V. M., and Devreese, J. T., "Electron and hole states in quantum dot quantum wells within a spherical eight-band model," *PHYSICAL REVIEW B*, vol. 64, p. 245329, Dec. 2001.

[50] Price, R. C. and Whetten, R. L., "All-aromatic, nanometer-scale, gold-cluster thiolate complexes," *JOURNAL OF THE AMERICAN CHEMICAL SOCIETY*, vol. 127, pp. 13750–13751, Oct. 2005.

[51] Ralph, D., Black, C., and Tinkham, M., "Spectroscopy measurement of discrete electronic states in single metal particles," *PHYSICAL REVIEW LETTERS*, vol. 74, no. 16, pp. 3241–3244, 1995. this letter comtains almost everything I am thinking.

[52] Reddy, C. V., Narayanamurti, V., Ryou, J. H., Chowdhury, U., and Dupuis, R. D., "Imaging and local current transport measurements of alinp quantum dots grown on gap," *APPLIED PHYSICS LETTERS*, vol. 76, no. 11, pp. 1437–1439, 2000.

[53] Reddy, C. V., Narayanamurti, V., Ryou, J. H., Chowdhury, U., and Dupuis, R. D., "Observation of resonant tunneling through a quantized state in inp quantum dots in a double-barrier heterostructure," *APPLIED PHYSICS LETTERS*, vol. 77, no. 8, pp. 1167–1169, 2000.

[54] Simmons, J. G., "Generalized thermal j-v characteristic for electric tunnel effect," *JOURNAL OF APPLIED PHYSICS*, vol. 35, no. 9, p. 2655, 1964.

[55] Smith, D. L., Lee, E. Y., and Narayanamurti, V., "Ballistic electron emission microscopy for nonepitaxial metal/semiconductor interfaces," *PHYSICAL REVIEW LETTERS*, vol. 80, no. 11, pp. 2433–2436, 1998.

[56] STEIGERWALD, M. L., ALIVISATOS, A. P., GIBSON, J. M., HARRIS, T. D., KORTAN, R., MULLER, A. J., THAYER, A. M., DUNCAN, T. M., DOUGLASS, D. C., and BRUS, L. E., "Surface derivatization and isolation of semiconductor cluster molecules," *JOURNAL OF THE AMERICAN CHEMICAL SOCIETY*, vol. 110, pp. 3046–3050, May 1988.

[57] Voisin, C., Christofilos, D., Loukakos, P. A., Del Fatti, N., Vallee, F., Lerme, J., Gaudry, M., Cottancin, E., Pellarin, M., and Broyer, M., "Ultrafast electron-electron scattering and energy exchanges in noble-metal nanoparticles," *PHYSICAL REVIEW B*, vol. 69, no. 19, p. 195416, 2004.

[58] WATANABE, S., NAKAYAMA, N., and ITO, T., "Homogeneous hydrogen-terminated si(111) surface formed using aqueous hf solution and water," *APPLIED PHYSICS LETTERS*, vol. 59, pp. 1458–1460, Sept. 1991.

[59] Whetten, R. L. Talk at group meeting, School of Physics, Georgia Tech, 2005.

[60] Wilkins, R., BENJACOB, E., and JAKLEVIC, R. C., "Scanning-tunneling-microscopy observations of coulomb blockade and oxide polarization in small metal droplets," *PHYSICAL REVIEW LETTERS*, vol. 63, pp. 801–804, Aug. 1989.